Evaluation of Wind Flows and Turbulent Fluxes in Complex Terrain of Canadian Rockies

by

Mina Rohanizadegan

A thesis
presented to the University of Waterloo
in fulfillment of the
thesis requirement for the degree of
Doctor of Philosophy
in
Geography

Waterloo, Ontario, Canada, 2024

Examining Committee Membership

The following served on the Examining Committee for this thesis. The decision of the Examining Committee is by majority vote.

External Examiner:	Dr. Stephan De Wekker Professor, University of Virginia
Supervisor:	Dr. Richard Petrone Professor, University of Waterloo
Co-Supervisor:	Dr. John Pomeroy Distinguished Professor, University of Saskatchewan
Internal Member:	Dr. Claude Dughuay Professor, University of Waterloo
Internal-External Member:	Dr. John Lin Professor, University of Utah
Other Member:	Dr. Warren Helgason Associate Professor, University of Saskatchewan

Author's Declaration

This thesis consists of material all of which I authored or co-authored: see Statement of Contributions included in the thesis. This is a true copy of the thesis, including any required final revisions, as accepted by my examiners.

I understand that my thesis may be made electronically available to the public.

Statement of Contributions

This thesis has been structured in accordance with the manuscript option. Chapter two has been published. Chapter three is under review, and chapter four is in preparation and will be submitted for review; consequently, should the Chapter 3 and 4 manuscripts be accepted for publication, they may differ from what is presented in this thesis due to comments and feedback following peer-review. Chapter two is published as:

Mina Rohanizadegan, Richard M. Petrone, John W. Pomeroy, Branko Kosovic,Domingo Muñoz-Esparza, and Warren D. Helgason (2023). High-Resolution Large-Eddy Simulations of Flow in the Complex Terrain of the Canadian Rockies. Earth and Space Science. http://doi.org/10.1029/2023EA003166

Mina Rohanizadegan completed the study design, data analysis, generated the original ideas of using large-eddy simulations to study the flows in complex terrain, and wrote the first draft of the manuscript. Dr. Richard M. Petrone and Dr. John W. Pomeroy provided resources and feedback on the writing of the manuscript and interpretation of the analysis. Dr. Branko Kosovic contributed to the methodology of the simulations, provided resources, and feedback on the writing, and Dr. Domingo Muñoz-Esparza contributed to the methodology of the simulations. Dr. Warren D. Helgason provided the resources.

Chapter three is submitted as:

Mina Rohanizadegan, Richard M. Petrone, John W. Pomeroy, and Branko Kosovic (2023). Analysis of Turbulence and Turbulent Kinetic Energy Dynamics in Complex Terrain. JGR: Atmospheres.

Mina Rohanizadegan completed the study design, data analysis, generated the original ideas of using simulations and observations to study the turbulence in complex terrain, and wrote the first draft of the manuscript. Dr. Richard M. Petrone provided resources and feedback on the writing of the manuscript, and Dr. John W. Pomeroy provided resources, and provided feedback on conceptualization of the turbulent transport in mountainous terrain, and provided feedback on the writing of the manuscript. Dr. Branko Kosovic contributed to the analysis, provided resources, and feedback on the writing.

Chapter four is prepared as:

Mina Rohanizadegan, Richard M. Petrone, and John W. Pomeroy. Influence of elevation dependent heterogeneity on heat and evaporative fluxes in complex terrain.

Mina Rohanizadegan completed the study design, data analysis, and the writing of the first draft. Dr. Richard M. Petrone provided feedback on the writing of the manuscript. Dr. John Pomeroy provided valuable feedback on the analysis and feedback on the writing of the manuscript.

By signing below, I indicate that I agree with the evaluation of the roles and contributions of the various authors expressed above

Abstract

In mountains, the role of diurnal wind (i.e. valley, slope winds) due to differential heating, radiation and topography in controlling fluxes of heat and water vapour is not well understood. Since data in high mountain areas are limited, high resolution models can help resolve near-surface processes and their diurnal changes to use as an input to hydrological models for more accurate predictions of evapotranspirartion and future water resources. Improvements over recent years in the resolution of Numerical weather prediction (NWP) models and large-eddy-simulation (LES) have had made great progress on resolving the atmospheric boundary layer (ABL) and boundary layer processes over mountainous terrain. In this work, the Weather Research and Forecasting (WRF) model is used to simulate flow in LES mode over the complex terrain of the Fortress Mountain and Marmot Creek research basins (MCRB and FMRB, respectively), Kananaskis Valley,Canadian Rockies, Alberta in mid- and late summer. The days selected in this study allow for development of thermally-induced wind circulation and ABL processes. However, the use of terrain-following coordinates in most numerical weather prediction models results in errors that propagate through the domain and can result in numerical instability. To avoid this issue when simulating flow over steep terrain a local smoothing approach was used, where smoothing is applied only where slope exceeds some predetermined threshold. The results are compared with global smoothing, which uniformly filters terrain, and is already implemented in WRF. Local smoothing with the cumulus parametrization activated only for the parent domain provides better predictions for surface wind direction, improved predictions for net radiation, and better RMSE for humidity, and was used for the rest of the analysis on turbulence kinetic energy (TKE) and near- surface processes. The model shows that valley flows are impacted by wind gusts and topographic wind originated from higher elevations blowing into the valley. In this study, up-valley flows were stronger in the wide but deeper Kananaskis Valley in MCRB, as compared to the narrower and shallower valley in FMRB. In addition, cold-air pools seem to linger longer in the deeper and wider valley at MCRB, but air temperature was lower in the early morning at the shallower but narrower valley at FMRB. The removal of the cold air pool due to temperature rise happened earlier in the valley in FMRB than in the valley of MCRB due to an elevated inversion layer of the deeper valley.

Boundary layer processes and turbulence in complex terrain are influenced by thermally-induced flows, as well as dynamical or non-local winds. Data from three high-frequency eddy covariance systems at a northwest-facing slope location, and at two ridgetops at the south and north valley side walls of the Fortress Valley were combined with LES to investigate the influence of diurnal mountain flows on TKE. Simulated cross sections showed up-valley flow was inclined toward the northern valley wall at the southeast side of the valley, and the interactions between the up-valley flow and the cross-ridge flows contribute to TKE in the valley. It was found that there is a strong correlation between TKE and wind speed at ridgetops, while TKE in the valley correlated strongly with the wind speed at the northern ridgetop. Furthermore, TKE budget analysis showed that horizontal shear could be an important source of TKE production at the northwest-facing slope station in the Fortress Valley. The variability observed in TKE budget components across different locations within this high mountain basin indicates the significance of both horizontal and vertical exchange processes in the mechanisms governing TKE production.

The final portion of this study evaluated model predictions of sensible and latent heat fluxes versus observations at three eddy-covariance locations in the Fortress Valley. The differences between model predictions and observations illustrates the crucial role of soil moisture, along with net radiation, in controlling the heat and evaporative fluxes in mountainous terrain. The observations over July and August were further used to quantify the variability of the sensible and latent fluxes with soil moisture content and net radiation, as influenced by elevation and vegetation. Observations showed that despite variations in vegetation type and elevation, the latent heat flux exhibited a weak correlation with soil moisture at each site but displayed a strong correlation with net radiation at all sites for both wet and dry days. But when all study sites were compared together for mid- versus late summer sunny days, it was noted that the local topography and soil moisture, radiation, and local flows can all have important impacts on turbulent fluxes. The findings also indicate that longer term data with a wider range of soil moisture, and topographical features (i.e slopes, aspect) will be beneficial for more in depth future studies on exchange processes in mountainous terrains.

Acknowledgments

I would like to express my gratitude to my adviser Dr. Richard Petrone, for his tremendous support and patience throughout my PhD journey. Dr. Petrone not only provided me with the freedom to explore my research and finding my own collaborators, but has also supported me to take the time to navigate my personal life. I would like to also thank my co-adviser Dr. John Pomeroy, who provided invaluable guided direction on my research, was instrumental in my field work and the data required for my thesis, and has supported me throughout my PhD.

I also would like to express my appreciation to members of my PhD committee, Dr. Claude Duguay, Dr. John Lin, and Dr. Warren Helgason for their continued support. I also would like to sincerely thank my collaborators, specially Dr. Branko Kosovic for providing me with the unique opportunity to use the computational facility at NCAR (National Center for Atmospheric Research), and providing invaluable guidance on my research. I would like to thank Dr. Domingo Muñoz-Esparza for providing support with computational aspect of my research. I would like to thank all the students and the technicians who helped me to acquire data for my thesis, and helped me with the field trips.

This thesis could not have been accomplished without the love and support of my parents, sisters, and brother. Their unconditional support has been my motivation to this end.

Finally, a heartfelt thank you to my beloved husband, Chris, who has always been by my side throughout this journey. Without his dedication to provide me with emotional support when I needed, and providing comfort in our personal life, this thesis would not have been possible to accomplish.

Dedication

This dissertation is dedicated to my beloved mother Mehri, my husband Chris, and my daughter Parisa.

Table of Contents

List of Figures

List of Tables

Chapter 1

Introduction

1.1 Diurnal Mountain Wind Systems

The atmospheric boundary layer (ABL) is the lower part of the atmosphere where the exchange of momentum, heat, and water vapor occurs between the surface and the free atmosphere above. Its depth can range from surface level to a few kilometers, depending on atmospheric stability and convective conditions (Stull, 1988). Traditionally, the ABL is recognized for turbulent motions (surface forcing; friction and convection) driving mass, heat, and momentum exchanges between the surface and the atmosphere (Rotach *et al.*, 2015). While buoyancy-driven production is the primary mechanism in transferring the fluxes to the atmosphere on a sunny day over a flat terrain, additional processes influence exchange on spatial or temporal scales in mountainous areas (Lehner & Rotach *et al.*, 2018). Wind effects, for instance, significantly impact turbulent production and the horizontal and vertical exchange of mass, moisture, and momentum in complex terrains.

Figure 1.1 presents a conceptual illustration of a daytime convective boundary layer in complex terrain, and the associated processes. In mountainous regions, thermally forced flows such as slope and valley winds, or diurnal mountain winds, are common. These arise from horizontal contrasts in heating and cooling due to horizontal differences in temperature between the land and atmosphere throughout the day (Whiteman, 2000; Schmidli &

Rotunno, 2010). Mountain-plain circulations occur due to daytime heating and nighttime cooling, creating horizontal pressure contrasts between the atmosphere over the mountain and the surrounding plain. These circulations play a major role in horizontal exchange through transporting air pollutants and moisture between the mountain and plain (Wagner *et al.*, 2015; Diemoz *et al.*, 2018).

Slope flows and cross-valley circulations facilitate mass and heat transport within the boundary layer adjacent to slopes. The efficiency of this process depends on the slope geometry, aspect, and atmospheric forcing conditions (Rotach *et al.*, 2015). Both slope flows and mountain venting serve as important mechanisms for the vertical transport of moisture from the ABL to the free atmosphere, involving the lifting of moist air to the mountaintops, initiating condensation (Dewekker *et al.*, 2004; Gohm *et al.*, 2009; Kirshbaum *et al.*, 2018). Mountain venting occurs when near-surface air is transported by thermally driven winds towards the mountain ridges, and then upwards over slopes. Daytime upslope flows are the results of the ongoing heated air in the boundary layer above a slope, whereas nighttime slope flows form as the cooled air in the boundary layer descends the slope after losing heat to the surface (Figure 1.2 a, b) (Zardi & Whiteman, 2013).

Valley wind systems are part of diurnal circulation driven by warmer or colder air in the valley, replaced by adjacent plain air, or air further down the valley at the same altitude, facilitated by the rising or sinking slope flows (Figure 1.2 c, d) (Rampanelli & Zardi, 2004; Schmidli & Rotunno, 2010). The up-valley wind advects cold air into the valley, and its strength is influenced by valley geometry such as volume and orientation (Zangl, 2004; Schmidli, 2013; Wagner *et al.*, 2015), along-valley pressure gradients and heat transfer processes over slopes (Giovannini *et al.*, 2017). Although valley flows are robust to external forcing once established, their strength and direction can be influenced by mesoscale and synoptic scale flows or through their interactions with the surrounding topography (Zangl, 2009). Background flow and terrain interactions produce smaller-scale flow separations and eddies, impacting valley flows, and even strong ridge-level winds, which might reach valley bottoms (Zardi & Whiteman, 2013). Self-shading can delay the formation of thermally driven flows in a complex terrain due to modifications to energy balance at the surface and sensible heat fluxes.

Dynamically driven flows are another important phenomena in complex terrain, par-

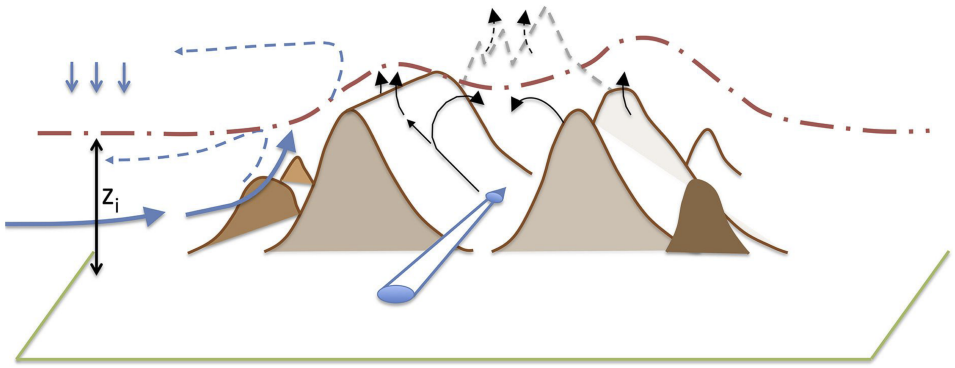

Figure 1.1: Daytime thermally driven flows in mountainous terrain, where the convective boundary layer is shown by the red-dashed dotted line, plain-to-mountain circulation and valley wind circulation (blue arrows), slope flow and mountain venting (black arrow). Taken from (Rotach *et al.*, 2015) (Figure 1).

ticularly observed in the Rocky Mountains (Whiteman, 2000). These regions frequently experience synoptic-scale and dynamically driven wind flows, resulting from the orographic lift of incoming mesoscale winds and prevailing strong winds. When the kinetic energy of the wind surpasses the potential energy of the obstacle, depending on the mountain height, wind velocity and atmospheric stability, the lifted air by the mountain is able to pass over the peak. Eventually, this air cascades down, leading to downslope wind storms or turbulent eddies on the lee side (Jackson *et al.*, 2013). Moderate downslope winds occur when the upstream air mass becomes cooler than that in the valley as the daytime solar heating warms up the air within the valley, and the flowing air above induces downslope winds when interacting with topography (Jiang & Doyle, 2008; Sheridan & Vosper, 2012). During stratified and stable atmospheric conditions (i.e. winter months or night time), the cold air lifted to the mountain tops falls due to gravity generating gravity waves. However, during daytime, this process can lead to disturbances in the formation of up-valley flows through wave breaking (Strauss *et al.*, 2016).

Terrain inhomogeneities, including variations in topography and vegetation, induce thermo-topographic flows caused by differential heating (Rotach & Zardi, 2007). Lee-side eddies and vortices alongside mountain ridges often result in frequent wind gusts that im-

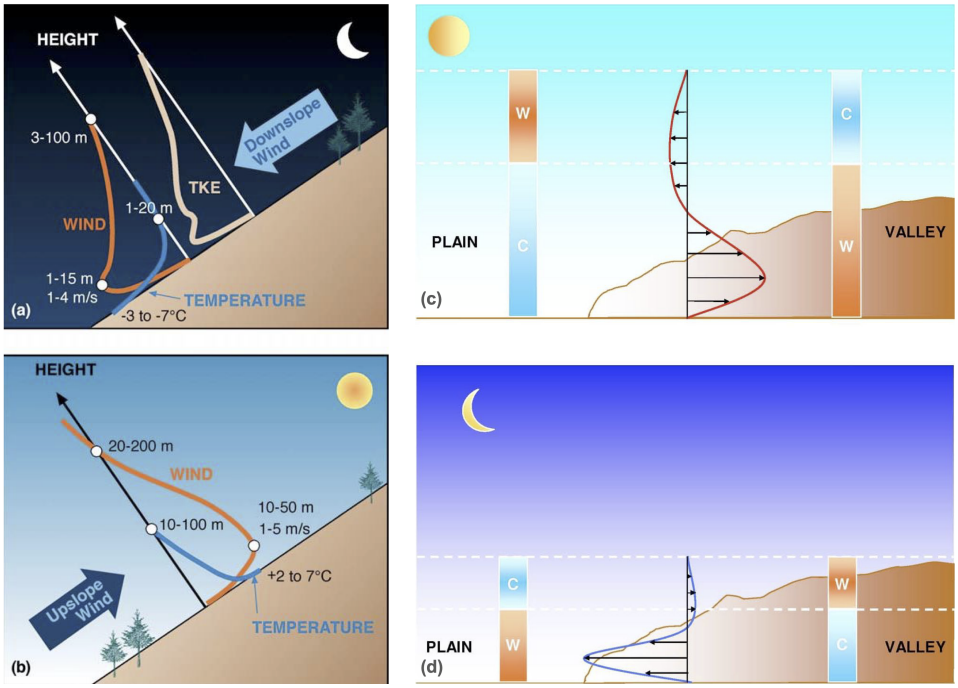

Figure 1.2: Temperature, wind and TKE profiles of (a) down slope and (b) up slope flows, showing the temperature deficit or excess, jet-like feature of slope flows. Wind profiles of (c) up-valley and (d) down-valley flows, showing the direction of up-valley from plain to mountain during daytime, and down-valley flow from mountain to plain during nighttime. Adapted from (Whiteman, 2000).

pact valley flows (Grubisic *et al.*, 2008). The distribution of valley flows is also affected by horizontal pressure gradients along the valley axis (Zardi & Whiteman, 2013), as well as by the centrifugal force imposed on the valley flow in curved valleys (Weigel & Rotach, 2004). Such phenomena illustrate the dynamic interplay between atmospheric stability, topography, and prevailing wind patterns, contributing to the complexity of airflow behaviors in mountainous regions.

The sheltering effect created by surrounding topography around a valley tends to reduce sensible heat flux, leading to the earlier formation or persistence of cold pools (Vosper *et al.*, 2014; Lehner & Rotach, 2018). While cold pools disperse during the morning in summer, wider or deeper valleys experience longer-lasting inversions, resulting in more persistent cold-air pools within these locations (Serafin & Zardi, 2010; Colette *et al.*, 2003).

1.2 Numerical Modeling of Boundary Layer Processes in Complex Terrain

Numerical weather prediction (NWP) models in complex terrain have undergone significant improvements in recent years due to the rise of computational power and adoption of new numerical techniques (Colman *et al.*, 2013). These improvements are particularly evident in the reduction of horizontal grid spacing to sub-kilometer scales for modeling ABL processes (Chow *et al.*, 2006; Weigel *et al.*, 2006; Goger *et al.*, 2018; Udina *et al.*, 2017). However, modeling in mountainous regions, characterized by complex topography, remains a challenging task.

Vertical mixing (eddy transport of vertical fluxes) in mesoscale models makes use of one dimensional planetary boundary layer schemes (PBL) developed primarily for flat terrain, assuming spatial homogeneity and therefore considering only vertical turbulent exchange. In complex terrains, this one-dimensional parametrization of turbulent processes results in misrepresentations of various ABL processes such as Turbulent kinetic energy (TKE) (Couvreux *et al.*, 2016), or mountain waves (Munoz-Esparza *et al.*, 2015). In fact, many ABL processes in heterogeneous terrain have horizontal components and exhibit a three-

dimensional nature driven by complex orography (e.g. valley and slope flows, the formation of cold pools).

For mountains, improving the calculation and parametrization of land-atmosphere fluxes of heat and water vapor requires better resolution of thermally driven diurnal winds. To achieve this, the utilization of fully three-dimensional turbulence schemes becomes necessary to accurately capture small-scale turbulent features observed in complex topography, especially concerning the generation of total kinetic energy (TKE) in valleys and slopes (Goger *et al.*, 2018). High-resolution large-eddy simulations (LES) aim to explicitly resolve the largest and most energetic eddies of the Inertial Subrange (Cuxart, 2015), assuming a cascade of energy to smaller sub-grid eddies, which are parametrized. Thus, by assuming that only these 'large eddies' are directly affected by the mean flow and assuming that the parametrized small-scales show a somewhat universal behavior, LES helps to mitigate uncertainties regarding turbulence structure over complex terrains. Hence, LES serves as the basis for the simulations conducted in this dissertation.

Advancements in computational resources have made LES more accessible in real-case applications (Rai *et al.*, 2017; Gerber *et al.*, 2018; Liu *et al.*, 2020; Umek *et al.*, 2021; Umek *et al.*, 2022; Goger *et al.*, 2022). LES, operating below a scale of 100 m, offers improvements over subgrid parametrizations for eddies of all scales in Reynolds-Averaged Navier-Stokes simulations (Chow *et al.*, 2013). The success of LES in capturing boundary layer processes and thermally induced circulations depends on resolving topographic features like valleys and slopes, as well as improving soil moisture representation and employing high-resolution land-use data (Chow *et al.*, 2006; Rihani *et al.*, 2015; Schmidli *et al.*, 2018). Idealized simulations with various horizontal grid spacings by (Wagner *et al.*, 2014) showed that the topography representation in the model is a crucial factor for correctly simulating the ABL.

Despite improvements in terrain representation, numerically resolving the effect of complex terrain on wind flow demands smaller grid cell size. The most common way to resolve vertical structure of ABL in numerical weather prediction models is the use of terrain-following coordinates. That results in large numerical errors when flow over steep terrain is simulated. These errors propagate through the domain and can result in numerical instability. Terrain smoothing is one way to deal with numerical instabilities, but excessive

smoothing of the terrain can result in unrealistic flows.

1.3 Turbulent Kinetic Energy Budget in Complex Terrain

In mountainous terrain, accurately representing boundary layer turbulence is important, where the exchange processes between the atmospheric boundary layer (ABL) and surface are highly impacted by the complexity of the terrain (Rotach & Zardi, 2007). Turbulence characteristics within the ABL over complex terrain are strongly influenced by the level of heterogeneity of terrain, diversity in surface cover and vegetation type, and wind flows (Rotach & Zardi, 2007; Dewekker & Kossmann, 2015; Lehner & Rotach, 2018; Solanki *et al.*, 2019).

TKE gives immediate information about the state of the ABL via the Obukhov length, reflecting the balance between mechanical production and buoyant production, or dissipation of turbulence in a horizontally uniform surface layer (Panofsky, 1984). While over horizontally homogeneous terrain, turbulent energy is predominantly driven by buoyant production, on windy days, shear production is relevant near the surface. However, over complex terrain, both buoyant and shear productions contribute to TKE. Shear production becomes the major source of TKE during periods of robust up-valley winds (De Franceschi *et al.*, 2009). Interactions between up-valley winds and winds aloft (e.g. cross ridge flows) generate both vertical and horizontal wind gradients, leading to strong afternoon shear production, and contributing to TKE at the surface (Weigel & Rotach, 2004; Weigel *et al.*, 2007a). Additionally, horizontal gradients in wind speed associated with up-valley wind contribute to horizontal shear production in complex terrain (Goger *et al.*, 2018).

Non-local sources of TKE, other than shear production, have been identified. Vecenaj *et al.*, (2011) found mountain wave-induced turbulence during a mountain wave event in Owens Valley, California, resulted in higher TKE on the sloping western part of the valley compared to the valley center. They attributed this to the advection of TKE by the mountain-wave activity, which played an important role in TKE production over the

western slope. Rai *et al.* (2017) using LES found horizontal TKE advection to be relevant in complex terrain, with horizontal shear production showing a similar magnitude as vertical shear production. Correct parametrization of boundary layer turbulence, represented by TKE, is important in high resolution simulations within complex terrain. This understanding is crucial when utilizing the turbulent state for applications such as wind energy, hydrological modeling, or comprehending and predicting exchange processes and evapotranspiraton.

1.4 The Impact of Heterogeneity of Complex Terrain on Surface Turbulent Fluxes

The Alpine Natural Subregion includes the highest elevations in Alberta, and has cold, dry and short summers with the highest annual mean precipitation of all subregions in Alberta, which falls mainly as snow throughout the non-summer months (Downing *et al.*, 2006; strong, 1992). Although precipitation is abundant in non-summer seasons, strong orographic winds would likely cause a moisture deficit, and make the region sub-humid and semiarid (Strong, 1992). This region is characterized by low growing vegetation in complex patterns due to a variable harsh microclimate produced by wind exposure, differing elevation, and snow deposition patterns (Willoughby *et al.*, 2006; Downing *et al.*, 2006). Thus, this characteristic vegetation cover, and gradients in cover with altitude, will have complex interactions with the dominant abiotic controls on evaporation such as radiation regime, topography and aspect, and turbulence (Zhao & Liu, 2014; Goulden *et al.*, 2012; Baily *et al.*, 1990).

The effect of horizontal inhomogeneities on vertical flux exchange has recently been the subject of studies in the past few years (Rotach *et al.*, 2015; Rotach & Zardi, 2007). Namely, dynamically and thermally forced winds (meso and sub-meso scale, i.e. plain to mountain wind systems, valley, and slope winds) modify the rate at which the flux exchange happens from non flat surfaces (Rotach *et al.*, 2015). Several ideal simulations considering topographical inhomogeneities showed that the valley wind system can amplify the vertical exchange of mass by a factor of between 1.2 to 2.8 (Wagner *et al.*, 2015). Lang

et al. (2015) simulated a deep valley surrounded by a variety of mountain range, and found three-fold enhancement of mass exchange when compared to the reference plain simulation. The process of mountain venting and other thermally-driven circulations, such as cross-valley flows, contribute to both vertical and horizontal transport of moisture, pollutants, temperature and turbulence to altitudes surpassing 1000 m above mountain tops (Henne *et al.*, 2004; Serafin *et al.*, 2018).

Heat and evaporative exchange processes at the land surface have long been recognized as one of the most important processes in the determination of the exchanges of energy and mass among the hydrosphere, atmosphere and biosphere (Brutsaert, 1982). Variations in terrain characteristics such as topography define the relationship between local mountain circulations, turbulent characteristics, and the efficiency of exchange processes (Rotach *et al.*, 2017). Advection due to surface roughness heterogeneities (Saunders & Bailey, 1994; Olyphant & Isard, 1987), diurnal valley winds (Schmidli, 2013), and mountain venting (Henne *et al.*, 2005) in high mountain regions introduce horizontal and slope parallel transport of heat and moisture disturbances, resulting in loss or enhancement of vertical turbulent fluxes.

From a modeling perspective, even when slope effects on vertical exchange are resolved using high-resolution LES, subgrid-scale variability of terrain can significantly impact turbulent exchange, which are parametrized at best using Monin–Obukhov similarity theory (MOST) developed for flat terrain (Stiperski & Rotach, 2016). The geometry and slope along the valley modify available solar energy, influencing the turbulent structure of the valley flow, and consequently turbulent fluxes (Rotach *et al.*, 2017). Surface turbulent fluxes of sensible and latent heat depend on available radiative energy; the timing and spatial variability of the sensible heat flux is strongly controlled by net radiation, while the magnitude of the flux is highly dependent on local terrain characteristics such as advection or vegetation cover (Rotach *et al.*, 2008).

While field campaigns have focused on heat fluxes, their horizontal and vertical transport, and turbulent structure of boundary layer, most studies have been performed in homogeneous conditions over flat terrain. Mountainous terrain introduces differential solar heating and shading, local flows, and heterogeneity in soil moisture, heat and evaporative fluxes depending on elevation and vegetation cover (Pomeroy *et al.*, 2003; Kafle &

Yamaguchi, 2009; Kiemle *et al.*, 2011; Rotach *et al.*, 2015; Zhao & Aining, 2015; Li *et al.*, 2018). The resulting spatial heterogeneity of fluxes limits our understanding of the important factors in controlling evaporative processes in mountainous terrain.

1.5 Objectives

Therefore, given the complexity of the relation and interactions between thermally induced diurnal winds, turbulence and heat and evaporative fluxes, the research goal of this thesis is to utilize LES to resolve daytime thermally driven flows and near-surface atmospheric variables in mountainous terrain. Next, using results from LES and observations, the variability of TKE and TKE budget terms , as influenced by thermally driven flows, with elevation and topography for a sunny fair weather summer day is explored. Finally, due to computational costs, observations providing longer term data for two months of summer were used to study the impact of complex topography on the sensible heat and evaporative fluxes with variations in soil moisture content, net radiation, turbulence, and wind flows.

The objectives are as follows:

1. Determine the optimal simulation set up by evaluating the effect of grid resolution, and orography smoothing on model predictions, and use the best model configuration to investigate the impact of topography on local flow features, and near-surface boundary layer processes.

2. Use the optimal model configuration to investigate the sources of TKE by studying TKE and TKE budget terms at different topographic locations.

3. Quantify the influence of elevation dependent topographical features on the near-surface sensible heat and evaporative fluxes.

1.6 Thesis Structure

This dissertation follows a manuscript-based thesis format that comprises 5 chapters. Chapter 1 introduces the research topic, the context for the research goals, and the three

objectives of this study. Each objective is addressed individually by chapters 2-4.

Chapter 2: "High-Resolution Large-Eddy Simulations of Flow in the Complex Terrain of the Canadian Rockies" (Rohanizadegan *et al*, 2023) addresses objective one, and evaluates the best model configuration against observations obtained from meteorological stations and SODAR over the complex terrain of the Fortress Mountain and Marmot Creek research basins, Kananaskis Valley, Canadian Rockies, Alberta in mid-summer.

Chapter 3: "Analysis of Turbulence and Turbulent Kinetic Energy Dynamics in Complex Terrain" (Rohanizadegan *et al.*, 2024, in review) addresses objective two, and discusses ABL structure and turbulence in three locations in Fortress Mountain research basin. The sources of TKE are investigated with a detailed TKE budget analysis.

Chapter 4: "Influence of Elevation Dependent Heterogeneity on Heat and Evaporative Fluxes in Complex Terrain" (will be submitted to Agriculture and Forest Meteorology) discusses the influence of elevation dependent topographical features (i.e soil moisture, solar heating,vegetation, turbulence and wind flows) on the near surface exchange processes (i.e sensible and latent heat fluxes).

Finally, Chapter 5 concludes the thesis by summarizing the key results of the research. It also discusses some of the limitations on the current work and addresses areas of research scopes.

Chapter 2

High-Resolution Large-Eddy Simulations of Flow in the Complex Terrain of the Canadian Rockies

[1]

2.1 Introduction

Mountains interact with the atmosphere primarily through the atmospheric boundary layer (ABL) that extends up to a few km above ground level (AGL). Mountainous terrain is frequently exposed to topographic wind flows, which are produced by orographic lift of incoming mesoscale and strong prevailing winds (Whiteman, 2000). Under weak synoptic conditions thermally-driven flows are also a common phenomenon in mountainous terrain, and are generated by horizontal contrasts in heating and cooling that arise from horizontal differences in temperature of the land and atmosphere due to diurnal differences in insolation (Lehner & Rotach, 2018; Serafin *et al.*, 2018). These thermally-induced flows are responsible for generating slope and valley flows (Schmidli & Rotunno, 2010; Rotach *et al.*, 2015), and can develop different flow characteristics depending on the geometry of valleys

and surrounding topography (Wagner *et al.*, 2015).

Predictions of surface phenomena in mountains are affected by complex orography, and is identified as a challenge for numerical modeling. Many attempts have occurred in recent years to improve the accuracy of numerical weather prediction (NWP) models to resolve flow in mountainous terrain by increasing grid resolution (e.g. Vionnet *et al.*, 2015; Udina *et al.*, 2017; Goger *et al.*, 2018), applying high-resolution land use and orography (Kalverla *et al.*, 2016; Jimenez-Esteve *et al.*, 2018; Golzio *et al.*, 2021), or improving soil moisture representation (Chow *et al.*, 2006). Weigel *et al.* (2007) modeled the contributing factors to the exchange of moisture in the Rivera Valley, Switzerland, and noticed that when the valley was resolved poorly, the cumulative daytime exchange was underestimated by a factor of three. Thus, the accuracy and resolution of the model is of great importance for resolving local flows in the valley and over slopes. Resolutions less than 100 m are recommended for simulating thermally-driven flows using LES (Cuxart, 2015).

LES modeling introduces an improvement upon subgrid parametrizations for eddies of all scales in Reynolds-Averaged Navier-Stokes (RANS) simulations (Chow *et al.*, 2013). LES resolve flow patterns by resolving larger scale eddies explicitly, and modeling smaller scale eddies containing smaller fractions of energy using turbulence closure models. Advances in computational resources have made high-resolution LES more accessible, and there are a number of studies that have used a turbulent resolving LES mode in ideal cases (e.g. Moeng *et al.*, 2007; Kirkil *et al.*, 2012; Mirocha *et al.*, 2014; Munoz-Esparza *et al.*, 2016; Arthur *et al.*, 2018). However, due to computational costs real case runs over mountains are still rare (e.g. Chow *et al.*, 2006; Rai *et al.*, 2017; Gerber *et al.*, 2018; Liu *et al.*, 2020; Umek *et al.*, 2021; Umek *et al.*, 2022; Goger *et al.*, 2022).

The development of nesting capabilities in NWP models has permitted application of new techniques to be investigated, such as transitioning from mesoscale to microscale regimes to obtain higher-fidelity turbulence information while preserving large scale forcing (Munoz-Esparza *et al.*, 2014; Wiersema *et al.*, 2020). Results have shown some advantages for simulating turbulence at small scales while avoiding the gray zone (terra incognita regime, 1 km - 100 m) (Wyngaard, 2004; Chow *et al.*, 2019), and provide better predictions for surface variables and wind flows in complex terrain. To appropriately resolve slope and valley flows in mountains at high-resolution, LES are required along with high-

resolution land use and topographic data. The Weather Research and Forecasting (WRF version 3.7.1) model (Skamarock *et al.*, 2008), while intended for mesoscale atmospheric simulations, has a nesting feature, in addition to its LES capabilities, designed to run on massive parallel computers. It incorporates real world land use, topography, and regional scale meteorological data that are easily imported into the model.

The main objective of this experiment is to utilize LES to resolve and analyze differences in daytime thermally-driven flows and near-surface atmospheric variables associated with two mountainous terrains with different valley volumes and surrounding orography during the snow-free season of a cold region, partly forested, high alpine environment. The study evaluates the effect of grid resolution, orography smoothing, and cloud parameterization resolution on model predictions to identify the best model configuration, which is then used to investigate the impact of topography on local flow features, air temperature and moisture, and cold-air pools.

2.2 Methodology

Simulations in this study, are focused on daytime convective conditions and predictions of thermally-driven flow and meteorological parameters. The model performance for a global smoothing option to alleviate the numerical issues with steep terrain was compared to a local filtering algorithm, and a mesoscale one-dimensional planetary boundary layer (PBL) (turbulence is fully parametrized) simulation. The model domain and data used are described below.

2.2.1 Study Area and Data

The study area is located over the eastern side of the Canadian Rocky Mountains in the Kananaskis Valley, Alberta (Figures 2.1 and 2.2), which are characterized by a variety of steep slope angles and valleys. This experiment focused on two heavily instrumented mountain basins: Fortress Mountain Research Basin (FMRB) (50° 50′ N, 115° 13′ W) and Marmot Creek Research Basin (MCRB) (50° 57′ N, 115° 09′ W). FMRB (Figure 2.1c)

contains wind scoured elevations of approximately 2099 to 2565 m. The alpine zone consists of two main ridges: Fortress and Canadian Ridges both oriented in SW-NE direction. Fortress Ridge has an elevation of about 2300 m, adjacent to a shallow valley at an elevation of 2000 m and orientation of 260° W, that is located in between Fortress and Canadian ridges. Canadian Ridge has an elevation of about 2211 m, and average slope of $\approx 15°$ with some areas of $\approx 35°$ (Harder *et al.*, 2016), while the mountain peaks exceed angles of 45°. Vegetation cover varies with elevation with shrubs and discontinuous coniferous forests at lower elevations (valley in between the ridges and slope sides) to alpine short grass (5-50 cm) at higher elevations (ridge tops), and bare alpine rocks at the steep slopes at highest altitudes. MCRB (Figure 2.1d) contains a greater variety of elevation ranges, from 1600 m in the large U-shaped Kananaskis Valley located east of MCRB to 2825 m at the summit of Mount Allan (Fang *et al.*, 2013). Slope variation and vegetation in MCRB are similar to FMRB with the exception of more dense forests and milder topography at middle elevations, and an open, grassland valley floor to the east.

Simulations were verified using data collected by Sonic Detection And Ranging (SODAR) on 18 and 19 July, 2016, from a flat surface on a ridge top at the east end of FMRB study area (Figure 2.1c) for remote measurements of the three-dimensional profiles of wind speed and direction in the lower portion of the atmospheric boundary layer (i.e. < 500 m). SODAR emits a number of acoustic pulse sweeps in each direction (north, east, south, west, and vertical) set to operate at a single frequency mode (1650 to 2750 Hz) (MFAS). Output resolution of vertical profiles were at 10 m intervals for heights 30 - 500 m AGL. Data was quality controlled and processed by APRUN software (Scintec, Germany), which determines wind speed and direction by examining the spectrum of backscattered wave for each cycle of SODAR sweeps.

Additional verification data were obtained from 13 meteorological stations (Figures 2.1b and 2.1c) located on ridge tops, valleys and a variety of aspects, slopes, and elevations at both FMRB and MCRB sites, and Burstall Pass (BRP) located northwest of FMRB (Table 1). Meteorological stations include measurements of surface wind speed and direction (RM Young, Campbell Scientific, USA), incoming and outgoing longwave and shortwave radiative fluxes measured by CNR4 (Net radiometer, Kipp and Zonen, Netherlands), and surface temperature and humidity (Rotronic sensors, Campbell Scientific, USA). Turbu-

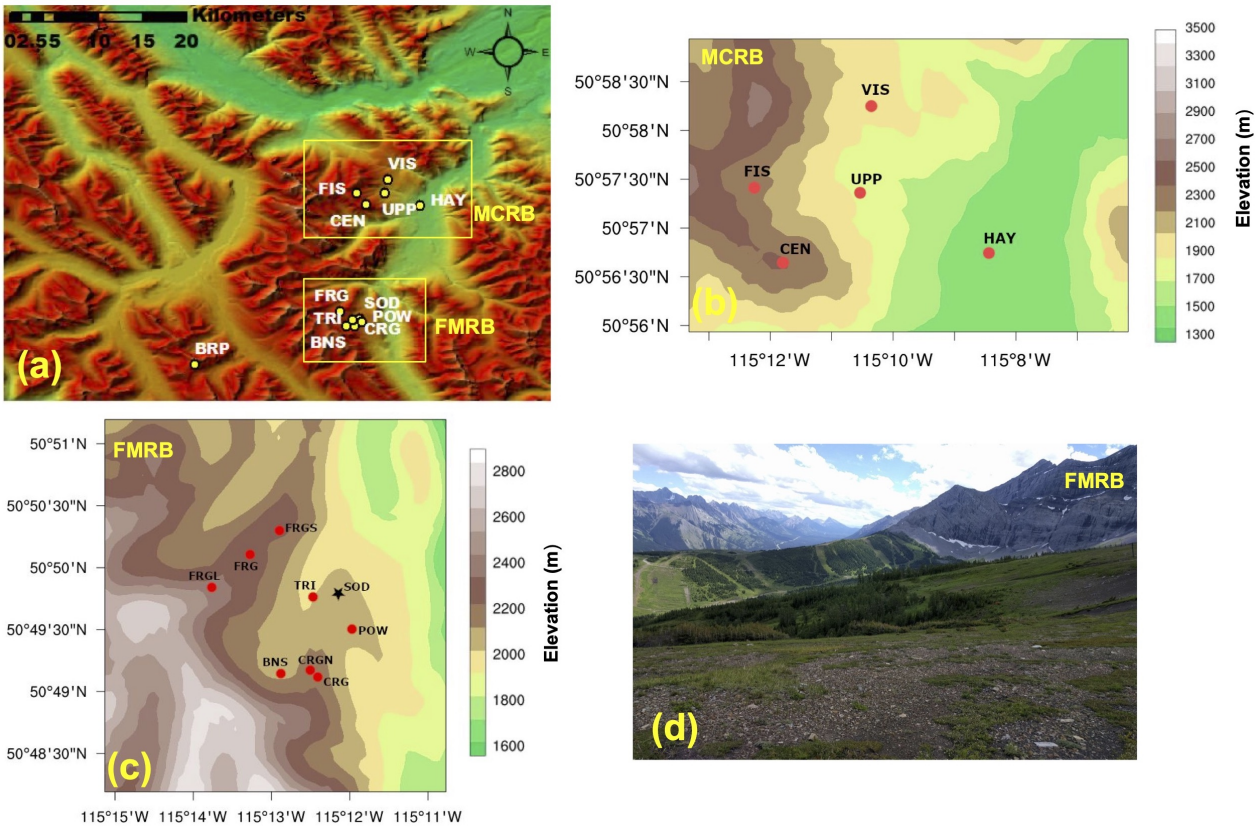

Figure 2.1: (a) Orography of the study area ($\Delta x = 90$ m) derived from the USGS dataset. The locations of meteorological stations at Marmot Creek Research Basin (MCRB), Fortress Mountain Research Basin (FMRB), and Burstall Pass Station (BRP) are marked by yellow circles; (b) The FMRB stations (locations indicated by points, and SODAR with a star), at 90 m grid spacing; (c) Similar to (b) but for MCRB area; (d) A picture of FMRB area from an eye view located near the FRG station, showing the valley area and a view of the Canadian ridge top (locations of CRG and CRGN stations).

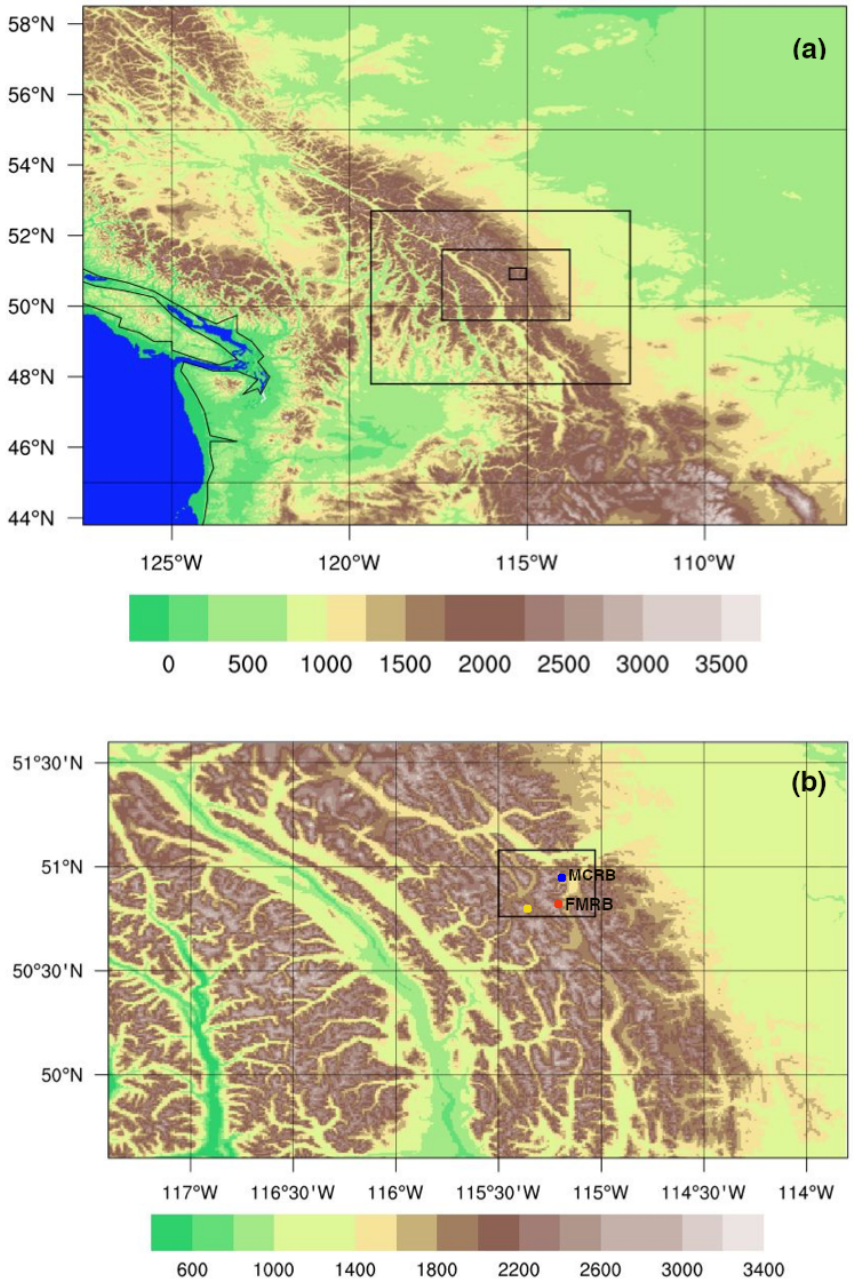

Figure 2.2: (a) Mesoscale domains (D1-D3) at 8.1 km, 2.7 km, 0.9 km grid spacing, respectively, and the innermost nested LES domain (D4) at resolution of 90 m; (b) D3 mesoscale domain at 0.9 km resolution containing LES domain (D4) at 90 m grid spacing. The blue (MCRB), red (FMRB), and yellow (BRP) circles denote the location of study areas.

Table 2.1: List of meteorological stations with coordinates and elevation in FMRB, MCRB, and BRP, Kananaskis Valley, Alberta, Canada, shown in Figures 2.1b and 2.1c.

Site	Name	Latitude (°N)	Longitude (°W)	Elevation (m)	Sensor height AGL (m)
FMRB stations					
TRI	Tripod (north-west-facing slope)	50.8278	-115.2077	2060	2
BNS	Bonsai (valley floor)	50.8210	-115.2141	2099	5
SOD	SODAR (ridge top)	50.8291	-115.2008	2117	30 - 500
POW	Power Line (ridge top)	50.8260	-115.1983	2136	5
CRGN	Canadian Ridge North (north-facing slope)	50.8217	-115.2066	2205	6
CRG	Canadian Ridge (ridge top)	50.8214	-115.2063	2211	3
FRGS	Fortress Ridge South (south-facing slope)	50.8382	-115.2157	2310	5
FRG	Fortress Ridge (ridge top)	50.8257	115.19672	2323	6
FRGL	Fortress Ledge (ridge top)	50.8300	-115.2286	2565	3
MCRB stations					
HAY	Hay Meadows (valley floor)	50.9441	-115.1389	1437	7
UPP	Upper Clearing (mid-level ridge top)	50.9565	-115.1754	1845	3
VIS	Vista View (ridge top)	50.9709	-115.1722	1956	3
FIS	Fisera Ridge (ridge top)	50.9568	-115.2044	2325	2.6
CEN	Centennial (ridge top)	50.9447	-115.1937	2819	2.5
BRP station					
BRP	Burstall Pass (ridge top)	50.7827	-115.3686	2317	10

lent characteristics and fluxes were measured by a CSAT3 sonic anemometer (Campbell Scientific, USA) located at the north-west-facing slope station, Tripod (TRI), in FMRB. High frequency wind speed measurements were detrended and block averaged over 30 min intervals for flux estimates after applying a double rotation scheme (Kaimal & Finnigan, 1994) to align the coordinates with the mean wind.

2.2.2 Horizontal and Vertical Grid

In order to capture turbulent flows in high-resolution, the model was configured with 4 one-way nested domains (D1 - D4), with a grid ratio of 3 at horizontal resolutions of 8.1 km, 2.7 km, and 0.9 km for the first three domains (Table 2). A grid refinement ratio of 10 was adjusted from D3 to D4 (Zhou & Chow, 2014) to avoid the gray zone associated

Table 2.2: LES model grid configurations for each domain.

Domain	Δx, Δy (m)	Grid points	Time step (s)
D1	8100	202× 202	1
D2	2700	202× 202	0.33
D3	900	271× 241	0.11
D4	90	401× 401	0.02

with eddies at scales of a few hundred meters at mesoscale down to three-dimensional LES (Wyngaard, 2004; Munoz-Esparza *et al.*, 2017).

The larger parent domain (D1) covers an area 2000 × 2000 km^2, containing nests D2 and D3 down to nested domain D4, focusing on the study area covering a 36 × 36 km^2 domain (Figure 2.2). Limits of domain D2, D3 and D4 were specifically designed to avoid steep terrain to minimize model stability issues. Topography for mesoscale domains D1-D3 was set to the 30 arc-sec (1 km) U.S. Geological Survey (USGS) datasets available in WRF. Topography for LES domain D4 was extracted from a 3 arc-sec (90 m) USGS dataset (Sertel *et al.*, 2010), and the land cover for domain D4 was obtained from CanVec land use database at 50 m resolution.

A horizontal to vertical grid aspect ratio ($\Delta x/\Delta z$) between 3 and 5 is recommended in the LES domain to effectively resolve the vertical structure of the atmosphere near the surface and avoid distortion of the eddies (Chow *et al.*, 2013). Vertical grids were distributed between ground level and 20 km (10 hPa) for a total of 80 levels stretched progressively from bottom to top of the model with a stretch coefficient of about 1.23 between the top levels. Below the first 1 km, 28 levels were used for all domains with $\Delta z_{min} = 20$ m to allow for resolving turbulent structures within the boundary layer height over complex terrain, and to avoid overestimation of low level jet and contamination from overly diffusive structures (Munoz-Esparza *et al.*,2017).

WRF uses a hydrostatic-pressure terrain-following vertical coordinate system, with stability issues arising from both the steepness of the terrain and grid aspect ratio (Daniels *et al.*, 2016). It was determined that numerical instabilities due to the amplification of numerical errors caused by grid distortion near the surface along steep slopes results in

vertical velocities violating the Courant-Friedrichs-Lewy (CFL) condition. To counteract numerical instability, some adjustments were applied. First, smoothing the terrain, increasing the time off-centering from WRF default of 0.1 to 1.0 that weights (forward in time) the vertically implicit acoustic-time-step terms in the model to dampen instabilities associated with sound waves propagating vertically in sloping model levels, and decreasing the time step were attempted. These solutions seemed to resolve the problem with numerical stability issues at the early start times in simulations, but continued to pose problems due to high lateral wind velocities over steep mountains in the simulations. To resolve this matter a 6th order diffusion option in WRF was applied to dampen the 2Δ waves, where Δ is grid spacing, for all variables in horizontal space (Knievel *et al.*, 2007).

2.2.3 Turbulence and Physics Parameterizations

Vertical mixing (eddy transport of vertical fluxes) in WRF is parametrized using one-dimensional PBL schemes. Mesoscale domains D1-D3 make use of the YSU PBL scheme (Yonesi University) (non-local treatment of turbulent eddies using a critical Richardson number) (Hong *et al.*, 2006) for vertical diffusion, and a two-dimensional Smagorinsky closure for horizontal eddy diffusivity (Smagorinsky, 1963). At the smallest model grid spacing in this study of 90 m for D4, LES aims to explicitly resolve the largest and most energetic eddies of the Inertial Subrange (Cuxart, 2015), with the assumption of cascade of energy to smaller sub-grid eddies, at which the turbulence is parametrized. In mountains, it is necessary to use fully three-dimensional turbulence schemes that represent observed small scale turbulent features occurring in a complex topography and relevant to resolving total kinetic energy (TKE) production in the valleys and slopes (Goger *et al.*, 2018). In this study a full three-dimensional local 1.5 order prognostic TKE diffusion closure was deployed in the LES domain (D4) (Lilly, 1966; Lilly, 1967).

Surface layer parametrization of Monin-Obukhov similarity theory (Monin-Obukhov, 1954) was set corresponding to specific PBL parametrization, and the LES surface layer was set to the revised surface layer scheme (Jimenez *et al.*, 2012). The surface layer scheme provides information on friction velocities and exchange coefficients to WRF's Noah-MP land surface model (LSM) (Niu *et al.*, 2011) to calculate the turbulent fluxes. For

cumulus parameterization, Kain-Fritsch (new Eta) (Kain, 2004) was used for the coarser domains, excluding the LES domain. Shortwave radiation was parametrized using the Dudhia scheme (Dudhia, 1989), which includes slope and shadowing effects on surface shortwave fluxes if corresponding namelist variables are activated. Longwave radiation was quantified using the rapid radiative transfer model (RRTM) (Mlawer *et al.*, 1997). The longwave scheme does not include corrections arising from slope effects on incoming longwave radiation, which is a shortcoming in applying WRF in complex terrain.

2.2.4 Boundary Conditions and Mesoscale Model Initialization

To determine the best forcing conditions to be applied to the LES domain, sensitivity experiments were performed for the mesoscale domains (D1-D3). Three reanalysis datasets were used for the sensitivity tests: (1) the North American Regional Reanalysis (NARR) at 32 km resolution and with 30 vertical levels and a three-hour time step (Mesinger *et al.*, 2006); (2) the Interim European Center for Medium-Range Weather Forecasts Reanalysis (ERA-Interim) at 77 km resolution, with 38 vertical levels and a six-hour time step (Dee *et al.*, 2011); and (3) the Environment and Climate Change Canada GEM-based High Resolution Deterministic System forecast (HRDPS) at a resolution of 2.5 km, with 28 vertical levels and an hourly time step (Fillion *et al.*, 2010). 5 PBL schemes for vertical mixing in the mesoscale domains were also analyzed: (1) YSU; (2) MYJ (Mellor-Yamada-Janjic) (Janjic, 1994); (3) MYNN (Mellor-Yamada-Nakanishi-Niino) (Nakanishi & Niino, 2006); (4) QNSE (Quasi Normal Scale Elimination) (Sukoriansky *et al.*, 2005); and (5) QNSE (a version of QNSE with non-local eddy diffusivity mass flux, EDMF). This combination of boundary datasets and PBL schemes generated 15 test cases in total to examine sensitivity. To evaluate the most accurate combination for initialization, hourly mean wind speed and wind direction for each of the vertical levels for both model 10 min output and SODAR 30 min datasets were calculated for the hours 7 am to 9 pm Local Time (LT). The mean root-mean-square error (RMSE) was then calculated for 27 vertical levels up to 300 m from ground level. RMSE is defined as

$$RMSE = \sqrt{\frac{1}{M}\sum_{j=1}^{M}\frac{1}{N}\sum_{i=1}^{N}(A_{ij} - B_{ij})^2} \tag{2.1}$$

where A_{ij} and B_{ij} are SODAR and simulation data, and M and N are the number of time steps and vertical grid points, respectively.

This analysis demonstrated that the combination of initial and boundary conditions from the HRDPS data set and all PBL schemes on average increased mean RMSE of wind speed by ≈ 0.6 m/s and wind direction by $\approx 2^\circ$ with respect to the other two reanalysis data sets. Combination of NARR data set and all PBL schemes resulted in a similar performance, with having reduced the errors by 10% for YSU PBL scheme. Combination of the NARR data set and QNSE PBL showed the largest error increased by 20%. Results for the two PBL schemes, YSU and MYNN, and in combination with the forcing data ERA-interim, showed the lowest mean RMSE for wind speed (≈ 0.45 m/s) and for wind direction ($\approx 11.5^\circ$). Combination of ERA-interim with the YSU PBL was selected for the mesoscale simulations (D1-D3) for being more computationally efficient.

Soil moisture and temperature from the meteorological stations in FMRB and MCRB for 18 and 19 July were compared to all three meteorological datasets (i.e. ERA-Interim, NARR, HRDPS). The lowest bias belonged to ERA-interim with mean negative bias value of -0.07 m^3/m^3 for moisture and $+1^\circ$ for temperature. Thus, ERA-Interim was chosen to initiate soil moisture and temperature at 4 soil model levels at ground level and 10, 30 and 100 cm below ground level.

2.2.5 Experimental Design

Domains (D1-D3) are mesoscale and use a PBL scheme for turbulence closure. Domain 4 uses an LES turbulence model to simulate the cascade of eddies from mesoscale to ABL convective scales, which are less than 100 m. WRF like most NWP models uses terrain-following coordinates, which can result in numerical errors in the approximation of velocity gradients over steep slopes, causing numerical instabilities. To avoid this problem

a global smoothing and local filtering approach was employed in which the local filtering only smoothed locations where the slope exceeds a given threshold.

The filters used in this study were: (1) global smoothing performed with a WRF smoother uniformly applied across all domains (D1-D4), hereafter referred to as LES with Global Filtering (LESGF); and (2) a local smoothing algorithm (Kosovic, 2020) applied to D4. Global smoothing was applied to the coarser domains (D1-D3). This setup was referred to as LES with Local Filtering (LESLF). The first option filters the terrain significantly by applying 15 smoothing passes to stabilize simulations over steep terrain, which results in removing lower elevation and valley features, and generating unrealistic flows. To improve upon removing lower elevation orography, a local filtering algorithm was also tested that selectively filters terrain at slopes $> 45\ ^{\circ}$ to alleviate numerical divergence stability errors arising from steep terrain-following hydrostatic pressure (sigma) vertical coordinates of WRF (e.g. Klemp *et al.*, 2007; Arnold *et al.*, 2012). Figure 2.3 illustrates the differences in point-to-point comparisons of ridge tops, valleys, and a slope, in which local filtering smooths steep mountains more than global filtering (altitude differences in points A, B and C, and slope angle), while global filtering removes more valley features, making the valleys deeper than reality (point E).

An additional LES with Local Filtering considers the impact of topographic shading and slope effects (LESLF_shade) on radiation by activating the namelist variables topo_shade and slope_rad in model setup. One more set up was also tested in which cumulus parametrization was activated only for the coarse parent domain, D1, in LESLF_shade_cloud simulations. The goal was to study the impact of model resolution on cloud fraction and radiation predictions when compared with LESLF simulations, which used cumulus parametrization for all domains except D4. All LES configurations utilized the Cell Perturbation (CP) method (Munoz-Esparza *et al.*, 2015), which is most suitable for generating smaller turbulent eddies. The CP method provides better predictions of vertical profiles of turbulent eddies, by applying finite amplitude perturbations of potential temperature along LES inflow boundaries that lead to fully resolved turbulence spectrum within a reduced fetch.

A mesoscale experiment, named PBL, was performed using YSU PBL for turbulence closure to compare with LES experiments. Domains (D1-D4) were configured similar to

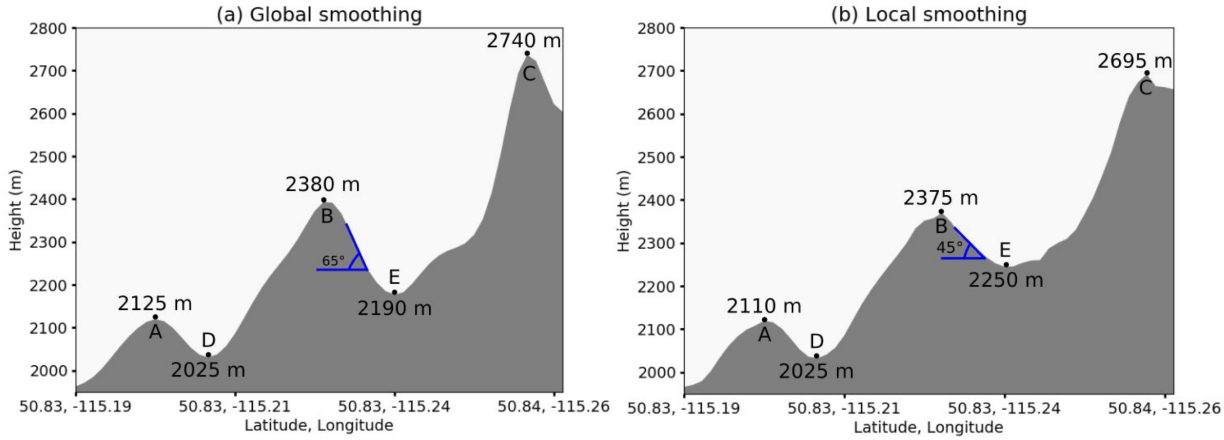

Figure 2.3: Example cross sections of global and local smoothing showing the differences in altitude of ridge tops, valleys, and a slope. Global filtering removes more valley features compared to local filtering, and local filtering smooths the steeper locations more than global filtering reducing the elevation of ridge tops.

LES experiments, except the resolution of domain D4 was set at 180 m. PBL experiments also used the topo wind namelist option that improves estimates of surface winds in mesoscale simulations and accounts for enhanced drag from sub grid topography in mountainous regions (Jimenez & Dudhia, 2012).

The choice of a suitable day for simulations was limited by the availability of sounding data on 18 and 19 July. Model forecasts are generally preferred for fair weather days with weak synoptic conditions (i.e. calm synoptic wind and clear skies) that represent the most unstable conditions, which are characterized by thermal flows. Typical wind speeds for upslope flows are between 1 and 5 m/s at a height of 20 to 200 m AGL (Zardi & Whiteman, 2013). On 18 July, wind speeds were generally lower and less than 5 m/s for most valley and ridge top stations, but forecasts were impacted by some periods of semi-cloudy skies. In comparison, 19 July had stronger mesoscale winds with wind gusts greater than 5 m/s reaching up to 12 m/s as observed at the ridge tops in FMRB and MCRB study areas. The stronger wind gusts can overwhelm more subtle thermally-driven local flows.

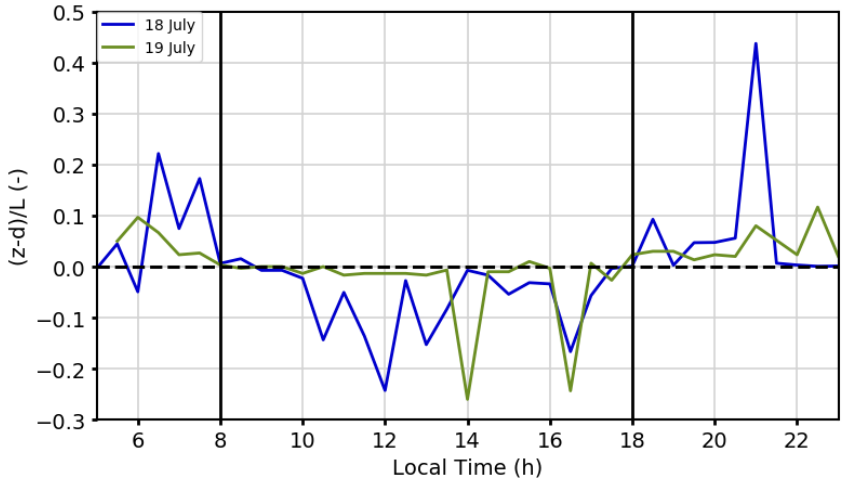

Figure 2.4: Time evolution of inverse Obukhov length (dimensionless: scaled with the sensor height and corrected with vegetation height) for 5 am - 11 pm LT on 18 and 19 July derived from turbulent fluxes measured by sonic anemometer at 2 m AGL at the TRI valley station.

The suitability of the chosen days for model simulations was narrowed down further by investigating the evolution of inverse Obukhov length (L) (Figure 2.4) calculated from the observed turbulent fluxes at the valley station (TRI) scaled with sonic anemometer height (z) and corrected with vegetation height (H) (Hogstrom, 1990), $(z-d)/L$, where d = 0.75 H $\approx$ 40 cm is the displacement height. After sunrise ($\approx$ 8 am LT at this location), the atmospheric boundary layer switched from stable ($(z-d)/L > 0$) to unstable conditions ($(z-d)/L < 0$) for both 18 and 19 July. $-0.5 < (z-d)/L < 0$ during unstable hours suggests that shear production was the dominant source for turbulent production (Wyngaard, 1973). Late afternoon boundary layer on both days resumed nighttime stable stratification ($(z-d)/L > 0$) after 6 pm. 18 July showed enhanced amplitude in shear and convective turbulent instabilities (10 am - 6 pm) that helps to drive valley and slope flows. To better evaluate model performance in thermally-driven flows, the rest of this paper is focused only on the 18 July forecasts.

All simulations for domains D1-D3 were initialized at 0600 UTC on 18 July to permit

6 hours of spinup period. Initial and boundary conditions for D4 were initialized from the output of D3 at 1200 UTC on 18 July to run concurrently after spinup period. Experiments were run for 16 hours physical time since the main focus of this study was on daytime flows (5 am - 9 pm LT). Frequent forecasting outputs were generated at time intervals of 10 min for the D4 domain for both LES and PBL simulations. Time series of some surface variables and vertical profiles of wind components, temperature, and water vapour were also output at every model time step at each meteorological station location. Since the instantaneous model output is not a full representation of the time dependent processes in the LES domain, the time series output was averaged for each 15 min interval to account for an ensemble of turbulent fluctuations. This makes it more comparable with measured surface variables averaged over the same period of time.

The setup above was computationally costly, which resulted in simulations requiring 12 hours CPU time for every 2.3 hours of physical time. This required 20 (720 cores) nodes/cores for the 4-domain simulations on the Cheyenne cluster at the NCAR supercomputer research facility.

2.3 Results and Discussions

The impact of LES with local filtering method, with and without topographic shading (LESLF_shade and LESLF, respectively), along with the results from simulations of local filtering LES with lower resolution cloud parametrization (LESLF_shade_cloud), global filtering LES (LESGF), and mesoscale simulations (PBL) on daytime air flow (5 am - 9 pm LT) for near-surface forecasts are compared to observations.

2.3.1 Time Series and Diurnal Cycle

The impact of topographic dependent vegetation, cloud and mountain shading, and elevation differences on radiation, slope and valley winds in complex terrain are investigated using surface time series at 4 different sites. The diurnal evolution of radiation, surface wind speed and direction at valley and ridge top stations are presented as follows: Bonsai

(BNS) and Power Line (POW) stations in FMRB, and Hay Meadow (HAY) and Fisera Ridge (FIS) stations in MCRB (Figure 2.1 and Table 2.1). The valley station (BNS) is located on the valley bottom, while the ridge top station (POW) is on a gentle slope ($<$ 10°) rising to the northeast. BNS and POW are considered "sheltered" sites as they are 15 m diameter clearings surrounded by coniferous forests, in addition to mountain ridges providing topographic shading at the valley site. In MCRB, the valley station (HAY) is located on the valley bottom, while the ridge top station (FIS) is on a level ground, with a ridge located to the west that slopes upward to the west. Land cover at HAY and FIS consists of sparse grass and bare ground located in a well exposed wide valley and high ridge top, respectively and so are considered "open". The vertical profiles and time series of wind speed and direction are also evaluated against SODAR for the simulated day, 18 July.

Radiation

Figure 2.5 illustrates simulated and observed surface net radiation and biases for each set of model configurations and observations. In mountainous areas, the surface radiation budget is modified by topographic shading and cloud cover (Zardi & Whiteman, 2013). All simulations showed some degree of overprediction of radiation in the early hours at all locations, with the highest overprediction seen at the sheltered ridge top station (POW) in FMRB. In the afternoon, at BNS, LESLF_shade_cloud and PBL overestimated radiation, while the rest of the simulations underestimated radiation by about $\pm$ 400 W/m^2. Similarly, at POW and open valley station (HAY), all simulations underestimated radiation, but LESLF_shade_cloud closely followed observations at both locations. At the open ridge top (FIS), all the simulations except LESLF_shade overpredicted radiation for various durations.

The discrepancies between the model predictions and observations of radiative fluxes especially early in the day are attributed to several factors, including orographic smoothing and the subsequent modulations in shortwave fluxes. Differences in elevation between LES results and reality may have contributed to the inconsistencies in predictions of radiative fluxes, which varies from none at the mid-altitude station, Upper Clearing (UPP), in

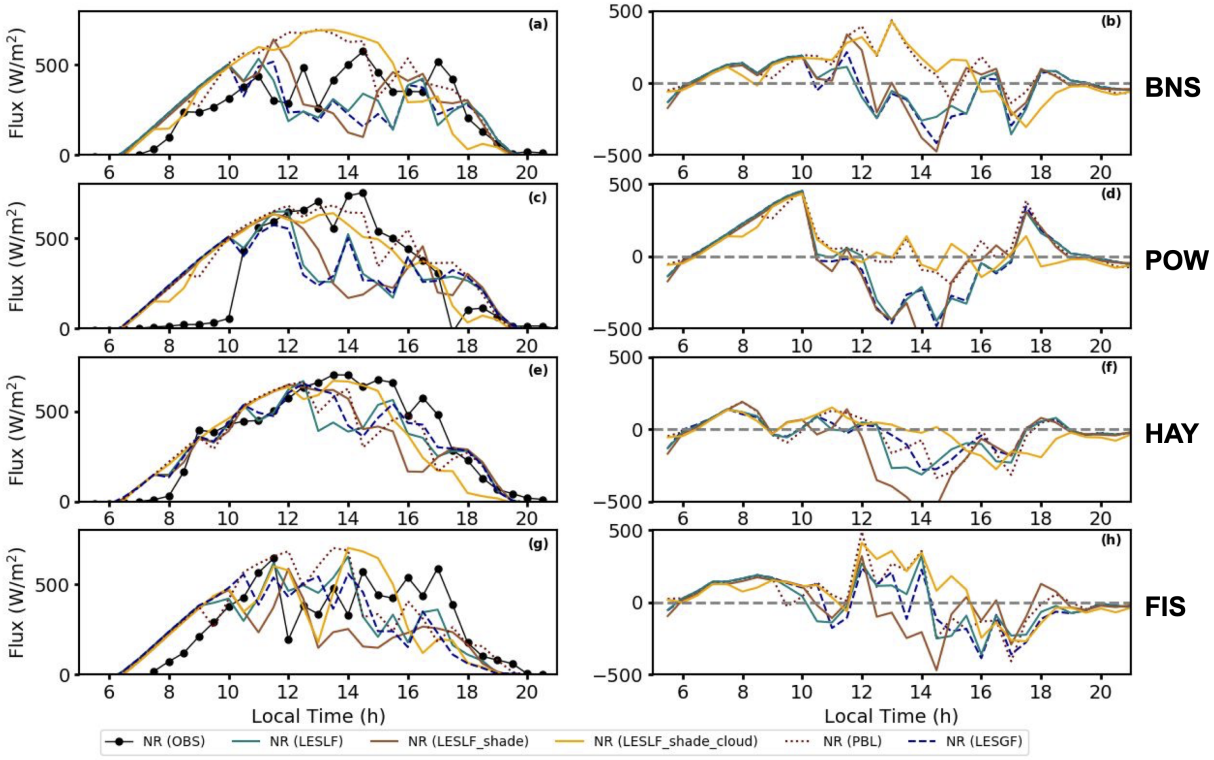

Figure 2.5: Net radiation fluxes (net shortwave and longwave radiation) (left), and biases between each model configurations and observations (right) at the sheltered valley (BNS, a, b), sheltered ridge top (POW, c, d), open valley (HAY, e, f), and open ridge top (FIS, g, h) stations.

MCRB to about 423 m at the ridge top station, Centennial (CEN), in MCRB.

The effect of topographic shading during a day with cloudy periods is difficult to ascertain from the current results. That is, in some instances LESLF_shade followed the observed fluxes better than LESLF, and vice versa. The sudden rise in the observed net radiation after sunrise in the valley sites (BNS and HAY) indicated shadowing by the surrounding mountains. At POW, sunrise occurs approximately two hours later than at the sheltered valley station (BNS) in the morning. The early morning lag in radiative flux measurements persisted over the summer months at POW, indicating that topographic shading by the slope rising to the northeast is responsible for the sunrise lag at this location. Simulations failed to follow observations possibly due to misrepresentation of the orography in the simulations. Additionally, short-lived cumuli (i.e. ground level up to 700 hPa) reduce the amount of shortwave flux received by the surface, and modify heat and moisture fluxes. Hence, their correct representation in high-resolution simulations is crucial for accurate predictions of radiation, and local wind flows in complex terrain. Nonetheless, LESLF_shade_cloud model with the lower resolution in cloud parametrization (activated only in the first coarse domain D1), overall is the most successful in predictions of radiative fluxes. The analysis confirms that nested high-resolution runs can be affected by the incorrect input for convection processes from the coarser domains (i.e gray zone), suggested by other studies (e.g. Jeworrek *et al.*, 2019), resulting in incorrect predictions of clouds in the finer resolution LES domain.

Potential Temperature, Wind Speed and Direction

In Figure 2.6a simulated vertical profiles of potential temperature at three different timestamps chosen to correspond with SODAR observations are compared to illustrate the evolution of the ABL during daytime hours. At 9 am LT, simulations showed a developing mixed layer near the ground in the potential temperature profile at approximately 100 m above ground. Above this mixed layer the atmosphere is stably stratified. In the afternoon, the atmosphere revealed a well-mixed layer, indicating a convective ABL due to warming up of the surface layer. In the late afternoon, a stable ABL seemed to be establishing, evident in the corresponding potential temperature profile.

Figure 2.6b, 2.6c, 2.6d, and 2.6e compare simulated wind speed and direction with SODAR profiles for 30 - 500 m AGL. For the sake of consistency, wind speed profiles are made using the output of an integrated data collection of 8 min in each cycle of SODAR sweeps, and time-averaged fluctuations of model output for the same time interval of SODAR cycle. SODAR profiles suffered from incompleteness and low measured heights in some measurement cycles (i.e. < 300 m) possibly caused by strong low level winds or lack of turbulence and temperature gradients, which often happen during morning and evening transitions. The progression of vertical profiles have been arranged to show examples of the flow at the SODAR location from afternoon of 18 July, when sounding measurements reached a height of more than 400 m AGL for better evaluation.

At 2:30 pm LT, PBL and LESLF_shade_cloud predicted the flow direction most successfully, but wind speed was either underestimated or overestimated by all simulations at various heights above ground, except PBL which was most successful in predicting the low-level jet at this time. The late afternoon (7:50 pm LT) wind profile observation from SODAR revealed that near-ground winds remained at approximately 180 - 200°. None of the simulations were quite successful in predicting wind direction, and deviations are $<$ 80° at below 200 m. LESGF was the most successful in predicting wind speed at this time except near the ground, and LESLF_shade_cloud followed observations closely in between 50 and $\approx$ 400 m above ground.

Time series evolution of wind speed and wind direction illustrates model performance with different configurations at 40 m AGL (Figure 2.7). Suitable SODAR observations were available for only a portion of 18 July. The simulated time series of wind speed for the LES results showed a progressive growth in amplitude of wind speed fluctuations from morning to the afternoon. This is consistent with the growth of a mixed boundary layer (Figure 2.6a), which is corroborated by SODAR observations. PBL model also showed growth in amplitude of fluctuations in horizontal wind speed from morning to the afternoon, but displayed higher RMSE than LESLF simulations (Table 3). LESLF_shade_cloud presented the best performance (Figure 2.7b), and the lowest RMSE for wind direction compared to the rest of simulations (Table 3).

To study the thermally-driven flows at each of the station locations, model output for wind speed and wind direction at 10 m AGL were compared to station data collected at

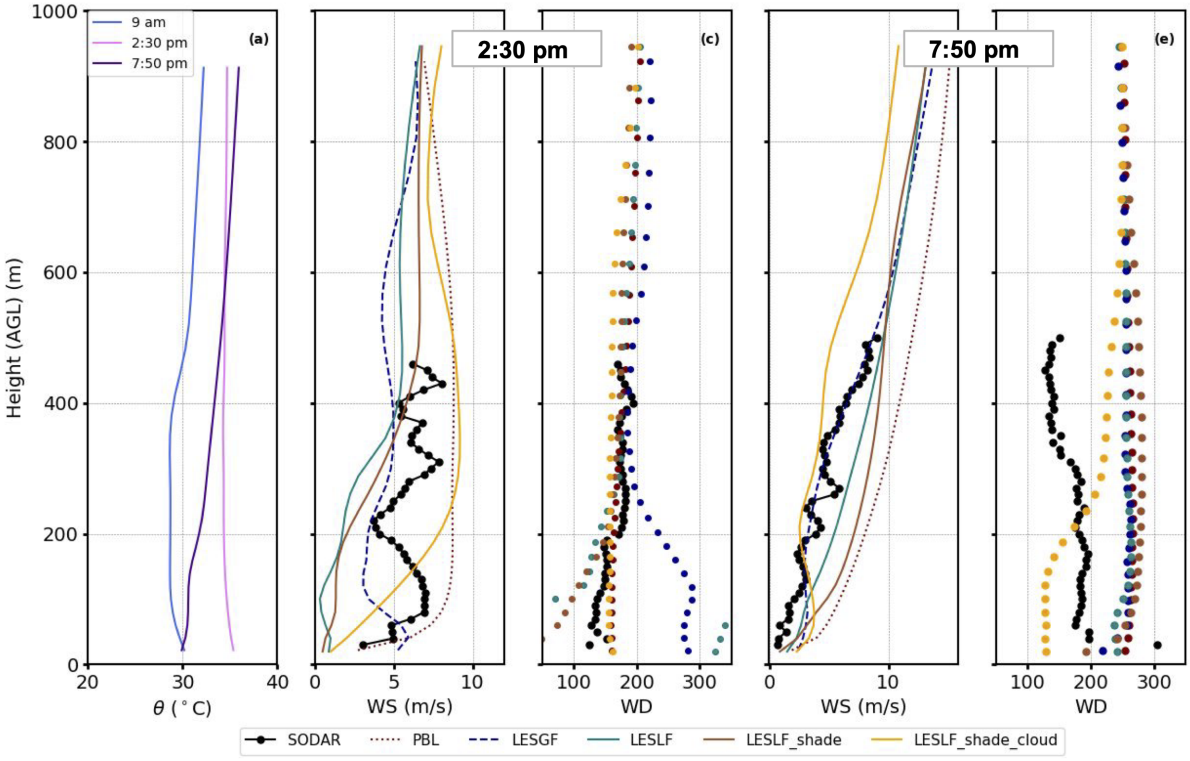

Figure 2.6: (a) Vertical profiles of potential temperature showing the evolution of ABL at 9 am, 2:30 pm, and 7:50 pm LT. (b, c, d, e) The 2:30 pm, and 7:50 pm LT (18 July) vertical profiles of SODAR, compared with LESLF_shade_cloud, LESLF_shade, LESLF, LESGF and PBL WRF simulations of wind speed and wind direction.

Table 2.3: Root-mean-square errors (RMSE) for wind speed (m/s), and wind direction (°).

MODEL	WS	WD
LESLF_shade_cloud	3.3	72
LESLF_shade	2.9	104
LESLF	3.2	109
LESGF	3.3	144
PBL	4	90

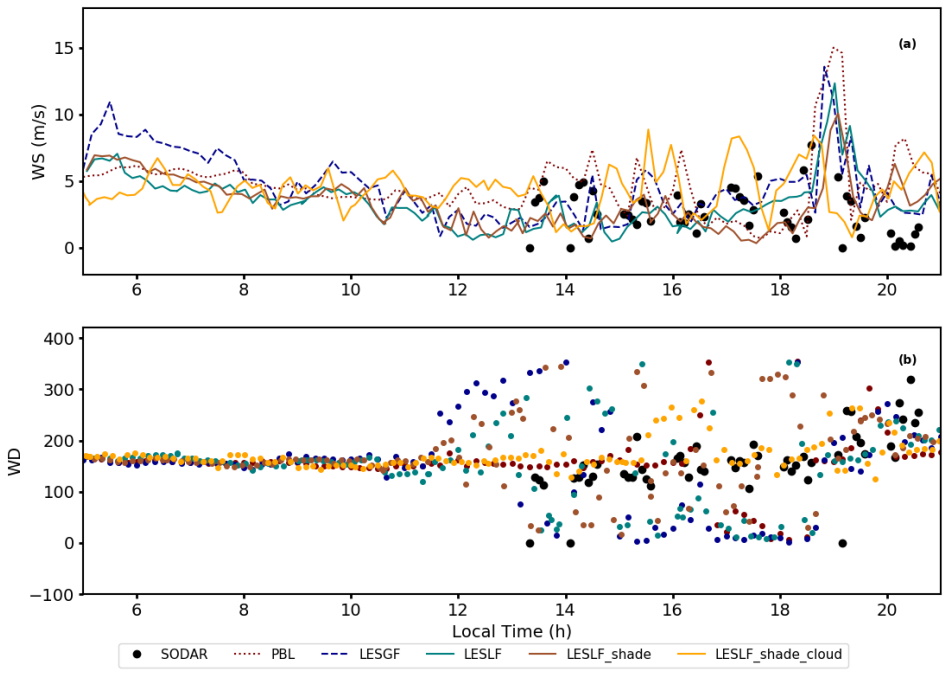

Figure 2.7: Time series evolution of wind speed and direction at 40 m AGL on 18 July (a, b).

various instrument heights (2-10 m AGL). To avoid discrepancy between differing model and sensor height measurements, model forecasts were corrected to the sensor height using a logarithmic wind profile under the assumption of a neutrally stratified atmosphere. Due to complexity of terrain at these sites, wind speed and direction vary in different patterns for each of the station locations.

At the BNS sheltered valley station in FMRB (Figure 2.8), wind speed remained consistently low, below 2 m/s, after sunrise at 8 am, with a slight increase in the afternoon. The dominant wind was down-valley ($\approx$ 150 - 250°) before noon, and started to turn into an up-valley flow after 11:30 am. The surface flow at BNS switched between up-valley (300 -350 and 0 - 50°) and down-valley the rest of the day, until after sunset at 7 pm when it eventually turned back to down-valley. LESLF simulations showed improvement in predicting wind speed ($RMSE = 0.6$ m/s), when compared to PBL ($RMSE = 0.9$ m/s) and LESGF ($RMSE = 1.0$ m/s). All simulations had difficulty with wind direction predictions in some instances throughout the day, but all simulations except LESLF_shade_cloud and PBL predicted the transition from down-valley to up-valley more successfully. The difference in wind direction pattern between the model and observations throughout the day might suggest that in reality, wind direction followed a complex pattern because of sub-canopy turbulence and the impact of surrounding topography. In sheltered sites, wind direction can be affected by turbulent fluctuations caused by under-canopy turbulence (Conway *et al.*, 2018). Sub-canopy turbulence and flow reversals are characteristics that can cause frequent and sudden changes in wind direction. It is noted that the model does not represent the effect of shading by vegetation on surface parameters. There is also high variability in surface vegetation heights in surrounding terrains, and a wide range in aerodynamic roughness length ($z_0 = 0.06$ - 1.1 m) that the current model resolution does not capture.

At the ridge top sheltered site in FMRB, POW (southeast-facing slope) (Figure 2.8), wind speed was very low in the very early hours before sunrise, but increased after 7 am and changed direction from the very weak drainage flow, possibly dampened by the surrounding vegetation ($\approx$ 300 - 350 and 0 - 50°), to upslope ($\approx$ 200°) during daylight hours. This persisted until about 7 pm before returning to downslope again at sunset. All simulations provided similar predictions for wind speed and direction, except in the early

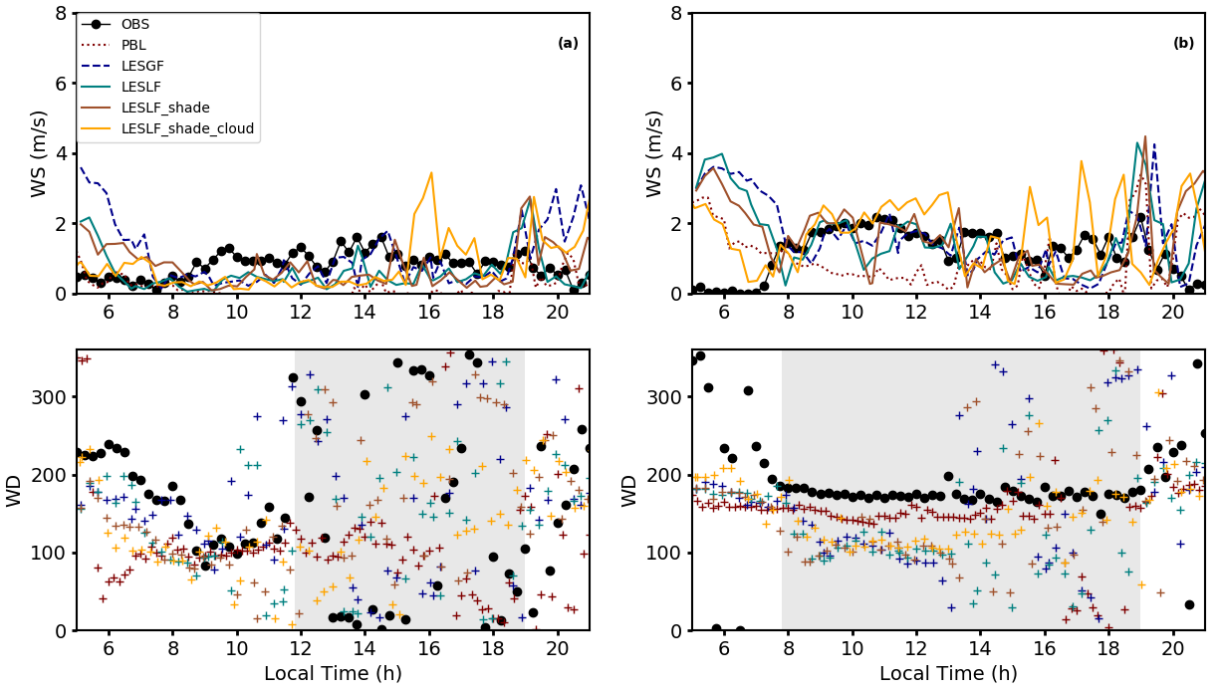

Figure 2.8: Surface wind speed and direction at the sheltered valley (BNS, a) and ridge top (POW, b) stations located in FMRB. The shaded areas highlight the periods in which the flow was essentially up-valley at BNS, and upslope at POW.

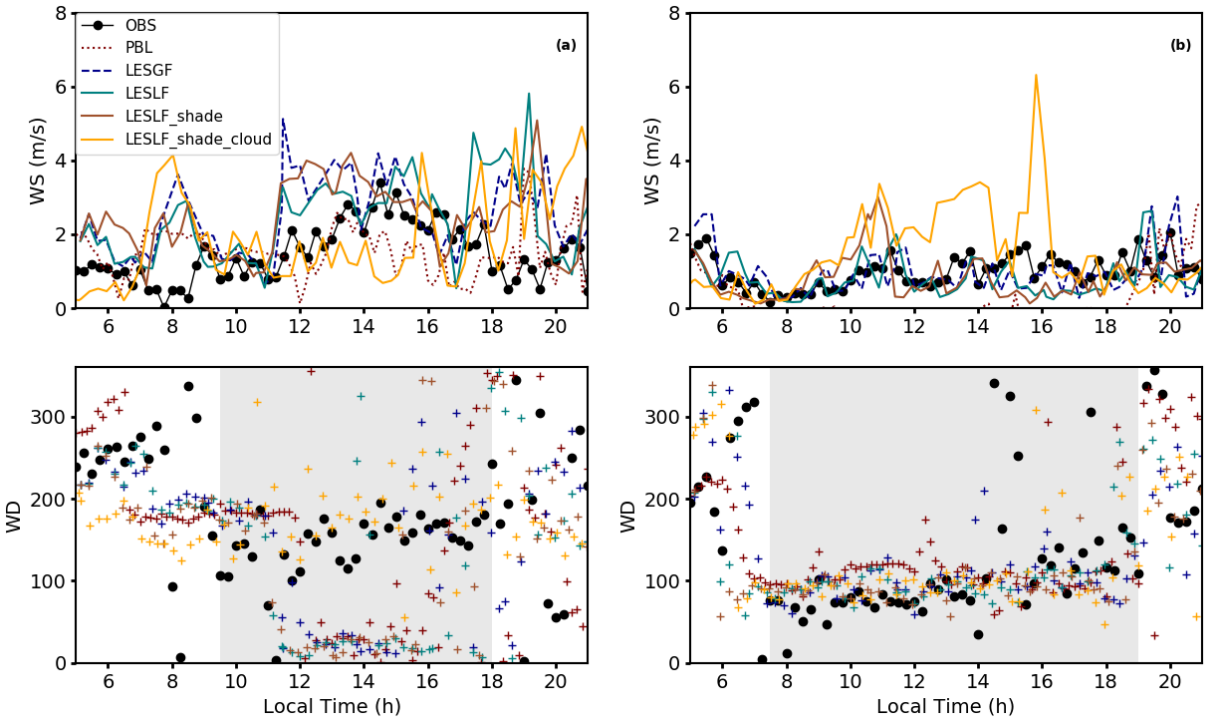

Figure 2.9: Surface wind speed and direction at the open valley (HAY, a) and ridge top (FIS, b) stations located at MCRB. The shaded areas highlight the periods in which the flow was up-valley at HAY, and upslope at FIS.

hours during model spin up, and stayed within the upslope range ($\approx$ 100 - 200°) after the morning transition. LESLF_shade_cloud presented the lowest RMSE ($RMSE$ = 0.9 m/s) for wind speed and ($RMSE$ = 54.5°) direction, and showed less fluctuations in the afternoon predictions of wind direction compared to the other simulations. The frequency of fluctuating wind direction could be due to convective patterns related to surface fluxes and radiative transfer (i.e. cloud shading) in each of the simulations.

At the open valley site (HAY), simulations predicted the onset of up-valley wind and transition from down-valley ($\approx$ 250 - 320°) to up-valley ($\approx$ 100 - 200°) relatively close to observations (Figure 2.9). Observed wind direction showed that wind was up-valley in the afternoon before transitioning back to down-valley after 6 pm, while all simulations except

LESLF_shade_cloud continued to predict a down-valley flow into the afternoon hours. Since this site was not shaded by the surrounding mountains during mid-day hours, the better agreement between LESLF_shade_cloud and observations seems to be related to better predictions of net radiation at this location (Figure 2.5).

Higher elevation ridge tops are generally exposed to solar radiation earlier than valley bottoms, and upslope flows are expected to form before up-valley flows (Lehner & Rotach, 2018; Serafin *et al.*, 2018). The timing of the onset of upslope flow toward west over the open ridge top (FIS) agreed with an earlier formation of upslope wind ($\approx$ 7 am) compared to the onset of the up-valley flow ($\approx$ 9 am) at the HAY station. This was similarly observed at the BNS valley station when the up-valley flow developed with a delay compared to the upslope flow at the POW station. The drainage flow at FIS is complex, with winds flowing mainly toward the east,but sometimes toward the south, influenced by the higher elevations and mountain peaks to the west and north. LESLF_shade_cloud showed the lowest RMSE in wind direction ($RMSE = 77°$) at the FIS station. LES results overestimated wind speed at the HAY station, and PBL had the lowest RMSE at this location ($RMSE = 0.9$ m/s). All simulations presented good agreement with the observed wind speed at the FIS station, except LESLF_shade_cloud that overestimated wind speed at some instances.

Air Temperature

The surface evolution of 2 m air temperature at the four sites (BNS, POW, HAY, and FIS) is shown in Figure 2.10. The simulations overestimated temperature in the morning at the valley sites (HAY and BNS) with biases of 6° and 4° C, respectively, right after sunrise. The overestimation of morning temperature is related to the model's under-representation of cold-air pools in mountain valleys (e.g. Zhang *et al.*, 2013; Pages *et al.*, 2017), and over prediction of radiative fluxes (Figure 2.5). Vionnet *et al.* (2015) reported the impact of valley cold-air pools on temperature biases during wintertime at valley and high-altitude stations in the Canadian Rockies using the GEM meteorological model. Their findings showed that the diurnal cycle at the HAY station was impacted by cold-air pool formation at night and early morning, but cold-air pools did not impact another station, Vista View (VIS), in MCRB located on a valley side at mid-elevations. Similar to Vionnet *et al.*

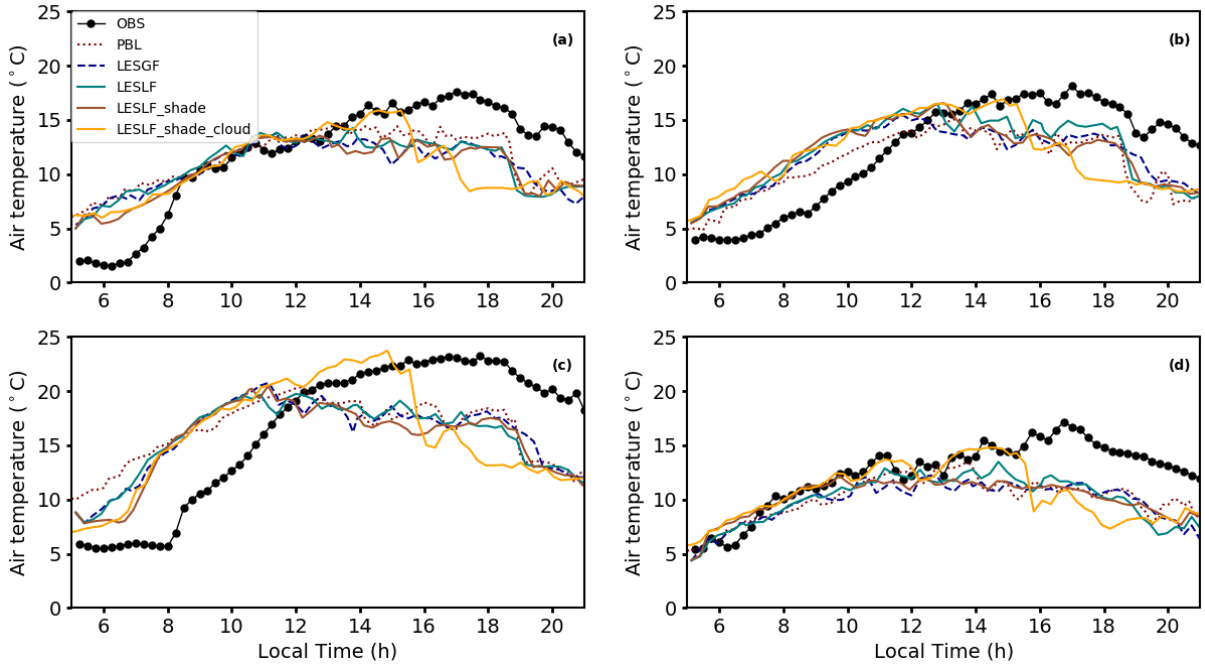

Figure 2.10: 2-m air temperature at the sheltered valley (BNS, a), sheltered ridge top (POW, b), open valley (HAY, c), and open ridge top (FIS, d).

(2015), this study finds that the warm bias was lower at higher elevations (BNS, POW and FIS) at 8 am with biases less than 2° C, with the POW warm bias persisting longer in the morning compared to all other locations, likely related to topographic shading similar to the lag in sunrise at this location.

As the valley nocturnal temperature inversion broke up with daytime heating, warm biases were reduced with very close performance for simulations but better predictions from LESLF_shade_cloud. When BNS and HAY observed temperature evolution an hour after sunrise (9 am LT) are compared, the removal of cold-air pool due to daytime heating happened slightly earlier in the FMRB valley than in the valley of MCRB, although the narrower FMRB valley is sheltered more by the surrounding topography (Figure 2.1c). The persistence of cold-air pools in HAY located in the deep and wide Kananaskis Valley (Figure 2.1b) can be related to a deeper inversion layer, and it will be discussed further in section 3.3. Continuing into the afternoon, all simulations showed a cold bias at all four

locations, regardless of differences in elevation or net radiation biases (Figure 2.5). Model resolution does not seem to have an impact on predictions, and both LES results and PBL showed similar performance for the later afternoon temperature predictions. The rise in maximum observed daytime air temperature of the two sheltered sites, POW and BNS, with smaller elevation differences ($\approx$ 40 m) followed a closer diurnal trend, than HAY and FIS with greater altitude ($\approx$ 900 m) differences.

2.3.2 Bias and Error Analysis

Table 4 summarizes the bias and RMSE error statistics at all stations for surface wind speed, and wind direction in FMRB and MCRB. Biases are calculated using,

$$bias = \frac{1}{N}\sum_{i=1}^{N}(A_i - B_i) \tag{2.2}$$

where A_i is simulation and B_i is observed data, and N is the time step. Overall, wind speed bias between simulated data and observations for all stations at both sites in this study was lowest for LESLF without shading, but RMSE error was slightly lower for PBL. Taking both bias and RMSE error for wind direction into account, LESLF_shade_cloud performed better than the rest of the simulations. If only FMRB sites are considered, LESLF_shade presented the lowest RMSE for wind speed between all the simulations tested, and LESLF_shade_cloud and LESLF presented close proximity errors for wind direction.

Table 5 summarizes the bias and RMSE error statistics at all stations for surface air temperature and specific humidity in FMRB and MCRB. LESLF_shade showed the least agreement with observations for RMSE error in air temperature between the tested simulations, and LESLF_shade_cloud provided lowest RMSE error for surface specific humidity. If RMSE errors and biases for all surface parameters at all station are taken into account, and SODAR evaluations are considered, LESLF_shade_cloud is eventually chosen as the winning model.

Table 2.4: Bias and root-mean-square errors for wind speed (m/s), and wind direction (°) for simulations compared with observations at all meteorological stations in both FMRB and MCRB sites (see Table 1) for the simulations tested. For comparison site specific statistics at only FMRB and MCRB stations are also reported.

MODEL	Met Station	WS Bias	WD Bias	WS RMSE	WD RMSE
LESLF_shade_cloud	All	0.7	5.7	1.6	72
LESLF_shade_cloud	Fortress Mountain	1.2	6.3	1.9	72.5
LESLF_shade_cloud	Marmot Creek	-0.1	-3.7	1.3	73.8
LESLF_shade	All	0.2	-4.6	1.4	74
LESLF_shade	Fortress Mountain	-0.3	-26	1.1	75
LESLF_shade	Marmot Creek	0.4	2.8	1.7	74.6
LESLF	All	0.1	-10.8	1.3	72
LESLF	Fortress Mountain	0.3	-10.3	1.5	72.6
LESLF	Marmot Creek	-0.3	-23.3	1.1	72.8
LESGF	All	0.4	-3.7	1.3	77
LESGF	Fortress Mountain	0.6	5	1.6	78
LESGF	Marmot Creek	0.0	-26.3	1.0	78
PBL	All	-0.5	-2.8	1.2	75.5
PBL	Fortress Mountain	-0.3	-6.9	1.2	76.7
PBL	Marmot Creek	-0.9	-10.0	1.3	73.6

Table 2.5: Bias and root-mean-square errors for air temperature (K), and specific humidity (g/kg) for simulations compared with observations in FMRB and MCRB sites. For comparison site specific statistics at only FMRB and MCRB stations are also reported.

MODEL	Met Station	T Bias	q Bias	T RMSE	q RMSE
LESLF_shade_cloud	All	-0.6	2.6	4.3	3.5
LESLF_shade_cloud	Fortress Mountain	-0.4	2.4	4.9	3.8
LESLF_shade_cloud	Marmot Creek	-0.8	2.6	3.9	2.8
LESLF_shade	All	-0.8	3.4	4.6	4.4
LESLF_shade	Fortress Mountain	-1.2	3.9	4.0	4.3
LESLF_shade	Marmot Creek	-0.4	3.0	5.2	4.5
LESLF	All	-0.6	3.5	4.2	4.6
LESLF	Fortress Mountain	-0.2	3.2	4.8	4.7
LESLF	Marmot Creek	-1.1	3.9	3.6	4.3
LESGF	All	-0.9	3.4	4.4	4.4
LESGF	Fortress Mountain	-0.5	3.0	4.9	4.6
LESGF	Marmot Creek	-1.4	3.7	3.8	4.1
PBL	All	-0.9	3.5	4.1	4.4
PBL	Fortress Mountain	-0.5	3.1	4.6	4.1
PBL	Marmot Creek	-1.1	4.0	3.5	4.9

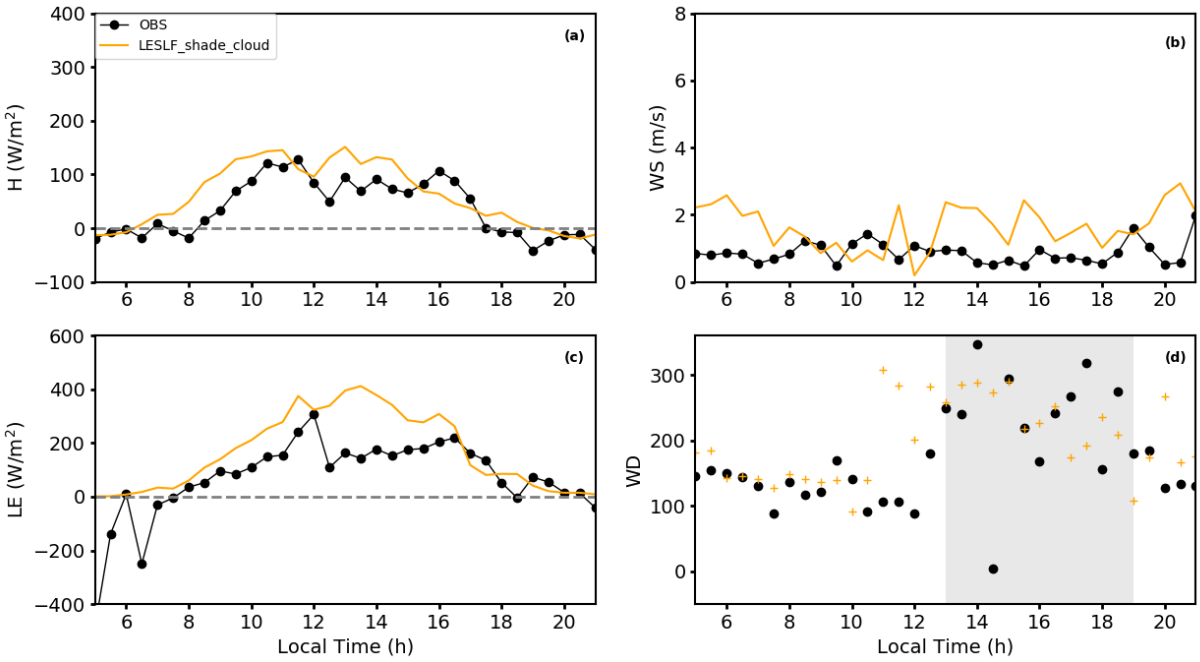

Figure 2.11: Surface sensible heat and latent heat fluxes (a, c), wind speed (b), and wind direction (d) at the north-west-facing slope station (TRI). The shaded area highlights the flow when it was up-valley.

2.3.3 Impact of Topography on Near-Surface Boundary Layer Characteristics

When dealing with very complex terrain, such as FMRB and MCRB mountainous areas, the surrounding topography and geometry of the valley can impact near-surface thermal flows particularly in the valleys. Helgason & Pomeroy (2012) discovered frequent wind gusts transported turbulent energy from higher elevation complex terrain surrounding the Kananaskis River Valley to the HAY valley station, which affected the rate of energy transfer at the surface. Large-scale topographical disturbances were found to contribute to turbulent fluxes in the valley area.

To investigate the effect of surrounding topography on local winds, the best performing model, LESLF_shade_cloud predictions were compared against observations at a differ-

ent location in the FMRB valley. The north-west-facing slope station, TRI (Figure 2.1), equipped with eddy covariance measurements, is located ≈ 300 m away from BNS. The TRI station is on a gentle slope near the valley bottom, ≈ 30 m higher in elevation, and is affected by the valley flows. The simulated sensible and latent heat fluxes, and wind speed and direction were compared against observations in Figure 2.11. Model provided reasonable predictions of surface fluxes, but the simulated wind direction had difficulty following observations when the wind switched between up-valley and down-valley in the afternoon hours similar to the BNS station.

Figure 2.12 depicts snap shots of complex flows in the FMRB and MCRB study areas, where the red dots represent the locations of valley stations, BNS in FMRB, and HAY in MCRB. The simulated surface wind at 10 m AGL at the BNS valley station at FMRB revealed the presence of a down-valley flow in the morning and upslope flows toward the higher elevations (Figure 2.12a). At MCRB, the down-valley flow near the HAY station seems to be impacted by the stronger winds blowing from the south end of the valley (Figure 2.12b), and there is presence of upslope flows toward the higher elevations.

At both the mountain valleys, the simulated afternoon up-valley flows are disrupted by the cross-valley winds or short-lived wind gusts, frequently observed at the higher elevations in the study areas, blowing from the mountain ridges toward the lower elevations (Figures 2.12c and 2.12d). This further illustrates the complex interactions of mesoscale and thermally-driven flows within mountain valleys.

The general topography and orientation of FMRB and MCRB could contribute to differences in up-valley wind strength. Valley geometry has an impact on valley wind formation and strength. Ideal simulations by Wagner *et al.* (2015) have shown that up-valley winds are weaker for wider and shallower valleys, while deeper valleys are conducive to a deeper inversion layer and stronger up-valley flows. The Kananaskis Valley at MCRB is wide, runs north-south and connects to a larger valley (Bow Valley), as compared to FMRB area that has a narrower valley with more compact side walls surrounding it and more of a south-west-north-east orientation. The depth differences between a valley bottom and the tallest ridge top with a meteorological station differ substantially, being 1400 m in MCRB and 500 m in FMRB. The breakup of nocturnal inversion, and transition from a down-valley to up-valley flow depends on the warming of convective boundary layer by

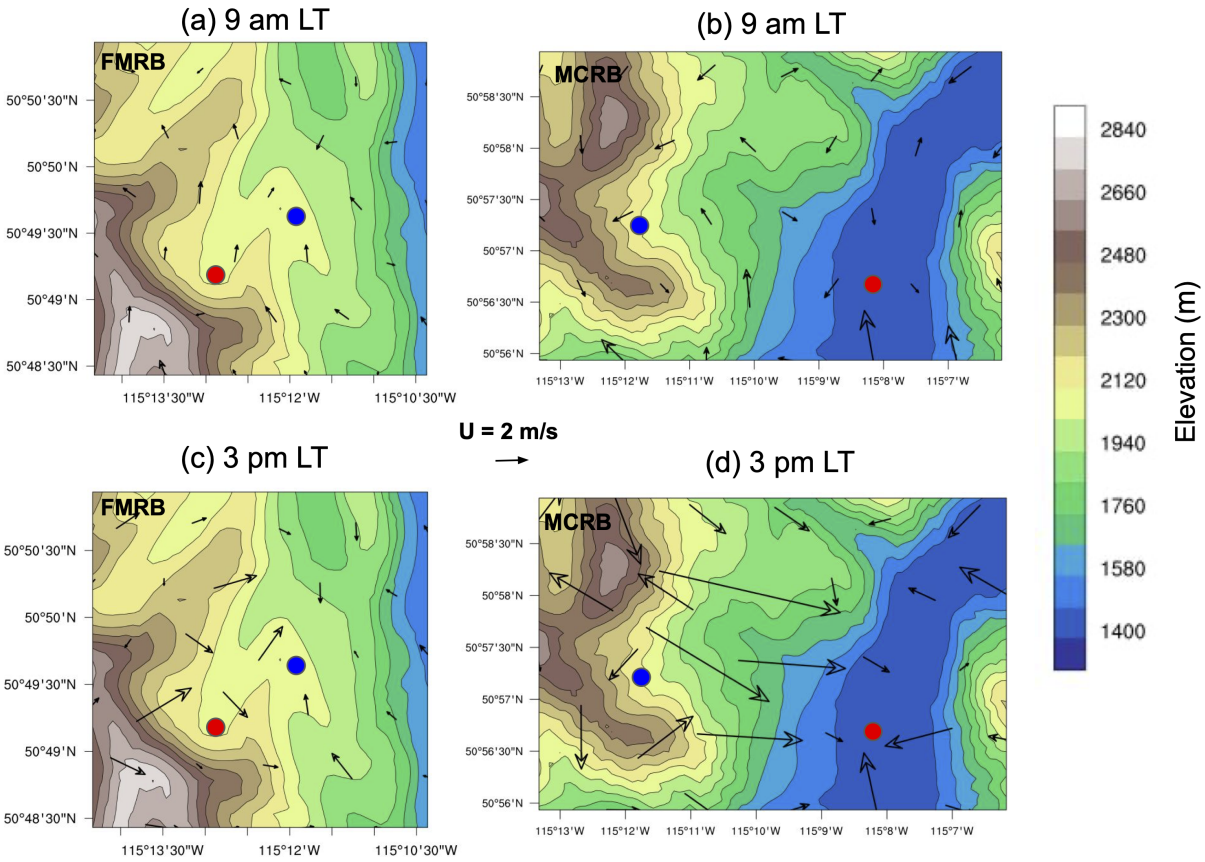

Figure 2.12: Surface horizontal wind vectors (at 10 m AGL) of LESLF_shade_cloud in FMRB at (a) 9 am LT, (c) 3 pm LT, and in MCRB at (b) 9 am LT, and (d) 3 pm LT. The red dots denote the locations of valley stations (BNS, and HAY), and the blue dots are the locations of ridge tops (POW, and FIS) in FMRB and MCRB, respectively. The orography is shown in color, and with isolines every 90 m in the vertical.

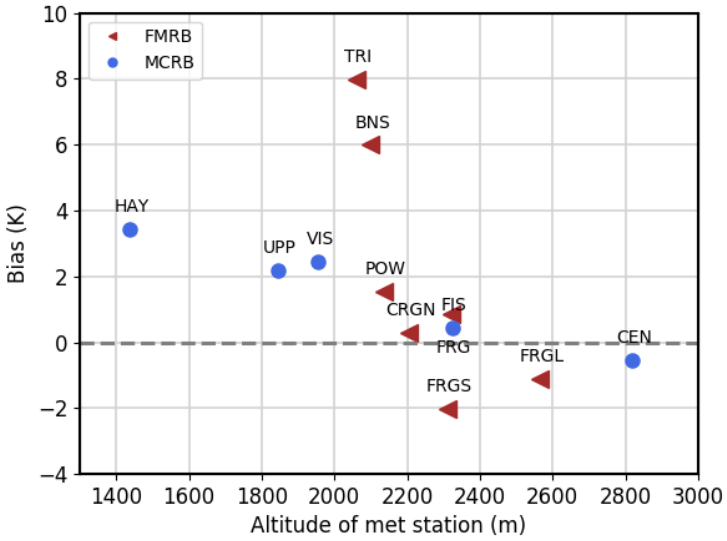

Figure 2.13: Nighttime (6 am LT) 2-m air temperature LESLF_shade_cloud bias for FMRB and MCRB stations.

heated surface layer. The subsidence of warmer air substituting cooler air in the valley compensating for upslope flow is equally important, but the process can be facilitated by valley geometry (Zardi & Whiteman, 2013).

Although HAY is in a wider valley (Figure 2.12), the presence of stronger observed up-valley wind in the afternoon at HAY ($>$ 2 m/s) (Figure 2.9a) in MCRB when compared to BNS in FMRB ($<$ 2 m/s) (Figure 8a), can suggest that valley depth is more important than width in influencing winds in this study. However, it is not possible to make a definite conclusion about the impact of valley geometry since valley orientation and its effect on solar heating of slopes is another important factor in the formation of valley flows.

The overall topography of the terrain seem to influence the performance of the smoothing methods. The simulated wind speed in Figures 2.8 and 2.9 showed differences caused by LESGF and local filtering simulations at the valley locations. The effect of filtering techniques and overall sensitivity simulation seems to be larger at the wider valley (HAY) than the narrower valley (BNS) in the simulations.

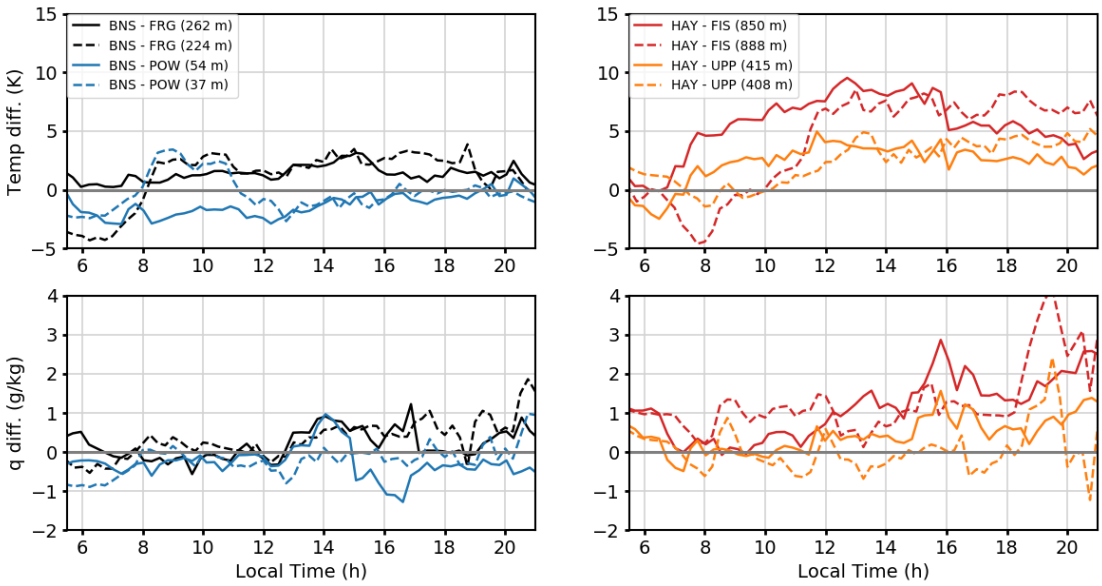

Figure 2.14: 2-m air temperature and specific humidity differences for pairs of valley and ridge top stations in FMRB and MCRB for LESLF_shade_cloud (solid lines) and observations (dashed lines). Model and actual elevation differences for a pair of sites are given for reference.

Topographic differences between FMRB and MCRB can cause differences in model temperature bias. The nighttime warm bias at 6 am for individual stations revealed a correlation between elevation and temperature bias (Figure 2.13). Lower altitude stations below 2200 m AGL in FMRB, and below 2300 m in MCRB showed a warm bias while above 2300 m showed a cold bias. The warm bias rose more rapidly for FMRB at the lower elevations as compared to MCRB. As discussed, cold-air pool seemed to linger longer in the deeper and wider valley at MCRB (Figure 2.10c), but temperatures were lower near the morning at the FMRB valley location (Figure 2.10a), likely due to the narrower valley with more topographic shading. The 6 am air temperature at the lowest valley station in FMRB (TRI) was -2.5° C, while it was 5.6° C at HAY in MCRB. Consequently, nighttime model biases were larger for FMRB valley locations, and rose faster with descend in elevation.

Figure 2.14 illustrates daily differences in the simulated (LESLF_shade_cloud) and the observed absolute magnitude of temperature and specific humidity for a pair of locations,

with different elevations in FMRB and MCRB. The largest differences in nighttime (before 8 am) temperatures between the simulations and observations were for the sites BNS and FRG (valley and ridge top in FMRB) with model and actual elevation differences of 262 m and 224 m, respectively, due to a larger cold-air pool effect, as compared to a pair of valley and ridge top, BNS and POW, which differed less in elevation (54 m and 37 m). Similarly, valley and ridge top (HAY and FIS) in MCRB mountain range displayed larger differences in cold-air pool bias than HAY and mid-altitude ridge top (UPP) with less elevation differences. The bias between simulations and observations diminished faster in FMRB since the observed cold-air pool effect diminished earlier in FMRB (Figure 2.10).

The simulations conducted over both the MCRB and FMRB areas revealed that specific humidity was overestimated during daytime, which peaked in the afternoon with the increase in air instability with a maximum of 6 g/kg and 4 g/kg for MCRB and FMRB stations, respectively. The insensitivity of model predictions to humidity differences in altitude or location of forecast is similar to temperature bias, and could be related to the model's inability to properly simulate horizontal mixing of air temperature and moisture in steep terrain (Zangl, 2002).

The magnitude of humidity bias was found to be correlated with elevation, with the model's overestimations of moisture tending to increase with height, as reported by (Doyle *et al.*, 2013). This is due to systematic errors arising for variables that have strong vertical stratifications such as moisture and temperature. This is a diffusion or advective issue in the model, which makes the valleys drier, and mountains more moist than reality, and since the mixing ratio decreases rapidly with height. Moreover, the simulated and observed differences in humidity after sunrise were more pronounced in MCRB than in FMRB for a pair of sites, likely due to lager elevation differences between the MCRB sites. This indicates that the model has more difficulty predicting moisture on ridge tops than in valleys, particularly in a deeper and wider mountain valley.

2.4 Summary and Conclusions

In this paper, the performance of high-resolution LES to resolve thermally-driven flows, and near-surface boundary layer characteristics of mountainous terrain in Canadian Rockies with two different methods of global and local terrain smoothing were examined. Simulations were performed for two summer days due to computational costs, with different synoptic conditions, for which rare sounding profiles were available. Predictions were also evaluated using data from automatic stations, located at a variety of elevations for valleys and ridge tops in two mountain basins with different valley sizes and volumes. Forecasts were provided for 18 July, 2016, at 90 m horizontal resolution for LES results and were compared against a mesoscale model at 180 m grid spacing.

Evaluations of vertical profiles of wind speed and direction using SODAR measurements demonstrate improved predictions for wind direction by the LES, which utilized local filtering smoothing, topographic shading, and cumulus parametrization activated only for the parent domain to avoid the gray zone (LESLF_shade_cloud). Time series evolution of wind speed at 40 m AGL shows better agreement with the observed afternoon rise in turbulent fluctuations for LES versus mesoscale, while time series of wind direction presents the lowest RMSE for LESLF_shade_cloud, and the highest RMSE for LESGF compared to all the local filtering simulations. Overall, daily evolution and error statistics at valley and ridge top locations for surface wind, air temperature, and humidity show similar performance for all the LES and mesoscale simulations. However, the local filtering simulation, LESLF_shade_cloud, with the cumulus parametrization activated only for the parent domain provides better predictions for surface wind direction, improved predictions for net radiation, and better RMSE for humidity. Hence, LESLF_shade_cloud is a preferable model compared to the other tested simulations to study the boundary layer processes in this study.

LES wind forecasts are consistent with the findings of other mountain studies (e.g. Liu *et al.*, 2020; Umek *et al.*, 2021; Goger *et al.*, 2022). But this assessment also highlights that correct topographic representation, and radiation in very complex terrain has a crucial role in model predictions. For better evaluation of various smoothing methodologies, higher resolution simulations and other methods dealing with terrain following coordinates with

more refined vertical grid nesting should be considered for future work.

Flow reversals, topographic and mesoscale winds can all have important influences on thermally-driven wind flows in complex terrain. The simulated wind direction had difficulty following observations in the valley locations, and the wind switched between up-valley and down-valley in some instances in the afternoon hours. In this study, both cloud shading and wind gusts seem to contribute to short-lived flow reversals at the valley locations.

Larger errors in nighttime and early morning air temperatures reveal that the simulations in this study underestimated cold-air pool effects, and underpredicted air temperature during the warmer convective hours in mid-day. Possible reasons for this discrepancy is faster cooling by clouds in the model compared to reality, and topographic shading not accounted by the model. Interestingly, nighttime cold-air pool bias decreased toward the higher elevations, indicating an elevation dependency of the value of nightitme cold bias. Specifically, the nighttime cold bias became greater toward the lower elevations for both mountain basins in the study. The elevation dependency was more pronounced for FMRB, which has a narrower valley area, than for MCRB. This difference could be due to a larger drop in observed nighttime temperatures in the narrower valley of FMRB with more topographic shading. In contrast, the removal of cold-air pool due to temperature rise happened earlier in the valley in FMRB than in the valley of MCRB due to a deeper inversion layer of the deeper valley. Moreover, the up-valley flows were stronger in the wide but deeper Kananaskis Valley in MCRB, as compared to the narrower and shallower valley in FMRB. In this study, the larger valley volume has an impact on up-valley wind strength. The formation and transition of down-valley to up-valley occurred earlier in MCRB valley than in FMRB valley. This is a complex process in a complex terrain, and could be related to a combination of various factors such as the thermodynamics related to valley geometry and orientation, contribution from upslope flows, and the rate at which cold air drains down the valley, which helps with the formation of up-valley flows.

This study also illustrates the shortcomings in model predictions of LES for daytime thermally-driven wind flow in alpine terrain, and demonstrates the improvement of high-resolution LES with correct cloud shading in predictions of diurnal radiative fluxes and wind flow patterns. Improvement in high-resolution numerical modeling of diurnal wind flows and radiation in complex terrain is essential in calculation of water vapour and heat

fluxes and exchange processes in surface-atmosphere interactions in mountain terrain. The improvement in representation of topography and land cover combined with multiscale simulations at high-resolution can help broaden our scope of weather forecasting and predictions of boundary layer processes in mountain basins.

Chapter 3

Analysis of Turbulence and Turbulent Kinetic Energy Dynamics in Complex Terrain

3.1 Introduction

In mountainous terrain where exchange processes between the atmospheric boundary layer (ABL) and the surface are highly impacted by the complexity of the terrain, correctly representing boundary layer turbulence is important for estimating land-atmosphere exchanges of momentum, evaporation and sensible heat transfer etc. (Rotach & Zardi, 2007). The characteristics of turbulence, represented as turbulence kinetic energy (TKE), within the ABL over a complex terrain are strongly influenced by the level of heterogeneity of terrain, diversity in surface cover and vegetation type, and meso- and microscale wind flows (e.g. Rotach & Zardi, 2007; Dewekker & Kossmann, 2015; Lehner & Rotach, 2018; Solanki *et al.*, 2019). TKE is related to the exchange of heat, moisture and momentum throughout the ABL, and TKE budget terms describe the contribution of physical processes to production, dissipation, and redistribution of turbulence.

While buoyancy-driven production is the primary mechanism in transferring the fluxes

to the atmosphere in a sunny day over a flat terrain, with contributions from shear production on windy days, additional processes influence exchange on spatial or temporal scales in mountainous areas (Lehner & Rotach, 2018). Horizontal and vertical wind effects significantly impact turbulent production and the horizontal and vertical exchange of mass, moisture, and momentum in complex terrains. For instance, interactions between up-valley winds and winds aloft (e.g. cross ridge flows) generate both vertical and horizontal wind gradients, leading to strong afternoon shear production, and contributing to TKE at the surface (Weigel & Rotach, 2004; Weigel *et al.*, 2007).

Under weak synoptic conditions, thermally induced circulations prevail due to the horizontal temperature differences over complex terrain (Lehner & Rotach, 2018; Serafin *et al.*, 2018). The slope and valley flows contribute to TKE production via coupling between vertical wind shear and the momentum flux (Zardi & Whiteman, 2013). However, slope and valley flows are often disrupted by large-scale synoptic or mesoscale winds and their interactions with mountain topography, which in turn contribute to turbulent production and its transport within mountain valleys (e.g. Rotach & Zardi, 2007; Helgason & Pomeroy, 2012; Singh *et al.*, 2016; Goger *et al.*, 2022). Vecenaj *et al.*, (2011) studied mountain-wave-induced turbulence during a mountain wave event in Owens Valley, California, and discovered higher TKE on the sloping western part of the valley when compared to with the valley center. They found that advection of TKE by the mountain-wave activity played an important role in TKE production over the western slope.

Most numerical weather prediction (NWP) models use a one-dimensional (1D) turbulence parametrization considering only vertical turbulent exchange. However, contributions from non-local sources to the TKE budget during dynamically driven wind flows, such as mountain wave events, indicate the importance of horizontal budget terms in production or redistribution of TKE over mountainous terrain (Vecenaj *et al.*, 2011; Munoz-Esparza *et al.*, 2015; Barman *et al.*, 2019). In a case study between flat (Scaled Wind Farm Technology, west Texas), and complex (Columbia Basin Wind Energy Study, northeastern Oregon) terrains, Rai *et al.*, (2017) showed that the horizontal shear had a significant contribution to the TKE budget, and the 3D nature of the TKE budget should not be ignored over complex terrain. Goger *et al.*, (2018) also studied the impact of 3D effects on TKE in the Inn Valley, Austria, by including horizontal shear production and advection in the

modelled TKE budget, which resulted in more realistic predictions for TKE budget terms especially during shear production dominant hours in the afternoon and at night. Correct parametrization of boundary layer turbulence, as represented by TKE, is important in high resolution simulations in a complex terrain, as the turbulent state is used to provide input for other applications such as wind energy, hydrological calculations, or understanding and predicting sensible heat and evaporative exchange processes that govern evapotranspiration. However, the degree to which the spatial and temporal variability in wind effects can contribute to turbulent production in complex terrains is still an open question.

The objective of this study is to explore and quantify the variability of TKE and the TKE budget terms with elevation and topography in a shallow high mountain valley in Fortress Mountain Research Basin, Alberta. Observations were chosen from a fair-weather sunny day and in presence of a weak afternoon synoptic wind, which does not overwhelm thermally driven valley and slope flows, but can contribute to turbulence in the valley area. The results from high resolution (90 m) Large-Eddy Simulations (LES) with the Weather Research and Forecasting (WRF) model are compared against observations of TKE for a location within the valley, and two ridgetop locations on either side of the Fortress Valley. Contributions from simulated vertical and horizontal TKE budget terms were investigated to examine the effect of cross-ridge wind on overall TKE and note implications for turbulent transfer of scalar fluxes.

3.2 Study Site

The study was conducted at a southwest-northeast oriented shallow valley in the eastern slopes of the Canadian Rockies, Kananaskis Valley, Alberta (Figure 3.1). Fortress Mountain Valley is surrounded by three sides: a steep mountain peak at an elevation of $\sim$ 2800 m above sea level (asl), to the southwest, Fortress ridge to the northwest at an elevation of 2300 m asl, and Canadian ridge to the southeast at an elevation of 2000 m asl. The northeast end of valley is open and connects to a wider north-south valley at an elevation of 1600 m asl. The vegetation cover is complex and typical of high mountains with a variety of shrubs and needleleaf forest in the valley and on its sides, transitioning to

grass and bare rock faces at higher elevations. Thermally driven flows are present during the summer months, often disrupted by the stronger wind gusts and mesoscale flows and changes in radiation caused by the cloudy skies. For this study, a fully sunny day is chosen to minimize the disruptions from cloud cover on the slope and valley flows.

3.3 Materials and Methods

3.3.1 Observations

A sunny, fair-weather day (i.e., weak synoptic wind < 5 ms^{-1} at the height of 800 hPa) on 19 August, 2016, was used for this study as it was expected to allow for development of thermally driven flows. Data was collected from three eddy-covariance measurement systems at the base of the northwest-facing slope ($\sim 15°$) (TRI) in the north-east opening of Fortress Valley, and at the southern and northern ridgetops (FOR and FRG, respectively) (Figure 3.1). Each station was equipped with a CSAT3 ultrasonic anemometer (Campbell Scientific, USA) at 2 m agl at TRI and FRG, and 15 m agl at FOR locations. The data sampling frequency was set to 20 Hz for the turbulence measurements, and the raw data was processed using the software, EddyPro (LiCOR, Lincoln, USA), provided by Campbell Scientific (Campbell Scientific Inc., Logan, UT, USA).

A correct determination of near-surface fluxes are necessary for a proper estimation of turbulent properties. This is performed by finding the most suitable averaging period that represents the desired turbulent scales. The averaging time over a complex terrain has to be determined carefully, since short averaging periods may not capture flux contributions from larger eddies and include non-stationarity effects, while long periods may include mesoscale motions in calculation of fluxes (Mahrt & Vickers, 2006). To find the most appropriate averaging period, analyses of 'Ogive' plots of turbulent fluxes were performed (e.g. Oncley *et al.*, 1996; Lee *et al.*, 2004). If an ogive converges starting from a certain frequency, this is an indication that there is no more flux beyond this frequency. This frequency or the equivalent period can be taken as the averaging period for the determination of turbulent perturbations.

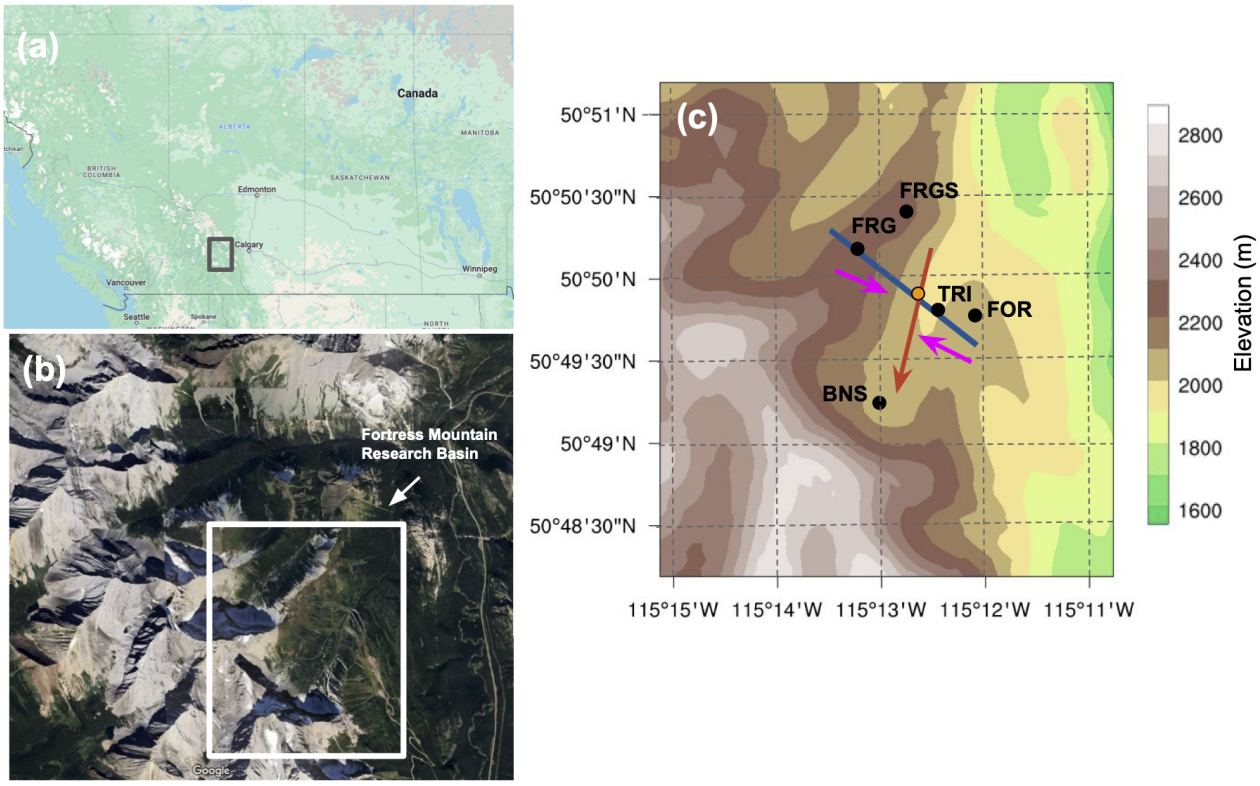

Figure 3.1: (a) and (b) Location of Fortress Mountain Research Basin. (c) Locations of three eddy covariance systems Tripod (TRI), Forest ridge (FOR), and Fortress ridge (FRG), as well as meteorological stations Bonsai (BNS), and Fortress ridge south (FRGS) marked with black dots, with model topography (derived from the USGS dataset at 90-m resolution; isolines every 100 m in the vertical) of the Fortress Mountain Research Basin. The red arrow shows the direction of up-valley flow, and the pink arrows show the directions of cross-ridge flows blowing from southeast in the morning and from northwest in the mid-afternoon. The blue line denotes the cross-section in Figure 3.4. The orange dot denotes a location on the opposite slope to TRI impacted by the up-valley flow.

Using the Ogive function for 1 hour periods between 1 pm and 6 pm when the mesoscale wind was the most prominent, the co-spectra of $u'w'$ and $v'w'$ converged to a 30-min averaging period, and was taken for determination of turbulent perturbations. 30-min averaging has been suggested by other studies in mountainous terrain (e.g. Helgason & Pomeroy, 2012; Babic & Rotach, 2018; Barman *et al.*, 2019; Solanki *et al.*, 2019), and seems to capture the majority of turbulence contributions to the fluxes while removing most of the mesoscale effects.

The raw data from the sonic anemometer was first despiked using the routine of Vixkers & Mahrt (1997). After the data was detrended and block averaged to the averaging period, the turbulence data were rotated into a streamline coordinate system after applying a double rotation scheme (Kaimal & Finnigan, 1994). Finally, the turbulence characteristics were quality checked using EddyPro to satisfy the stationary test given by Foken & Wichura (1996) as its standard 30% level. The stationary test looks for variability of statistics with time due to the fluctuation of meteorological parameters and mesoscale events, and is performed using the mean flux values over each 30-min interval with the mean values over the six corresponding 5-min sub-intervals. After this calculation, the dataset, which passed this quality check, was used for further analysis.

3.3.2 Numerical set-up

The Weather Research and Forecasting (WRF version 3.7.1) model (Skamarock *et al.*, 2008) was used to simulate the flow and turbulence structure in Fortress valley. The model was set up into four nested domains: The outer domain of 8.1 km (D1) horizontal spacing spanned western Canada and northwestern USA, and was driven by Medium-Range Weather Forecasts Reanalysis (ERA-interim) data (Dee *et al.*, 2011). The parent domain was nested down to fine resolution grids D2-D4 (2.7 km, 0.9 km, and 90 m), aiming to resolve the complex topography of Canadian Rockies using LES (Figure 3.2). The LES domain consisted of 401 $\times$ 401 grid points with a time step of 0.02 s. A grid refinement ratio of 10 was adjusted from D3 to D4 (Zhou & Chow, 2014) to avoid the gray zone associated with eddies at scales of a few hundred meters at mesoscale down to three-dimensional LES (Wyngaard, 2004; Munoz-Esparza *et al.*, 2017). The large changes in resolution from D3 to

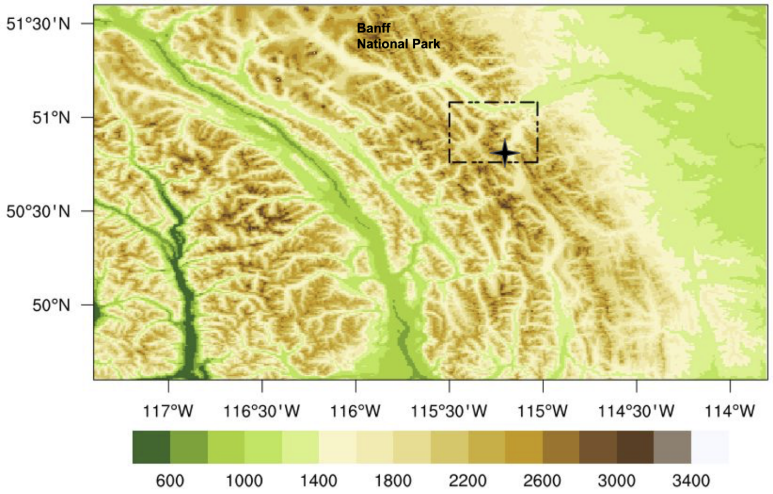

Figure 3.2: Contours of terrain height in meters above mean sea level (amsl) of the two innermost domains. The outer domain (D03), centered on the Canadian Rockies, has 0.9 km horizontal resolution. The dashed line outlines the extent of the LES domain (D04), which has 90 m horizontal resolution. The black star marks the location of the area of interest.

D4 can be accommodated by almost doubling the number of grid points in the horizontal direction, coupled with the cell perturbation method for some computational saving (Chow *et al.*, 2019). Vertical grids were distributed between ground level and 20 km (10 hPa) for a total of 80 levels stretched progressively from bottom to top of the model with a stretch coefficient of about 1.23 between the top levels. The lowest model level located at $\Delta z = 20$ m and 28 vertical levels lie below 1000 m.

Mesoscale domains (D1, D2, and D3) used the YSU planetary boundary layer (PBL) scheme (Yonesi University) (Hong *et al.*, 2006) for vertical diffusion, and the 90-m resolution LES domain (D4) made use of full three-dimensional local 1.5-order prognostic TKE diffusion closure (Lilly, 1966; Lilly, 1967). For cumulus parameterization, Kain-Fritsch (new Eta) (Kain, 2004) was used for the coarser domains, excluding the LES domain. Shortwave radiation was parametrized using the Dudhia scheme (Dudhia, 1989), which includes slope and shadowing effects on surface shortwave fluxes if corresponding namelist variables are activated. Longwave radiation was quantified using the rapid radiative transfer model (RRTM) (Mlawer *et al.*, 1997). The ERA-Interim was used to initiate soil moisture and temperature at 4 soil model levels at ground level and 10, 30 and 100 cm below ground level.

The simulations for parent domains were initialized at 0600 UTC to account for a 6-hour spinup period, while the 90-m resolution LES domain was initialized from the output of the 0.9 km resolution domain at 1200 UTC to run concurrently after the spinup period. Full details on simulation set-up, initialization and boundary conditions, and experimental design can be found in (Rohanizadegan *et al.*, 2023). The model set-up used for this analysis is equivalent to the so-called "LESLF_shade_cloud" setup (local filtering LES with topographic shading and slope effects on radiation, and with cloud parametrization only applied to the coarser parent domain) described by (Rohanizadegan *et al.*, 2023).

3.3.3 TKE Calculations

The model and observed resolved TKE, e, were calculated as the sum of velocity variances, $e = \frac{1}{2}(u'^2 + v'^2 + w'^2)$, where u', v', and w' were obtained by subtracting 10-min moving averages from the instantaneous wind speed components ($i = 1, 2, 3$), defined as $u_i' = u_i - \overline{u_i}$.

The total simulated TKE was calculated by the sum of the resolved e and subgrid-scale TKE provided by the WRF output . The TKE budget equation is expressed as (Stull, 1988),

$$\underbrace{\frac{\partial \overline{e}}{\partial t}}_{(I)} + \underbrace{\overline{U_j}\frac{\partial \overline{e}}{\partial x_j}}_{(II)} = \delta_{i3}\underbrace{\frac{g}{\theta_v}(\overline{u_i'\theta_v'})}_{(III)} - \underbrace{\overline{u_i'u_j'}\frac{\partial \overline{U_i}}{\partial x_j}}_{(IV)} - \underbrace{\frac{\partial(\overline{u_j'e})}{\partial x_j}}_{(V)} - \underbrace{\frac{1}{\rho}\frac{\partial(\overline{u_i'p'})}{\partial x_i}}_{(VI)} - \underbrace{\epsilon}_{(VII)}, \tag{3.1}$$

where letters with overbars denote mean quantities; U is the mean wind speed, g is the acceleration due to gravity, θ_v is the virtual potential temperature, ρ is the density of air, ϵ is the TKE dissipation rate, and p is the atmospheric pressure. Term I represents the time tendency of TKE, (II) is the advection of mean TKE by the mean wind, (III) represents the buoyant production/consumption of TKE, depending on the sign of the heat flux $\overline{u_i'\theta_v'}$, (IV) represents the mechanical shear production, (V) is the turbulent transport of TKE, representing the redistribution of TKE by vertical or horizontal velocity fluctuations, (VI) is the pressure transport term, and the last term is the viscous dissipation of TKE. Turbulent dissipation was calculated using the method of -5/3 slope to detect the inertial subrange (Piper & Lundquist, 2004) from the power spectra of the two horizontal wind components. The extend to which the TKE balance is closed can provide some indication of the contributions from horizontal terms and pressure redistribution.

Since only one level of observations were available at all the stations, the observed and simulated buoyancy production/consumption, vertical shear production, vertical advection and turbulent transport terms at the TRI and FRG stations (2 m above ground) were calculated from the first model level for comparison, assuming zero values for the budget terms at the surface. At the FOR station, model output from two first levels were used to compare with the observations at 15 m above ground. The vertical profiles of the TKE budget terms were calculated using two adjacent model levels starting from the first model half-level at 10 m above ground.

The horizontal shear production at the northwest-facing (TRI) and southern ridgetop (FOR) stations were estimated using the simulations from a location along the cross-ridge wind (u), which was found to contribute the most to horizontal shear term at a similar altitude and two grid points apart,

$$\approx \overline{u'u'}\frac{\Delta\overline{U}}{\Delta x} + \overline{u'v'}\frac{\Delta\overline{V}}{\Delta x} \tag{3.2}$$

respectively, where $\overline{U}$ and $\overline{V}$ are the mean horizontal velocity components, and $\Delta x =$ 180 m.

The horizontal shear production at the ridgetop station (FRG) was calculated with the model output from the south-facing slope station (FRGS, Figure 3.1) that is located at a similar altitude,

$$\approx \overline{u'u'}\frac{\Delta\overline{U}}{\Delta x} + \overline{u'v'}\frac{\Delta\overline{U}}{\Delta y} + \overline{u'v'}\frac{\Delta\overline{V}}{\Delta x} + \overline{v'v'}\frac{\Delta\overline{V}}{\Delta y} \tag{3.3}$$

where the velocity variances are taken from the FRG station, the velocity components $\overline{U}$ and $\overline{V}$ are rotated back into the Cartesian coordinate system, and $\Delta x = 400$ m and $\Delta y =$ 100 m. Horizontal advection is not considered in this study since the terrain heterogeneity and vegetation can modify the mean TKE significantly spatially, and in all directions.

3.4 Results and Discussion

3.4.1 Surface Parameters

WRF LES (LESLF_shade_cloud) was able to reproduce the observed transition and turning points for valley and slope flows, and provided realistic estimates of the heat fluxes at the northwest-facing slope (TRI) and at the northern ridgetop (FRG) stations. Figure 3.3 illustrates the good agreement between the measured and simulated sensible heat flux on the simulated day, 19 August, at the TRI (Figure 3.3a), and at the FRG stations (Figure 3.3c). The model overpredicted sensible heat after sunrise until about 3 pm at the southern ridgetop (FOR) (Figure 3.3b). Model overprediction of sensible heat at the FOR station was most likely due to overestimation of radiation in the morning (not shown), and misrepresentation of tall canopy at this location that can have a cooling effect on the sub-canopy soil.

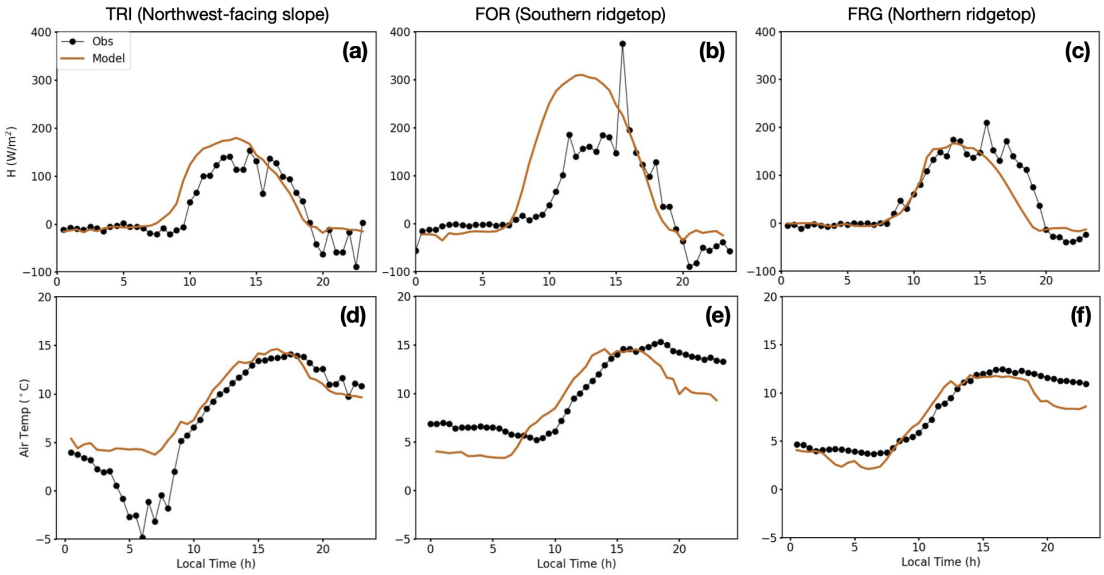

Figure 3.3: Surface sensible heat flux and air temperature at the TRI (a,d), FOR (b,e), and FRG (c,f) stations.

The observed and simulated surface air temperature at the TRI and FRG stations are shown in Figures 3.3d and e, with predictions following the observations, except the period with cold-air pool in the valley at the TRI location, and night time at the FRG station. Similarly, the model underestimated air temperature at the FOR station at night time, and overestimated temperature during midday.

3.4.2 Simulated Flow Patterns

Cross-Sections

Figure 3.4 shows the cross-valley and along-valley flows on a northeast-southwest cross-section (Figure 3.1) on 19 August 2016 at three different times (11 am, 3 pm, and 8 pm LT). In the morning (Figure 3.4a), the isentropes showed steepening on the southeast-facing slope, indicating a growing mixed layer inside the valley, and a stable layer aloft. The elevation difference between the two ridge tops, and the earlier son exposure of the

southeast-facing slope most likely explains the unevenness in the isentropes over the north-facing and south-facing slopes. Upslope flows were established at the southeast-facing slope, and were prominent with speeds > 2 ms^{-1} . A southeast cross-valley wind was present, also observed at the FRG ridgetop station, possibly eroding the weak upslope flow on the northwest-facing slope, and lasted until mid-afternoon.

Several hours later at 3 pm (Figure 3.4b), an along-valley flow has developed above the valley floor, and the center of the flow was inclined toward the southeast-facing valley side wall. The up-valley flow exhibited an asymmetric structure, with higher wind speeds ($>$ 4 ms^{-1}) on the southeast-facing slope compared to the lower wind speeds (< 2 ms^{-1}) on the northwest-facing slope. This difference in wind speeds is likely due to the curvature at the south-eastern part of the valley entrance, pushing the air toward the north side of the valley due its inertia, a feature also reported in other studies (Weigel & Rotach, 2004; Goger *et al.*, 2018) for curved valleys. The asymmetry in along-valley wind speeds can be intensified by the differences in elevation of the valley side walls, with the north side of the valley receiving more radiation than the south side. At this time, the upslope flow at the southeast-facing valley side wall was slightly eroded by a stronger afternoon northwest cross-ridge wind.

By the sunset, simulations indicated the breakdown of the up-valley flow, and a weak downslope flow was established on the southeast-facing slope, indicated by both the wind arrows and the isentropes on the slope. The cross-ridge wind with higher wind speeds (> 4 ms^{-1}) dominated above the valley, while along-valley and slope flows showed much lower wind speeds (1 ms^{-1}).

Vertical Profiles: Northwest-Facing Slope versus Southern Ridgetop

Vertical profiles from model output of the northwest-facing slope station (TRI), and the southern ridge top station (FOR) are presented in Figure 3.5 for 9 am, 3 pm, and 6 pm, to show three key moments in the evolution of flow patterns and TKE. At 9 am at TRI, there was a developing mixed layer close to the surface below 30 m above ground in the potential temperature profile, while above this mixed layer, the atmosphere was stably stratified (Figure 3.5a). The wind displayed a downslope drainage flow from near the

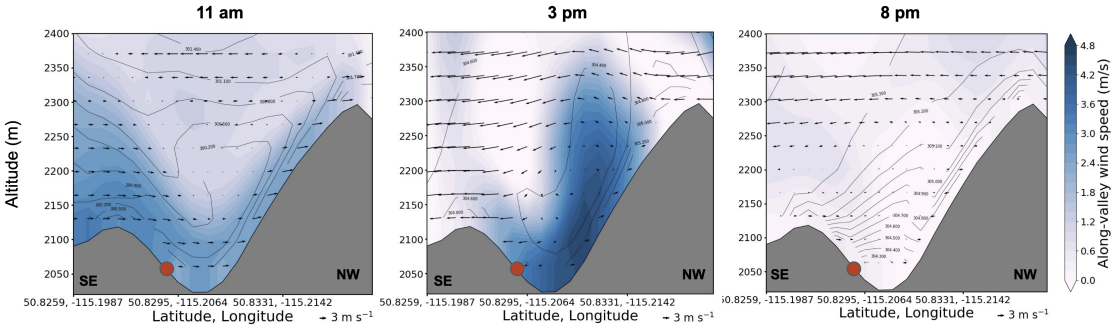

Figure 3.4: Interpolated along-valley wind speed (color contours) on a northwest-southeast cross-section along the red line in Figure 3.1 for 11 am, 3 pm, and 8 pm on 19 August 2016. Wind arrows are calculated from the cross-valley wind speed (u) and the vertical velocity component (w), respectively. Red dot marks the location of the TRI station. "SE" and "NW" indicate southeast and northwest, respectively.

ground to a height of 200 m above ground, reaching a maximum wind speed of ~ 3 ms^{-1} at approximately 50 m above ground (Figure 3.5b, c). The early morning mixed layer showed TKE values ~ 0.1 m^{2}s^{-2} very close to the surface (Figure 3.5d).

In the afternoon, the atmosphere was neutral below 800 m, and stable above. Flow direction above the ground (20 m and above) was influenced by the cross-ridge wind blowing from the northwest (Figure 3.4c), and the wind speed intensified with height above ground with speeds of > 5 ms^{-1} above 500 m above ground. At this time, there was evidence of an up-valley flow at a location opposite side of the TRI station, with the model suggesting a jet-like velocity maximum (up to 4 ms^{-1}) at around 20 m above ground. TKE values were significantly larger than in the morning, showing a peak close to the ground, which rose to a second peak of ~ 4 m^{2}s^{-2} at 500 m above ground. Multiple TKE maxima were also previously reported in the Rivera Valley (Weigel *et al.*, 2007) and in the Inn Valley (Goger *et al.*, 2018). Later in the afternoon, at 6 pm, slope flow retained a similar structure to the early afternoon, transitioning sharply from a weak downslope flow (100 degree) very close to the ground to ~ 270 degee, suggesting an influence by the stronger cross-ridge flow. There were multiple TKE peaks present, with highest TKE at 100 m above ground.

At the southern ridge top (FOR), the model showed a deeper developing mixed layer

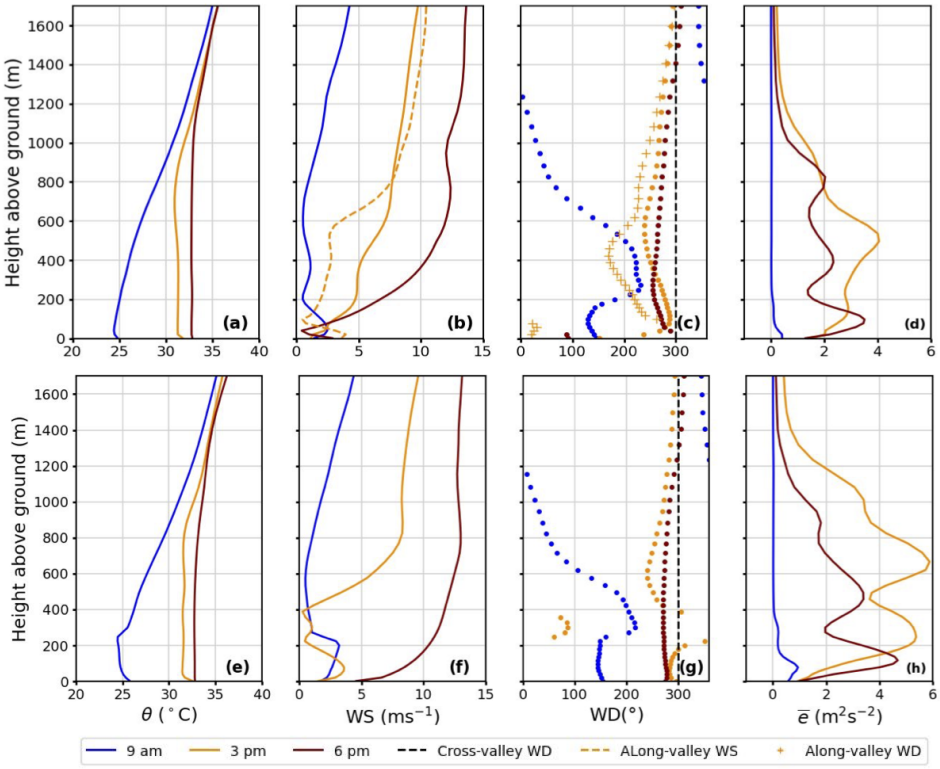

Figure 3.5: Simulated vertical profiles of (a, e) potential temperature, (b, f) horizontal wind speed, $WS = \sqrt{u^2 + v^2}$, (c, g) wind direction, and (d, h) TKE at a grid point closest to the TRI, and FOR stations, respectively, at 9 am, 3 pm, and 6 pm on 19 August, 2016. The black dashed line denotes the direction of mid-afternoon cross-ridge flow. The orange dashed line and the plus signs indicate the wind speed and direction of the along-valley flow, respectively, at a location across the TRI station on the opposite slope, denoted by the orange circle in Figure 3.1.

in the morning when compared to the TRI valley location (Figure 3.5e), reaching approximately 250 m, capped by a weak inversion layer up to 300 m above ground. Ridgetops and slopes are exposed to sunlight earlier than valley floors, and develop a mixed layer earlier than valleys (Zardi & Whiteman, 2013). Wind speed at FOR was higher near the ground compared to TRI (exceeding 2 ms^{-1}), and TKE was slightly larger than at TRI, reaching ~ 1 m^2s^{-2} at about 70 m above ground (Figure 3.5f, h). At 3 pm, the flow showed a jet-like feature near the ground with wind speeds exceeding 3 ms^{-1}. Wind speeds showed a steep rise in the neutral boundary layer between 400 and 800 m above ground. TKE displayed two peaks at about 200 and 600 m above ground, measuring around ~ 5 and 6 m^2s^{-2} at this time. By 6 pm, the ground flow was strong (> 5 ms^{-1}), and wind speed increased progressively up to a height of 600 m above ground, similar to the TRI location, where the cross-ridge flow dominated the atmosphere above the study sites.

3.4.3 Turbulence Characteristics

Time Series: Northwest-Facing Slope Versus Southern Ridgetop

The simulated time series of wind speed and direction, TKE, and the associated vertical budget terms are compared against observations at TRI and FOR in Figure 3.6. Note that observations were recorded at 2 m above ground at TRI and FRG, and at 15 m above ground at FOR, while the lowest model half-level is located at 10 m above ground.

At TRI, the model followed observations for surface wind speed and wind direction reasonably well (Figure 3.6a, b) after a few initial hours of spin up, during which the model adjusted to the observed downslope flow at the station location. After sunrise, both model and observations showed that the wind direction generally remained a weak downslope flow < 2 ms^{-1} for most of the day at the 2 m height. In the month of August, the TRI station received more shading in the morning than the opposite side of the valley. Observed wind revealed a variable direction at TRI, impacted by different flows such as both valley and slope flows, or influenced by non-local flows blowing from the larger valley in the southeast and passing over the Canadian ridge. Although the cross-sections in Figure 3.4 implied a well-developed mid-day up-valley flow in the northern section of the valley,

the persistence of the downslope flow ($\sim$ 100-180°) into the afternoon at the TRI location can be an indication of non-local flows affecting the wind at this location on the day of study.

TKE began to increase with the development of the mixed layer in the valley, even though surface wind speed remained low (Figure 3.6c). But the model predicted higher wind speeds for the cross-valley wind speed component (U) at 20 m and 250 m agl (equivalent to the Fortress ridge elevation), also shown in cross-sections in Figure 3.4. The increase in wind speed at higher elevations above ground seemed to correlate with the increase in TKE at some instances throughout the day. The time series of vertical TKE budget terms at the first model level and at the observed 2-m height (Figure 3.6d, e) show that both the buoyancy and mechanical term can not explain the rise in afternoon TKE production at the surface level.

At FOR, the flow was easterly until sunrise about 7 am (Figure 3.6e), and became southerly afterwards. This change in wind direction was accurately depicted by the model. Wind speeds were initially low in both the model and observations during the first few hours after sunrise while the mixed layer developed above the ridgetop (Figure 3.6d). Overall, the rise in the observed TKE is well simulated by the model, and correlated with the rise in wind speed (Figure 3.6F). Observations showed Buoyancy and vertical shear production as the dominant production terms for TKE, while vertical advection and turbulent transport terms contribute to redistribution of TKE throughout the day. Model underpredicted buoyancy, but agreed with observations on the vertical shear as a production mechanism for TKE at this location. The model underpredicted TKE towards nighttime at this location due to underestimation of vertical shear production term.

Horizontal and Vertical TKE Budget Terms from Simulations

To investigate the contributions from horizontal and vertical TKE budget terms to TKE, vertical profiles of simulated TKE budget production components at TRI, and at FOR are presented in Figure 3.7. Since multiple levels of observations were not available, only model results are shown for the TKE budget analysis. At 9 am in the morning, TKE production at TRI was predominantly determined by horizontal shear the ground, reaching up to

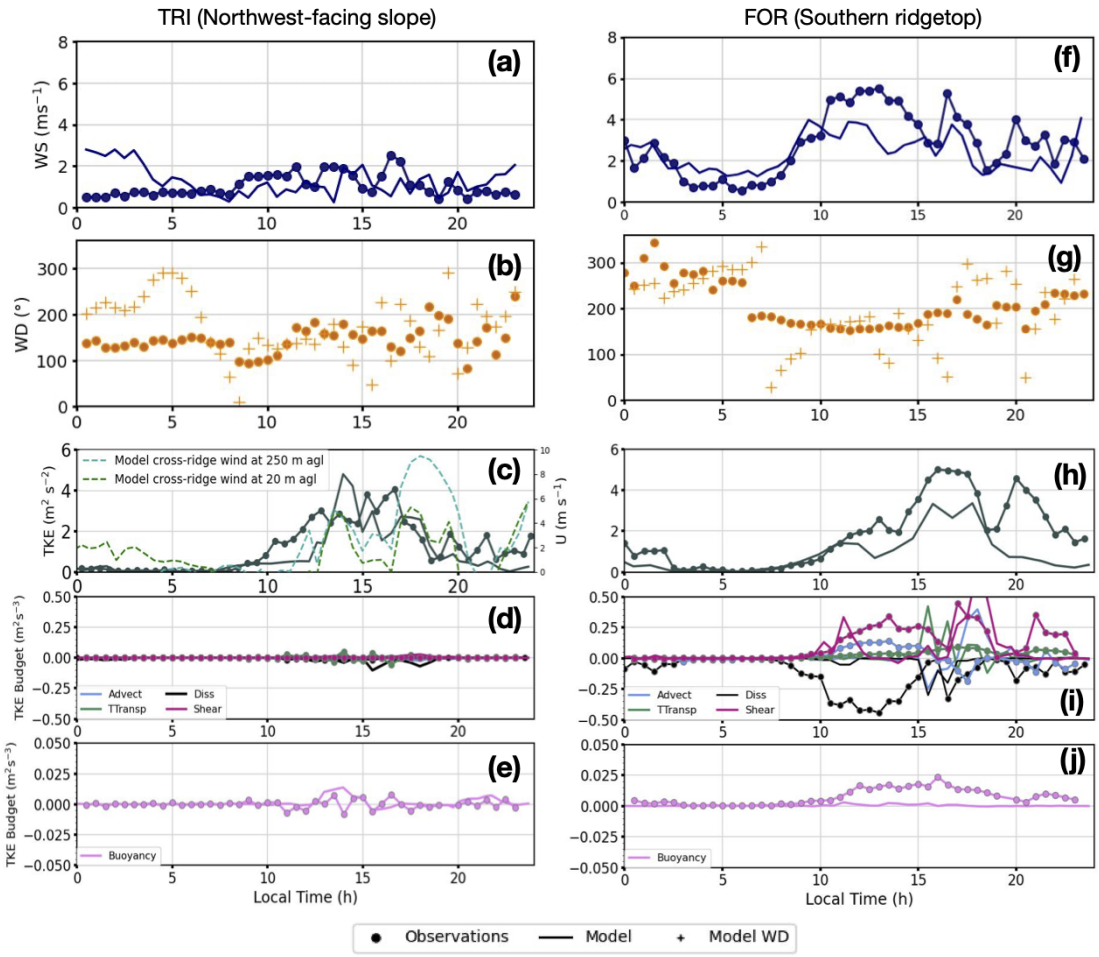

Figure 3.6: Time series of surface wind speed (a, f), wind direction (b, g), TKE (c, h), and vertical TKE terms (d,e,i,j) on 19 August, 2016 (started at 0600 UTC) from both observations (dots), and model output (solid lines) for the northwest-facing slope (TRI, a-e) and southern ridgetop (FOR, f-j) stations. The dashed lines in panel c denote the horizontal cross-ridge wind (u) at 20 and 250 m agl for comparison. For TKE calculations, sonic anemometer data was low-pass filtered and decimated to $f = 1\ s^{-1}$ from the 20 s^{-1} raw sampling rate. For consistency, both the model and observed TKE are averaged over 30-min.

0.002 m^2s^{-3}, while at FOR, buoyancy and vertical shear were both contributing to TKE, reaching up to $\sim$ 0.006 m^2s^{-3}, respectively.

However, by 3 pm, the dominant TKE production mechanism is horizontal wind shear, with maximum of about 0.024 m^2s^{-3} at the surface and 600 m above ground at TRI. Buoyancy, vertical shear, and turbulent transport also exhibited maxima close to the surface at about 100 m above ground level. In comparison, at FOR, vertical shear is the dominant budget term, with a peak of about 0.06 m^2s^{-3} at 250 m above ground level.

Notably, the rise in horizontal or vertical shear production at both stations relatively corresponds with the increase in TKE, as illustrated in Figure 3.5d and h, while other terms can also act as source or a sink at various heights above ground.

At 6 pm, buoyant production ceased entirely at both locations, while shear production was more pronounced near the surface, exceeding 0. 1 m^2s^{-3} at both TRI and FOR stations at about 100 m above ground. At this time, horizontal shear was a significant production term at the TRI valley location, while vertical shear production was the dominant term at the FOR ridgetop location near the surface. Although horizontal shear is a crude estimate of horizontal wind-gradient in the valley area, the analysis indicates the importance of horizontal shear in TKE production within the valley area. Conversely, at FOR, significant contribution of vertical wind shear based on both simulations and observations (Figure 3.5i) indicates local wind-gradient as the main production mechanism for TKE. Overall, the TKE budget is not fully closed at both the study sites. The extent to which the TKE balance is closed provides some indication of the importance of horizontal heterogeneity, impacting the pressure correlation, and other horizontal redistribution terms.

To investigate the source for the enhanced TKE at TRI, Figure 3.8 presents a time series of simulated horizontal and vertical shear terms at 20 m, and 250 m above ground (equivalent to the elevation at which up-valley wind speed was the largest, and of Fortress ridge, respectively). At both 20 and 250 m above ground, horizontal shear of TKE played a significant role in TKE production during the period of increased turbulence between 1 and 8 pm, while vertical shear had a lesser contribution to the total TKE production. The source of horizontal shear production was found to be due to horizontal shear gradients in wind speeds for the up-valley flow (Goger *et al.*, 2018). In this study, the correlation

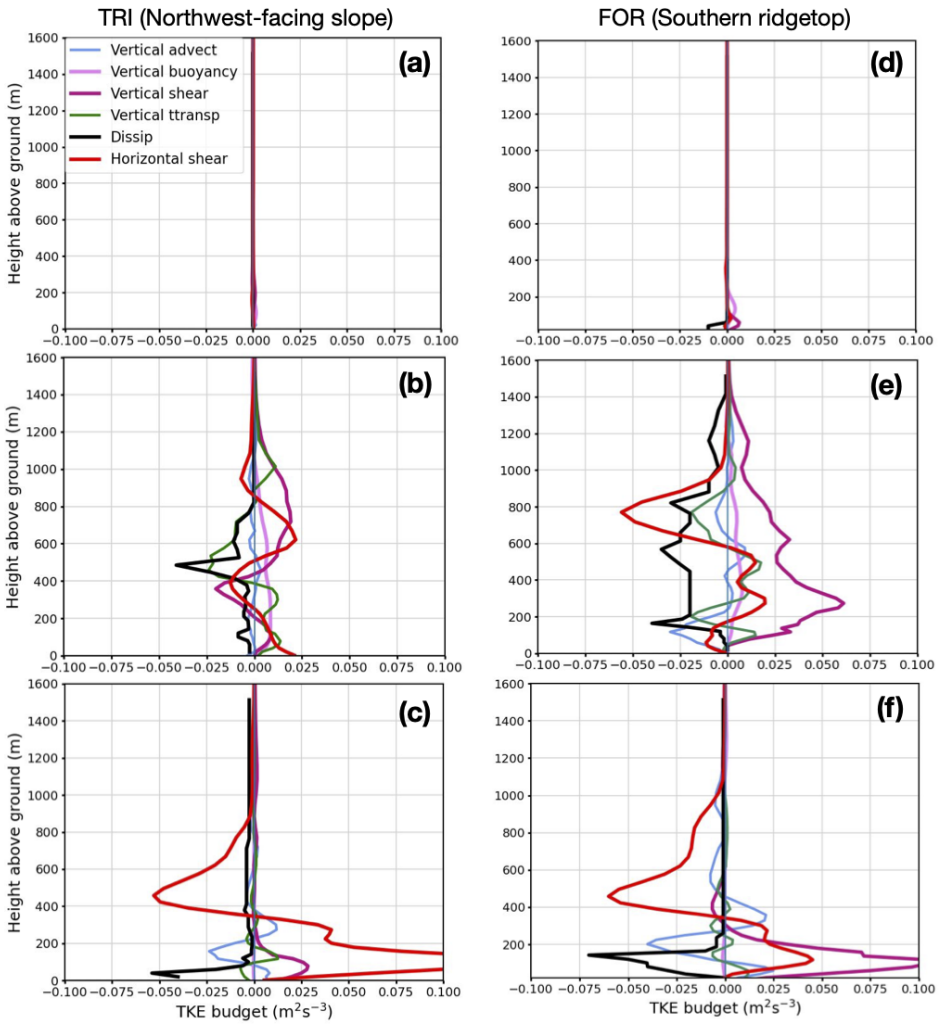

Figure 3.7: Profile of vertical TKE budget terms and horizontal shear term at 9 am (a, d), 3 pm (b, e), and 6 pm (c, f) from model output at the TRI and FOR stations on 19 August, 2016. Note that horizontal shear production includes the estimate of two terms Equation (2) along the cross-ridge u wind component.

between the simulated cross-ridge flow at 20 and 250 m above ground and the surface TKE at certain instances (Figure 3.5c), and the cease in TKE production with the sunset implies that horizontal wind-gradients within the cross-ridge flow, along with interactions between the cross-ridge and along-valley flow, contributed to horizontal shear production at the northwest-facing slope.

In fact, Figure 3.9 presents the daily mean TKE and wind speed for selected days (both sunny and cloudy) in July and August, for which eddy covariance data were available at both the TRI and FRG stations. TKE at TRI exhibited a strong correlation with the wind speed at FRG ($r^2 = 0.6$, $p_{value} = 0.01$), in contrast to the correlation between TKE and wind speed at TRI, which showed a weaker coefficient ($r^2 = 0.3$, $p_{value} = 0.1$). The wind direction at FRG was quite variable throughout the day, and exhibited variations at similar hours for different days. This suggests advection of TKE transported from FRG may not have a significant impact on TKE in the valley, but the correlation between TKE in the valley and wind speed at FRG affirms the influence of the cross-ridge flow on the TKE production at the northwest-facing slope.

Time Series: Northern Ridgetop Station

Figure 3.10 shows the corresponding time series of wind speed and direction, TKE, and the associated vertical budget terms for the FRG ridgetop station. At the FRG ridgetop station, after sunrise, the flow was initially southeasterly $\sim 100^\circ$ towards the ridgetop and continued into the afternoon, before switching to northwesterly $\sim$ 250-300° between 3 pm and 8 pm (Figure 3.7a, b), aligning with the cross-sections in Figure 3.4. Model underpredicted wind speeds after 10 am for most of the day, and wind direction changed to northwest about 2 hours earlier than the observations. The rise in observed TKE correlated with the increase in observed wind speed (Figure 3.7c). Model's underestimation of wind speed led to an underprediction of the observed TKE at this location, with a maximum difference of ~ 7 m^2s^{-2}. For comparison, model's wind speed at 500 m above ground showed higher wind speeds, corresponding to the observations, while the simulated TKE at this height remained low later in the afternoon. Both simulations and observations agreed upon minimal to no contribution from the vertical TKE budget terms to the TKE

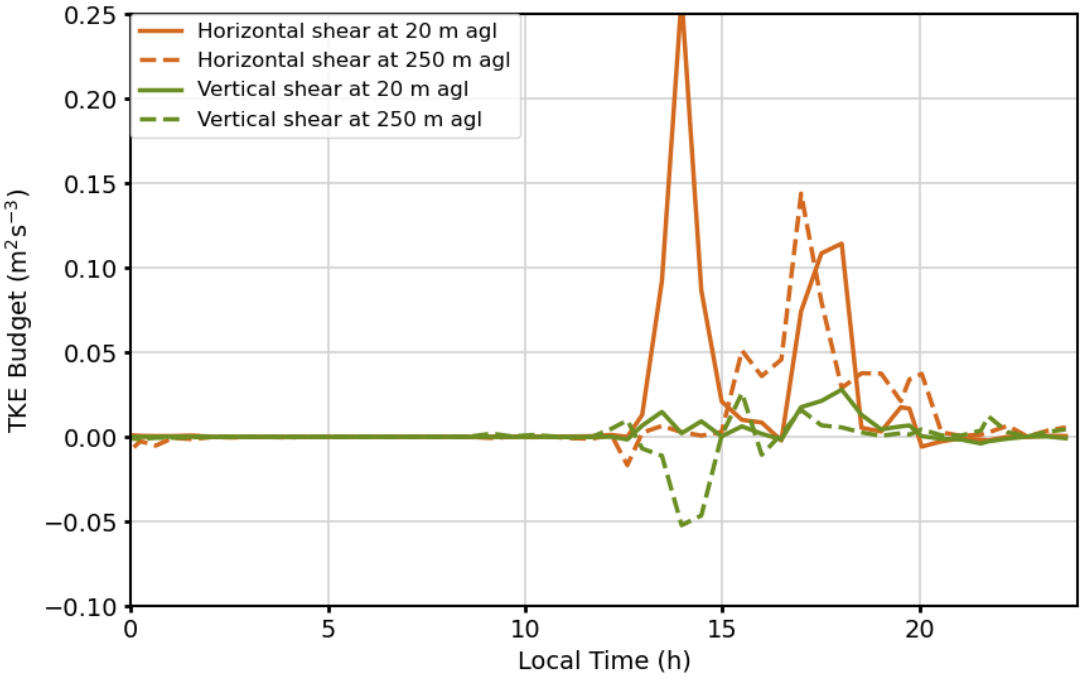

Figure 3.8: Time series of horizontal shear production (orange) and vertical shear production (green) from model output at 20 m agl and at 250 m agl at the station TRI on 19 August, 2016.

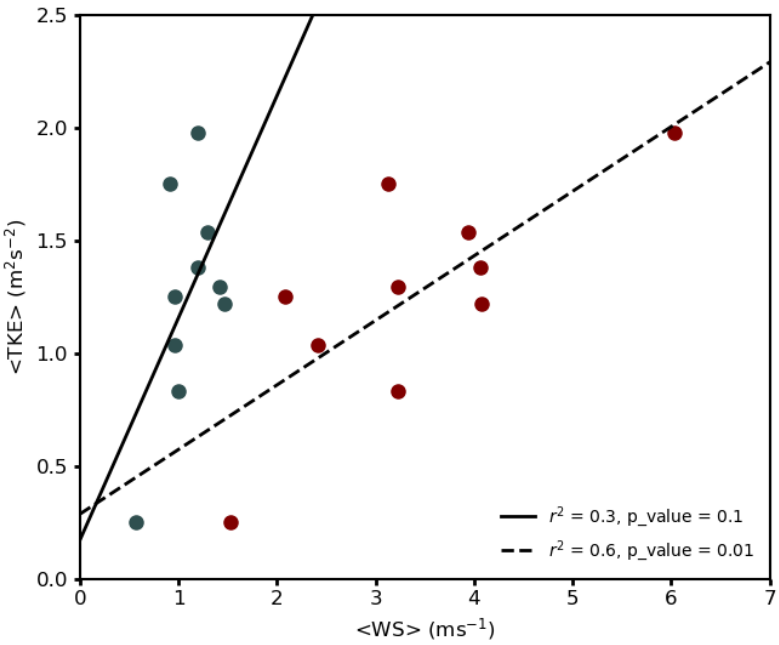

Figure 3.9: Observed daily mean TKE and wind speed (U) at the TRI and FRG stations. 8, 10, 22 , 23 , and 24 July, as well as 17-21, and 23 August, 2016, were selected for this analysis with high quality eddy covariance data available for both locations. Grey circles represent both the TKE versus wind speed at TRI, while red circles represent TKE at TRI versus wind speed at FRG.

at the northern ridgetop (Figure 3.7d).

Similar to TRI station, time series of horizontal shear calculated at FRG with another station (FRGS) at similar altitude revealed horizontal shear as the main production term at the surface and at 500 m above ground, concurrent with the rise in simulated TKE. Although model underestimated TKE later in the day at the northern ridgetop, horizontal shear from the cross-ridge wind-gradient introduces a source for TKE production at this location. some of the potential reasons for model's failure in predictions of surface wind and TKE can be due to smoothing of topography, affecting the steeper mountain crests around FRG station. The smoothing can decrease the intensity of channeling of wind flows and gusts from higher elevations toward lower elevations, which in turn would smooth out the horizontal wind-gradients toward the surface. Another explanation would be due to residual layer above the ridgetop. The vertical turbulence ceases, but horizontal turbulent motions can persist. Since model might have stabilized earlier than reality after the sunset at this location, it underestimated the horizontal turbulence and TKE.

Observations over July and August highlighted that the complexity of wind flows at the FRG ridgetop, displaying varying wind direction and strength on different days. Even if there are none to weak synoptic flows present, various flows can influence the wind patterns on the Fortress ridgetop. These include drainage flows from the crest on the south-west, cross-valley circulation due to the shift in the location of up-valley flow (Weigel & Rotach, 2004), dynamical orographic flows crossing over the mountain barrier on the north to northwest side of the Fortress valley which happens when the air is unstable enough to pass over or gets diverted horizontally around the mountains (Whiteman, 2000), and flows from the larger valley on the southeast side toward the higher elevations during daytime. Interaction of the ambient winds with topography and orographic lifting can cause gusty winds during summer time (Whiteman, 2000), which is frequently observed at the FRG station. Without proper observations it would be difficult to concur which processes are more relevant to flows at the FRG ridgetop, and how they may affect TKE production at this location, which should be considered for future studies.

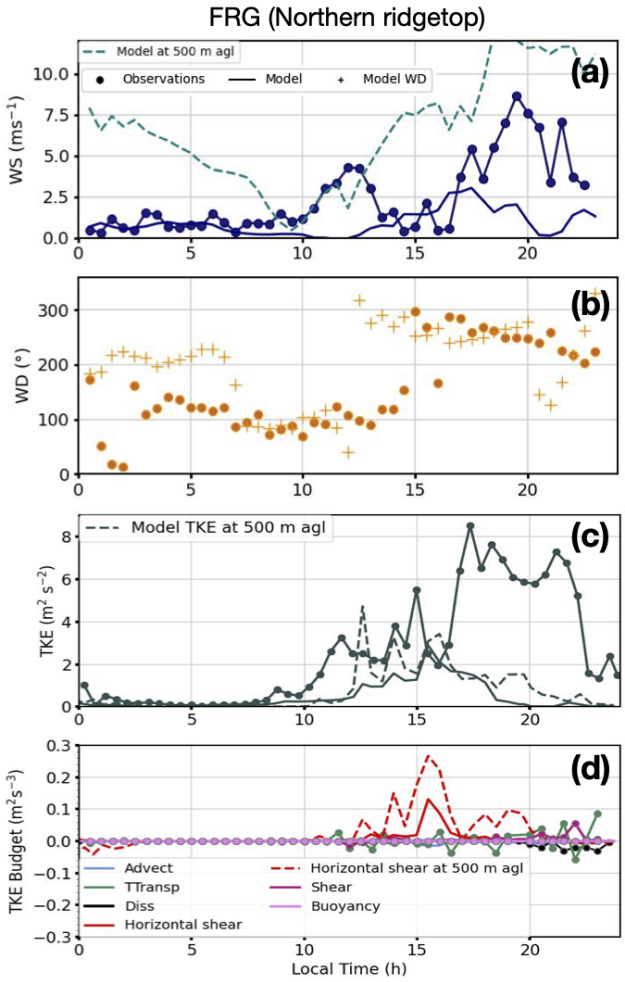

Figure 3.10: Time series of surface wind speed (a), wind direction (b), and TKE (c) on 19 August, 2016 from both observations (dots), and model output (solid lines) for the northern ridgetop (FRG) station. The dashed lines in panels a and c denote the horizontal wind (u) and TKE at 500 m agl for comparison, respectively. Note that horizontal shear production includes the estimate of four terms Equation (2) with rotated velocity components using both FRG and FRGS stations and velocity variances at FRG station.

3.5 Summary and Conclusions

In this study, near-surface turbulence characteristics of the daytime atmosphere in a shallow high Alpine valley are investigated. This analysis makes use of high-frequency eddy covariance measurements at three different locations within the Fortress Mountain research basin, as well as LES using WRF. A clear-sky summer day in presence of weak synoptic winds, which does not overwhelm thermally-driven valley and slope flows is considered and simulated. An up-valley flow is evident in simulated cross-sections, inclined towards the northern slope. Even though there is a lack of proper observations at the northern slope to support simulations, the observed wind at the BNS valley station situated at the west end of the valley (Figure 3.1) reveals an up-valley flow with low wind speeds < 2 ms^{-1} for the summer months, while the observed winds at the TRI station are most often weak slope flows, despite its location near the valley bottom. This suggests that the shift in the up-valley flow towards the northern slope is mostly affecting the northeast entrance of the valley.

Both model and observations indicate the presence of cross-ridge flows throughout the day, and the TKE at the northwest-facing slope station (TRI) is strongly correlated with the wind speed at the northern ridgetop station (FRG). But TKE at TRI falls fast once the up-valley flow breaks down with diminishing convection, and as the late afternoon stable boundary layer sets in. Both simulated wind speed at 20 m and an equivalent elevation (250 m agl) to FRG ridgetop above the TRI station, and the observed wind speed at FRG reveal that the increase in wind speeds coincides with an afternoon rise in the observed and simulated TKE at the TRI station. This may suggest contribution from interactions of cross-ridge and up-valley flow, to the TKE budget, and the role both play in generating turbulence in the valley.

The vertical TKE budget terms from observations and model output at first level at TRI did not explain the TKE at this location. While at the southern ridgetop (FOR), TKE seems to correlate well with the wind speed at 15 m agl, and both observed and model vertical TKE budget analysis indicate considerable contributions to TKE, specially from vertical shear production. The results show that the vertical TKE budget alone may not account for all the increase in surface TKE at the northwest-facing slope. In fact, both

vertical profile and time series of TKE budget at 20 m and 250 m above the TRI location reveal strong horizontal shear at higher elevations. This further suggest the possibility of TKE generated through interactions of cross-ridge flow and up-valley flow, and horizontal wind-gradients in cross-ridge flow at higher levels above ground, contributing to TKE at the surface and at above the northwest-facing slope.

The observed TKE at the northern ridgetop reaches values as high as 8 m^2s^{-2} in the afternoon when the cross-ridge flow has the highest wind speed. The strong correlation between the observed wind speed and TKE at this location suggests a locally shear-driven source for TKE, associated with the cross-ridge flow. Even though the model underpredicted wind speed at the FRG ridgetop station, simulated cross-sections predicted stronger winds over the valley at elevations equivalent to that of FRG ridgetop. Although a comprehensive TKE budget analysis at the northern ridgetop is not feasible due to an underestimation of the simulated TKE, the time series of TKE budget from observations and model output at the surface suggests minimal to zero contribution to TKE at this location. However, time series of horizontal shear production from the model output at the surface and at 500 m agl shows some contribution to the TKE related to horizontal wind-gradient of cross-ridge winds before late afternoon, where model fails to predict the TKE due to early stabilization of boundary layer compared to reality.

It is finally noted that the connection between the turbulent state in the valley and vertical and horizontal exchange in the boundary layer above the valley have indications about the impacts of these processes on sensible heat and evaporative fluxes in the valley. The improved understanding of how turbulence is affected by the local and non-local flows in complex topography helps with improved calculations and evaluations of exchange processes in mountainous terrains. With limitations in observations in high mountain areas, high resolution models can help resolve near-surface processes, and be used as an input to hydrological models for future projection predictions of water resources. However, the results in this study affirms that current 1D turbulence parametrization in numerical weather prediction models is not suitable for a complex terrain, and a full 3D parametrization of turbulence is essential for correct predictions of the turbulence state of the boundary layer and the associated exchange processes in mountainous environment.

Chapter 4

Influence of elevation dependent heterogeneity on heat and evaporative fluxes in complex terrain

4.1 Introduction

Mountains serve as the headwaters of major river basins that provide water for downstream agriculture, industry and communities, and mountainous terrain influences water availability through precipitation, evapotranspiration, and complex land-atmosphere interactions imposed by orographic effects (Fang *et al.*, 2023). Heat and evaporative exchange processes at the land surface have long been recognized as one of the most important processes in the determination of the exchanges of energy and mass among the hydrosphere, atmosphere and biosphere (Brutsaert, 1982). Although heat fluxes and their vertical and horizontal transport are key elements of the hydrological cycle, and have been the focus of field campaigns, most studies have been performed in homogeneous conditions over flat terrain.

Due to their complex shapes, mountain studies pose several challenges that arise from incompatibility with representative measurements and accurate modelling. The major

reason for the failure in quantitative measurements and model evaluation is that mountain or hilly terrain introduces differential solar heating and shading, local flows (i.e. slope and valley flows), and heterogeneity in soil moisture, heat and evaporative fluxes depending on elevation and vegetation cover (Pomeroy *et al.*, 2023; Kafle & Yamaguchi, 2009; Kiemle *et al.*, 2011; Rotach *et al.*, 2015; Zhao & Ainong, 2015; Li *et al.*, 2018). Rotach *et al.* (2007) showed how mean daily cycles of net radiation and sensible heat fluxes changed during the day (convective sunny day), depending on slope orientation. The resulting spatial heterogeneity of fluxes limits our understanding of the important factors controlling evaporative processes in mountainous terrain.

Modifications in the surface radiation budget and turbulent fluxes (heat and evaporative) with spatial variability in soil moisture in complex topography emphasizes the significance of the feedback processes between soil moisture, precipitation, and evaporative fluxes (Eltahir, 1998; Small *et al.*, 2003; Maxwell *et al.*, 2007; Rihani *et al.*, 2015). In high mountain areas, drastic differences in elevation, slope, and aspect, along with vegetation cover can cause significant differences in surface properties, and land atmosphere interactions (Dornes *et al.*, 2008).

The goal of this study is to quantify the influence of elevation dependent topographical features (i.e soil moisture, solar heating,vegetation) on the near surface exchange processes (i.e sensible and latent heat fluxes) in a mountainous drainage basin. The objective of this study is to quantify the variability of the sensible and latent fluxes with soil moisture content and net radiation, as influenced by elevation, vegetation, and wind flows during a summer period when heat and evaporative fluxes from the surface are at their maximum.

4.2 Study Sites and Data Processing

The study sites are located at three different elevations in the Fortress Mountain Research Basin, Alberta, Canada (FMRB), a cold continental high mountain basin dominated by a long snow covered period from October through June and a short cool summer (Figure 4.1). Tripod (TRI) is located near the base of a north-west-facing slope, and within the Fortress valley (2060 m above ground level), while Forest Ridge (FOR) and Fortress Ridge

(FRG) are located on ridgetops bounding this valley (2080 m and 2323 m above ground level, respectively). The vegetation cover also differs at the three locations, with patchy shrubs at TRI, needleleaf forest at FOR, and sparse, low grass and moss at FRG.

The period of interest was the months of July and August, 2016, to investigate the variability of heat and evaporative fluxes with elevation when the fluxes are at their maximum value during the summer months. The specific timing of the research also provided the opportunity to use Large-eddy Simulation (LES) results (Rohanizadegan *et al.*, 2023) for further evaluations.

Net radiation was observed with net radiometers (NR Lite2; Kipp and Zonen, Delft, the Netherlands) installed at 2 m, 15.5 m, and 5 m above ground level at the TRI, FOR, and FRG stations, respectively. Soil moisture was measured at 3 depths below the ground surface at the TRI location (5, 15, and 30 cm below ground), and soil temperature was measured at 2 depths below the ground surface (2, and 15 cm). Soil moisture and temperature at the FOR location were measured at 2 cm below the ground, and at the FRG location at 6.5 cm below the ground surface. Rainfall was measured at the FOR location, using a tipping bucket rain gauge with datalogger (Onset Computer Corp., Bourne,MA, USA).

The latent (LE) and sensible (H) energy fluxes were measured with eddy covariance (EC) instrumentation during the same period as the meteorological data. EC measurements at the FOR ridgetop site were collected with a three-dimensional sonic anemometer (CSAT3; Campbell Scientific Inc., Logan, UT, USA) and an open-path infrared CO2/H2O gas analyzer (IRGA) (LI-7500; LI-COR Inc., Lincoln, NE, USA) mounted at a height of 15.5 m above the surface, on the meteorological tower described above. EC measurements at the TRI valley and FRG ridgetop sites were collected with a similar anemometer to the FOR site at 2 m above ground level, but the fast humidity was measured with Krypton hygrometers (KH20, Campbell Scientific Inc., USA). The EC systems sampled fluxes at a frequency of 20 Hz, and the collected raw EC data were detrended and block averaged over 30-min intervals for flux estimates using the software (EddyPro, LiCOR) provided by Campbell Scientific (Campbell Scientific Inc., Logan, UT, USA), which completes all standard raw data corrections and processing, including air density correction for open path sensors (Reba *et al.*, 2009), corrections for coordinate rotation (double coordinate rotation,

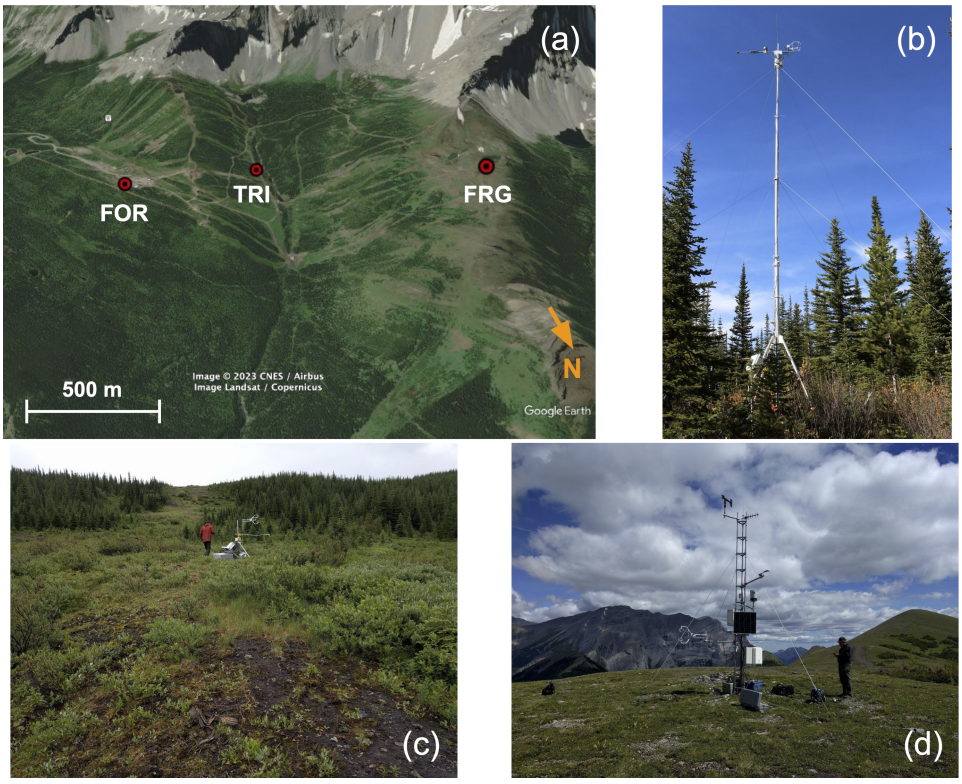

Figure 4.1: (a) Map of Fortress Mountain Research Basin, marked with the locations of eddy covariance equipment. Note that image is looking south in (a). Images of study locations (b) Forest ridgetop station (FOR), (c) Tripod valley station (TRI), (d) Fortress ridgetop station. Note that EC systems are installed at 2 m above ground at TRI and FRG stations, and 15.5 m above ground at FOR station.

Kaimal *et al.*, 1994), and time lag and sensor separation, following common Fluxnet protocols (Kaimal *et al.*, 1994; Aubinet *et al.*, 2012). After the data was quality checked using the software for a non-stationarity test given by Foken & Wichura (1996) at its standard 30% level, only the days that had more than 85% of data available within the 24 hours were chosen for further data analysis to avoid any bias in daily averages.

4.3 Numerical set-up

The Weather Research Forecast (WRF) model in large-eddy simulation (LES) mode was used to simulate the flow and turbulence structure for a fair weather sunny day, Aug 19. Full details on simulation set-up, initialization and boundary conditions, and experimental design can be found in Rohanizadegan *et al.* (2023). The model set-up that has proven to yield the best results for July 18 is the so-called "LESLF_shade_cloud" setup (local filtering LES with topographic shading and slope effects on radiation with the cloud parametrization only applied for the coarser domain) described in the above reference, was used for August 19. In this setup, the model is run in a one-way nesting mode. A grid of 8.1 km horizontal spacing is initialized from Medium-Range Weather Forecast Reanalysis (ERA-interim) data, and is then successively nested down to grids of finer horizontal spacings (2.7 km, 0.9 km, and 90 m). All of the simulations start at 0600 UTC to account for a 6-hour spinup period, while the LES domain was initialized from the output of domain at 0.9 km at 1200 UTC to run concurrently after the spinup period.

4.4 Results

In this section, the controlling factors on near surface turbulent fluxes are described for the three locations. This was done in three different ways: (1) Assessing the relationship between different elements for dry and wet soil conditions; (2) Comparing fair weather (fully sunny conditions) midsummer days with more hours of sunlight ($\approx$ 13 hours) versus late summer days ($\approx$ 11 hours); and (3) Evaluating model predictions for radiation and sensible and latent fluxes for a case study (19 August) for which LES was available.

4.4.1 Wet and Dry Days

Wet and dry days were selected based on an arbitrarily chosen cutoff depending on the value of the soil volumetric water content (VWC) at each of the study sites. At the TRI station, wet days were chosen when VWC in the top 5 cm of the soil was $> 0.35\ m^3/m^3$, and $< 0.35\ m^3/m^3$ for dry days, with a full range $0.32 <$ VWC < 0.39 at this location. At the FOR station wet days were selected when VWC in the top 2 cm of the soil was $> 0.3\ m^3/m^3$, and $< 0.3\ m^3/m^3$ for dry days, with full range $0.21 <$ VWC < 0.36. Finally, wet days at the FRG station were selected when VWC in the top 6.5 cm of the soil to be $>0.22\ m^3/m^3$, and $< 0.22\ m^3/m^3$ for dry days, with full range $0.19 <$ VWC < 0.25. The criterion for choosing wet and dry days varied depending on site elevation. In mountainous terrain, the soil is typically drier at higher elevations, since it is better drained and exposed to greater wind speed, lower relative humidity (Table 1), and greater shortwave irradiance.

The latent heat fluxes appeared to be unaffected by the soil moisture content at all study sites (Figures 4.2, 4.3, and 4.4), regardless of whether the soil was dry or wet. Although the correlation coefficient differed slightly between stations, it was evident that net radiation played a significant role in controlling latent heat fluxes at all three locations, both on wet and dry days, with FOR exhibiting the strongest correlation ($r^2 = 0.9$) among all the stations. Similarly, sensible heat fluxes had moderate to strong correlations with net radiative fluxes at all locations, with FOR ridgetop net radiation showing the most significant influence on sensible heat for both the wet and dry days. The variations in correlation coefficients between the sites could be related to the number of data points used in the analysis affected by the data collection limitations (i.e non-stationarity), and more long term studies are required to verify these findings.

Furthermore, there was a moderate relationship between wind speed and latent heat at the TRI station for both wet and dry days, while FRG and FOR locations proposed weaker correlations between the wind speed and latent heat fluxes. This suggests that near-surface wind speed (i.e. slope flows) could have a considerable influence on latent heat exchange at the TRI station, despite the low wind speeds (< 2 m/s) at this location.

When wet and dry days were compared, soil moisture content did not seem to greatly impact correlation coefficients between different elements at any of the locations. However,

at the TRI station, there was a stronger relationship between turbulent fluxes and net radiation on dry days as compared to wet days. But given turbulent fluxes had a strong relation with net radiation with closer correlation coefficients at FOR and FRG ridgetops for both wet and dry days, the wetter soil along with more sparse vegetation at TRI can cause a faster and more significant response to the changes in near-surface air temperature, and resulted in more deviations in turbulent fluxes between the wet and dry days.

4.4.2 Effect of Variability in Net Radiation in Midsummer Versus Late Summer on Heat Fluxes

The observed averages of two sunny (i.e. least amount of clouds observed in time series of net radiation) midsummer days were compared against three sunny late summer days to investigate the impact of topographic shading and the overall reduction of net radiation due to changes in solar altitude angle over time (i.e. maximum solar elevation angle during daytime reached $\approx 60^{\circ}$ in mid-July and $\approx 53^{\circ}$ in mid-August) on latent heat fluxes (Figure 4.5).

On average, net radiation decreased from midsummer to late summer with a reduction of about 31 W/m^2 at TRI, 58 W/m^2 at FOR, and 48 W/m^2 at FRG (Table 1). The net radiation declined from mid- to late summer at all locations, but it was greater at the ridgetops (FRG and FOR) in midsummer, being more exposed to solar irradiance compared to the valley station (TRI). The smaller decline in net radiation at the TRI location from mid- to late summer was found to be related to lower nighttime emitted terrestrial radiation, and can be caused by the colder surface temperature and larger cold-pool effect in the valley. Similarly, latent heat fluxes at the stations decreased from mid- to late summer, but to a lesser degree, with reductions in latent heat of about 7 W/m^2 at TRI and FRG, and 17 W/m^2 at FOR. The drier soil and less humid air at FRG (Table 1) lead to less moisture evaporation from the surface into the atmosphere, resulting in a smaller change in latent heat flux at the high ridgetop compared to forested ridgetop (FOR). At TRI, slope flows can contribute to the enhancement of latent heat in August, and to the smaller difference in fluxes between mid- and late summer season.

While there was either no, or only a weak correlation observed between soil moisture

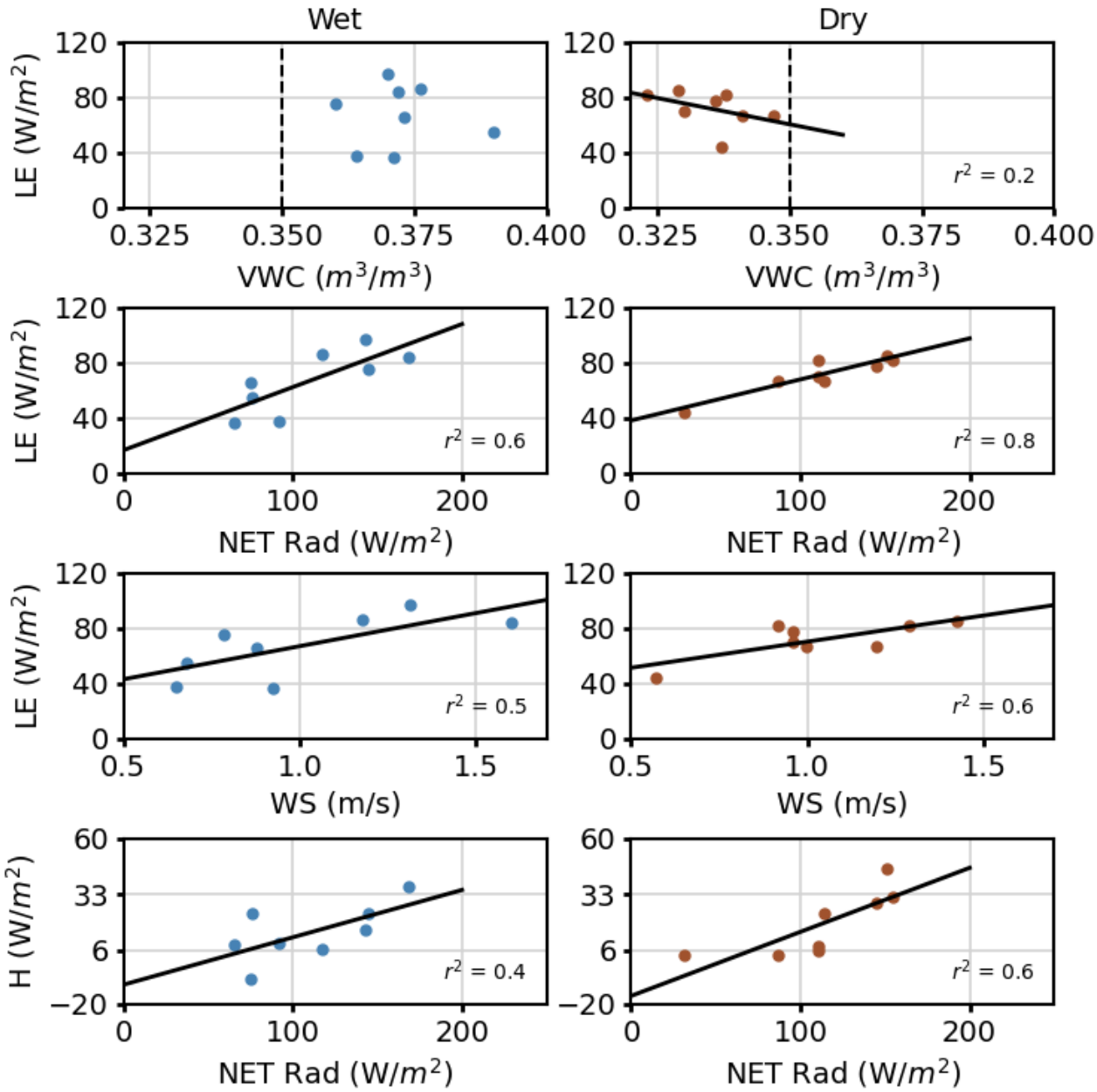

Figure 4.2: Relationships between different near-surface meteorological variables for the wet and dry days of the months of July and August at the TRI valley station. Each point represents a different day, with values averaged over the 24-hour period. Least squares linear fit and r^2 values are shown, except when r^2 was < 0.1.

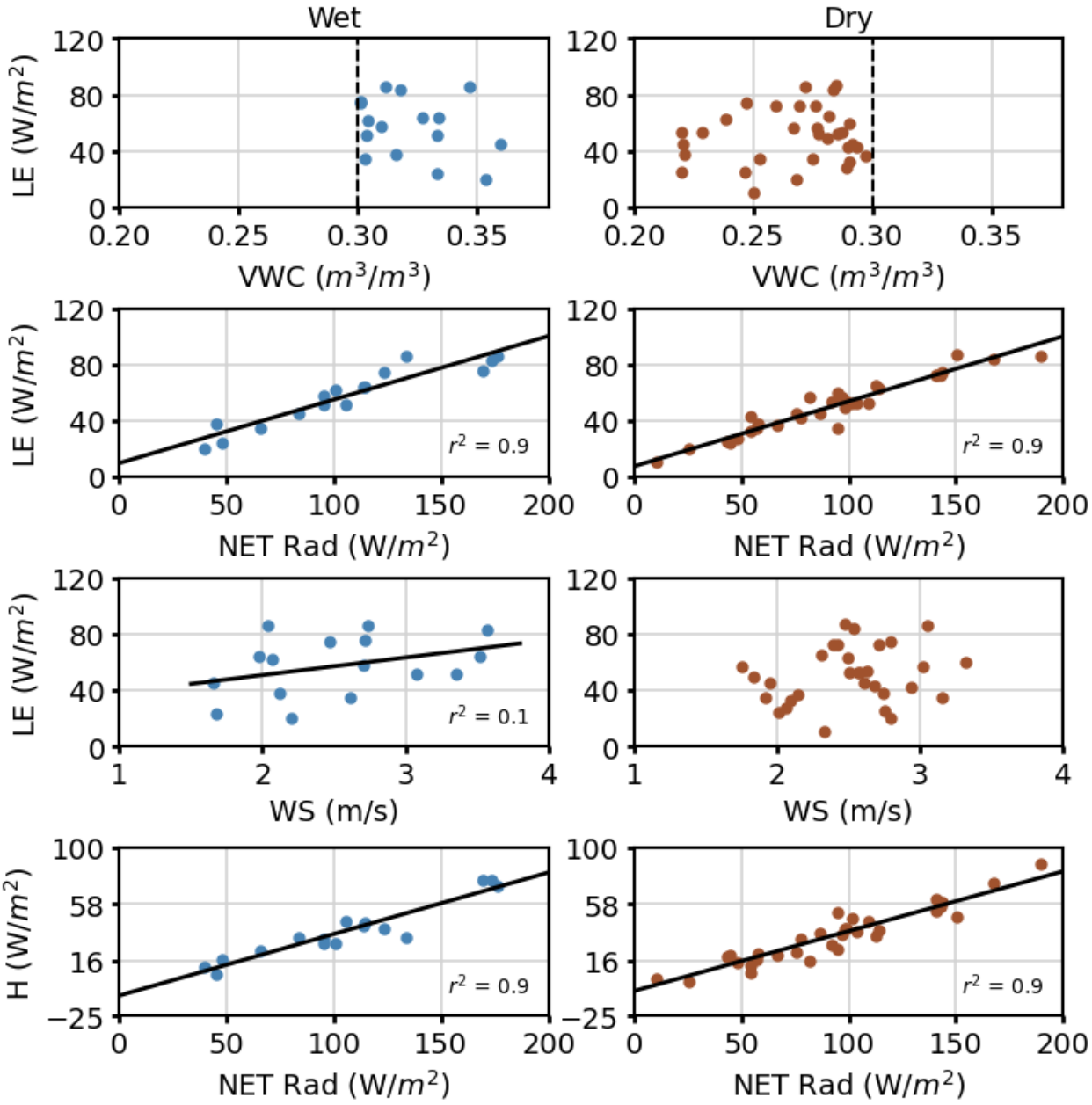

Figure 4.3: Similar to Figure 4.2, but for the FOR ridgetop station.

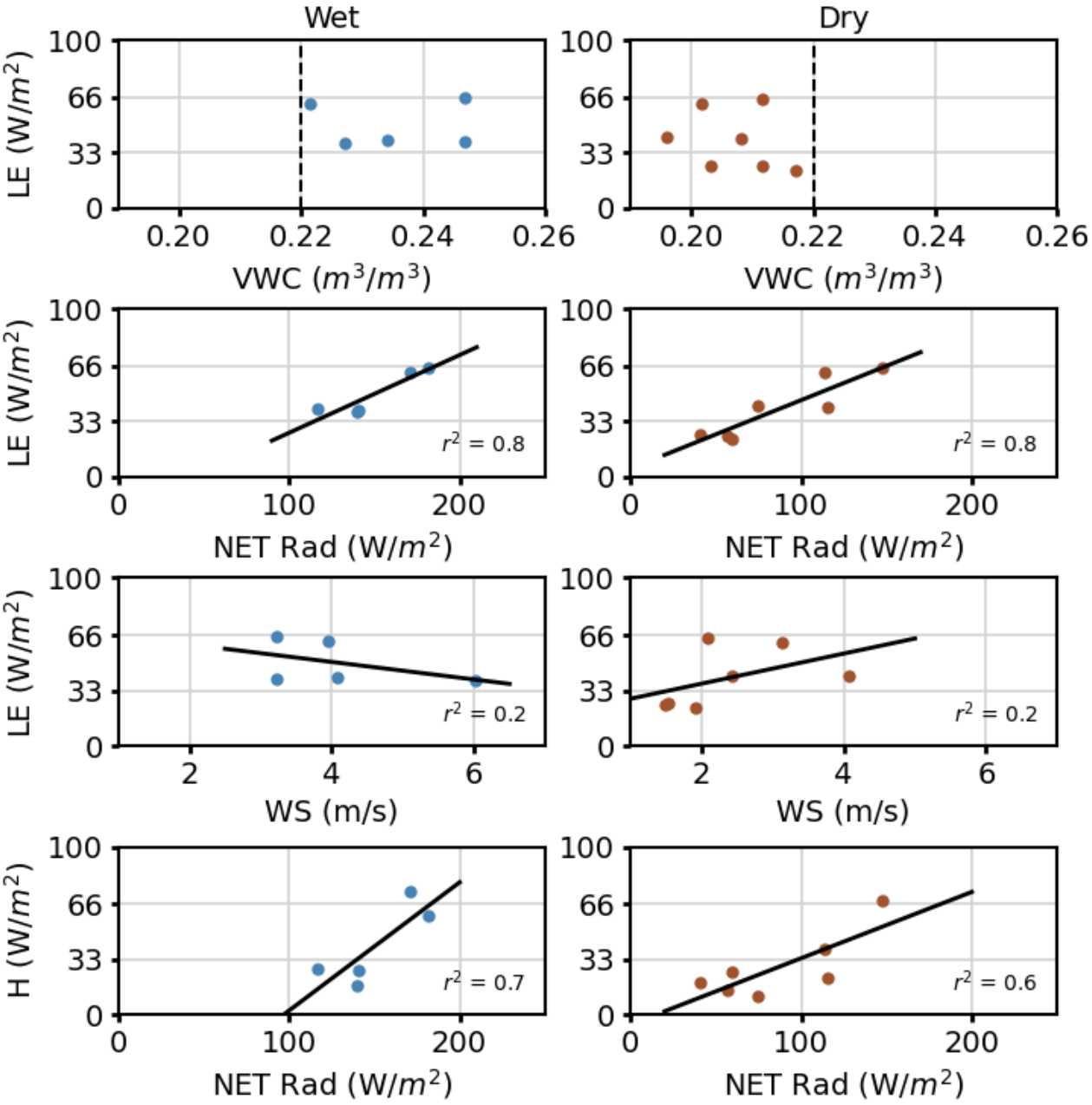

Figure 4.4: Similar to Figure 4.3, but for the FRG ridgetop station.

and heat fluxes at all three stations (as seen in Figures 4.2,4.3, and 4.4), the decrease in latent heat fluxes from the low-elevation station (TRI) to the highest ridgetop (FRG) during the late summer days can be explained by the overall soil moisture content at each of these locations, as detailed in Table 1. Specifically, TRI had the highest soil moisture content, which influenced its latent heat flux, whereas FRG had the lowest soil moisture content and, consequently, the lowest latent heat flux. Cooler soil temperatures (Ts) associated with wetter soils at the TRI station (as indicated in Table 1) contributed to lower sensible heat fluxes for both mid- and late summer days, but led to higher latent heat fluxes compared to the other locations. The decrease in late summer latent heat fluxes from the low to high elevation stations further emphasizes the impact of soil moisture on heat fluxes.

Sensible heat fluxes at all stations also decreased from mid- to late summer in line with the reduction in net radiation, with the most significant reduction occurring at FOR (36 W/m^2) and smaller at FRG (23 W/m^2) and TRI (24 W/m^2). This pattern can be attributed to various factors, including the station's location and topographic characteristics. Both the decrease in net radiation from mid- to late summer, and the topographic, soil, and land cover attributes contributed to the greater decline in sensible heat flux at the FOR ridgetop location. The shading by a tall canopy at FOR, likely results in a more significant reduction in surface soil temperature from mid- to late summer (as indicated in Table 1), and a larger response to the reduction in shortwave radiation from mid- to late summer.

4.4.3 Comparison Between Simulated and Observed Time Series of Turbulent Fluxes

The simulated net radiation at the three stations on a sunny day (19 August, 2016) reproduced the maximum observed radiation approximately 1 hour earlier (Figure 4.6). In Figure 4.7, the daily maxima in simulated latent and sensible heat fluxes occurred earlier than the maxima in observations, similar to net radiation. This confirms the dependency of latent and sensible fluxes on net radiation at all locations, as previously discussed for the observations. Consequently, the simulated turbulent fluxes were mainly overestimated,

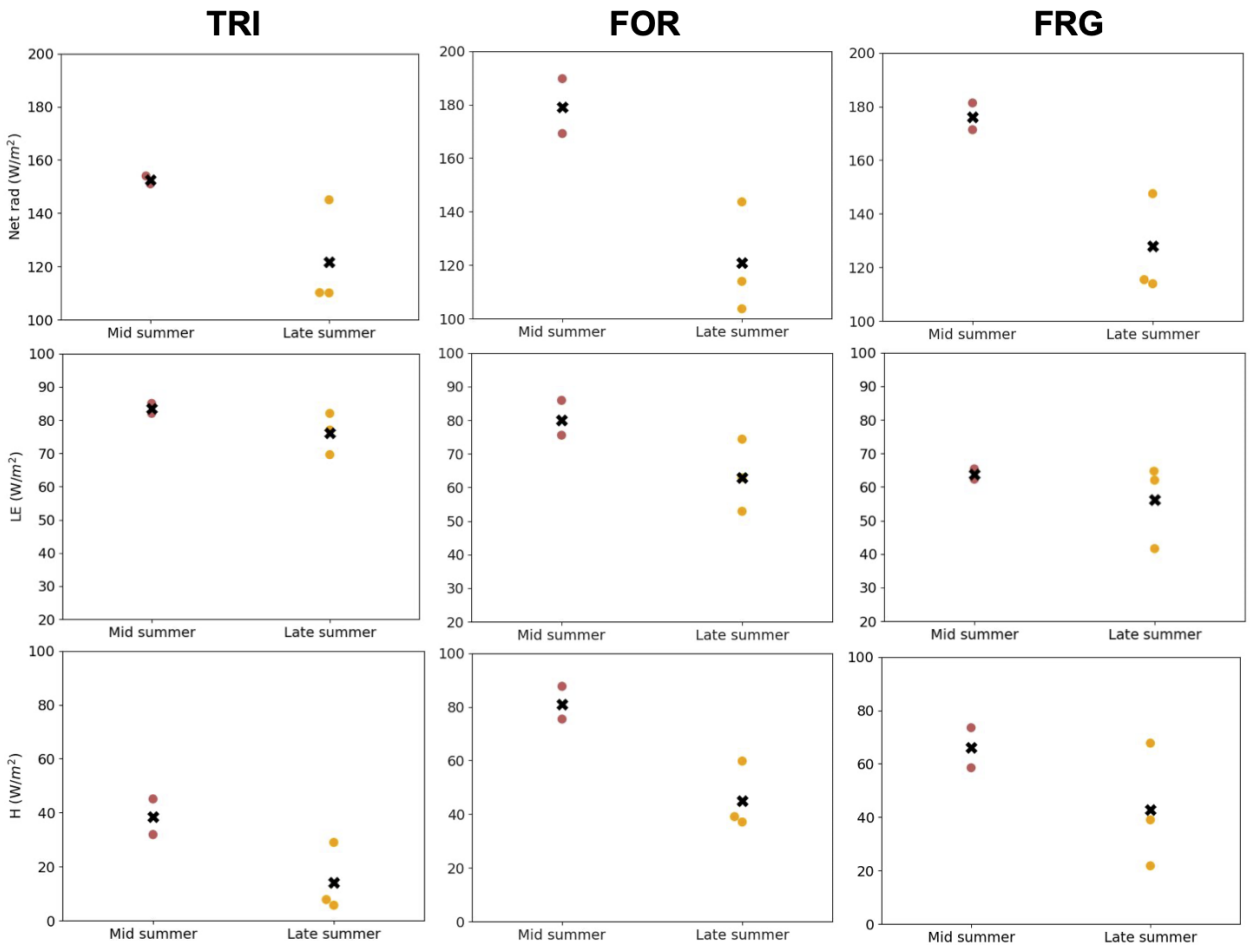

Figure 4.5: Observed daily average of net radiation, latent and sensible heat fluxes for the midsummer day and late summer days, from the low to high elevation stations, at the TRI (first column), FOR (second column), and FRG (third column) station. The x mark denotes the overall average for the mid and late summer days for each element.

Table 4.1: Mean values of observed net radiation (Net rad), latent heat (LE) and sensible heat (H) fluxes, volumetric soil moisture content (VWC), soil temperature (Tc), air temperature (Ta), relative humidity (RH), and wind speed (WS) at the three stations for the mostly sunny midsummer (8, 24 July), and late summer days (19, 20, 21 August).

	Midsummer			Late summer		
	TRI	FOR	FRG	TRI	FOR	FRG
Net rad (W/m^2)	178	179	176	115	121	128
LE (W/m^2)	92	80	74	77	63	55
H (W/m^2)	44	81	82	14	45	39
VWC (m^3/m^3)	0.34	0.28	0.23	0.32	0.24	0.2
Ts ($^\circ$ C)	12.3	14.0	13.5	12.0	12.5	13.3
Ta ($^\circ$ C)	11.3	13.4	11.7	11	13.6	11.7
RH (%)	58	55	5	77	43	22
WS (m/s)	1.2	2.9	3.9	0.9	3.2	2.5

especially before reaching their maximum in the afternoon. The most significant deviation in simulated sensible heat flux from observations happened at the FOR station, indicating the cooling effect of shading by a tall canopy on the underlying soil, a feature not captured by the model's land surface scheme (Noah-MP), as explained in Rohanizadegan *et al.* (2023). The daily maximum net radiation at the FOR station is also overestimated by the model more than the other locations, contributing to the overprediction of sensible heat at this site.

While the daily maxima in simulated and observed latent and sensible heat fluxes did not completely align, both the simulated and observed sensible heat fluxes averaged over 24 hours were greater at the FOR station (200 and 60 W/m^2, respectively) compared to the TRI station (60 and 29 W/m^2, respectively). This was expected, as the average net radiation at FOR was greater than at TRI. At FRG, the simulated average sensible heat was comparable to that of TRI, despite higher net radiation at the ridgetop than the valley. This is possibly due to the model's higher soil moisture content (0.32 m^3/m^3) compared to reality (0.2 m^3/m^3) at the FRG ridgetop, which led to more cooling of the soil temperature and consequently a reduction in sensible heat flux.

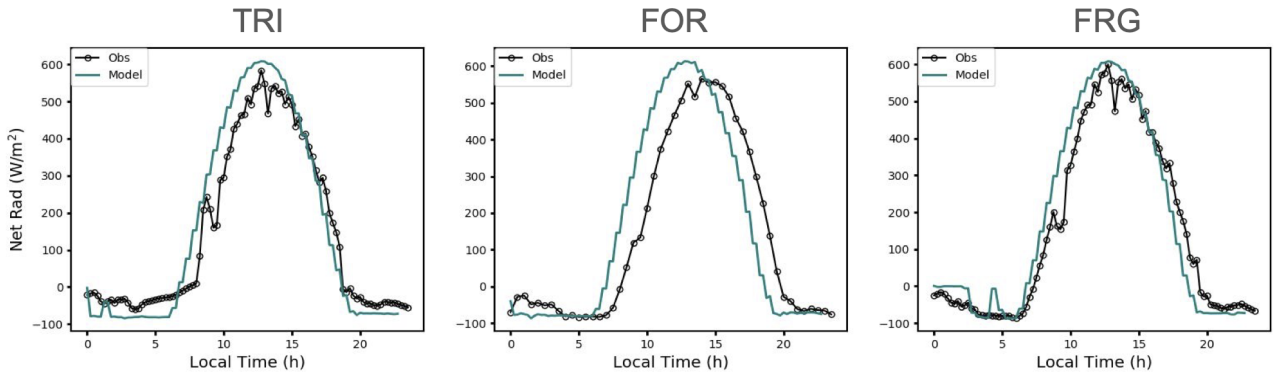

Figure 4.6: Time series of observed and simulated net radiation at the TRI, FOR, and FRG sites, on 19 August.

Observed latent heat fluxes were greater at TRI (77 W/m^2) compared to the high ridgetop station FRG (64 W/m^2), due to higher soil moisture content at TRI. Overall, it becomes apparent that local variables (i.e soil moisture content and net radiation) are impacted by topography, elevation and vegetation, and that seems to have a considerable influence on the daily turbulent fluxes.

4.4.4 Non-local Influences on Evaporative Flux

In complex terrain, horizontal and vertical exchange processes can play an important role in transporting turbulent fluxes, contributing to enhancement or losses of the fluxes (Schmidli, 2013; Rotach *et al.*, 2017). In this study, the latent heat flux at the TRI station strongly and moderately correlated with turbulent kinetic energy (TKE) on both wet and dry days (Figure 4.8), respectively. As discussed in chapter 3, TKE at TRI most likely originated from above the surface layer, primarily generated through interactions between up-valley and cross-ridge flows. The vertical and horizontal shear generated at higher levels were recognized as important sources of TKE within the valley. Meanwhile, vertical shear and advection were noted as a source of TKE closer to the ground, particularly during the presence of afternoon up-valley wind. The TKE at TRI also correlated with the wind speed at the northern ridgetop. Horizontal and vertical advection due to mountain processes

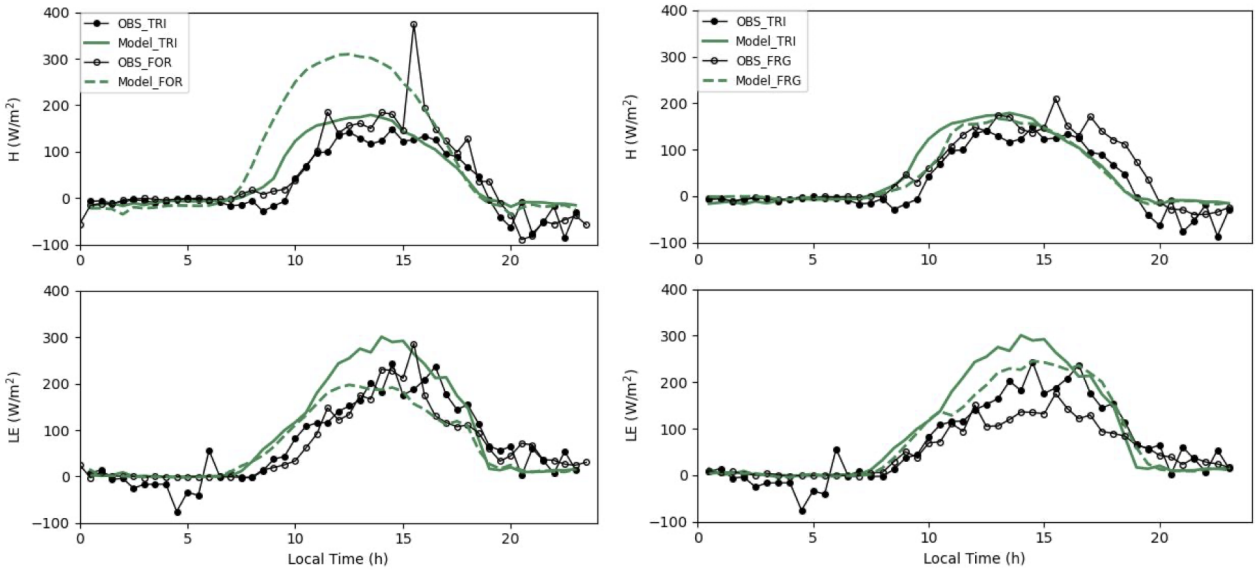

Figure 4.7: Time series of observed and simulated sensible and latent heat fluxes at the TRI, FOR, and FRG sites, on 19 August.

such as valley winds and cross-valley flows can influence the generation of turbulent fluxes (Schmidli 2013).

The observed correlation between TKE and latent heat at the TRI valley station might be an indication that horizontal and vertical exchange processes associated with up-valley and cross-ridge flows could influence horizontal and vertical heat and moisture transport, resulting in loss or enhancement in vertical turbulent fluxes in the valley.

4.5 Discussion

This study utilized three EC towers positioned in a valley, and forested, and tundra-covered ridgetops on opposite sides of the valley. Despite variations in vegetation type and elevation, the latent heat fluxes exhibited a weak correlation with soil moisture ($r^2 \geq 0.2$) but displayed a strong correlation with net radiation ($r^2 \geq 0.6$) at all sites, for both wet and dry days. Similar findings were reported by Williams *et al.* (2015), who observed a

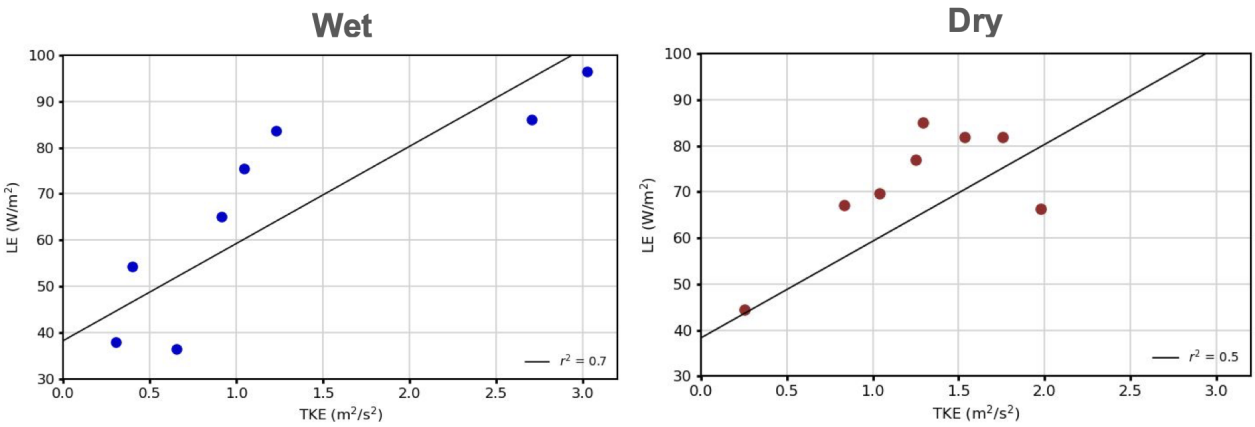

Figure 4.8: Observed daily mean latent heat flux and TKE at the TRI station for the wet and days.

poor correlation between the surface evaporative fraction (latent heat divided by the sum of sensible and latent heat fluxes) and upper layer soil moisture (at 10 cm depth), suggesting that factors other than soil moisture, such as vegetation and transpiration, explain most of the variability in evaporative fluxes. Sensible heat fluxes showed a moderate to strong correlation with net radiation for all sites, with the TRI exhibiting the weakest correlation for the wet days, possibly affected by the sparse vegetation and wetter soils at this location.

This study also identified other factors in addition to radiative fluxes in influencing turbulent fluxes. For instance, at the TRI valley location, latent heat displayed a moderately strong positive correlation with local slope flows ($r^2 \geq 0.5$) for both wet and dry days, while it displayed a weak or no correlation between latent heat and local wind speed at the ridgetops for wet and dry days. The potential impact of valley geometry and thermally-driven flows (valley and slope flows) on moisture and heat exchange between the mountainous surface and the free atmosphere has been noted by previous studies (rotach *et al.*, 2008; Rotach *et al.*, 2015).

In contrast, at the FOR and FRG ridgetop locations, the poor correlation between latent heat and wind speed can be attributed to the higher wind speed at these locations, which reduce the impact of aerodynamic resistance in restricting evaporative fluxes. When comparing the study sites, which differed in elevation and topography, the effect of soil

moisture content on latent heat fluxes became more pronounced. From the lower site (TRI) with higher soil moisture to the higher elevation site (FRG) with lower soil moisture, and considering the averages for mid- or late summer days at each site, latent heat decreased while sensible heat mostly increased with elevation. At FOR forested site, transpiration seem to enhance the latent heat fluxes in midsummer when compared to FRG ridgetop with sparse vegetation but similar soil moisture content, while the cooling effect of a tall canopy results in more decline in sensible heat from mid- to late summer.

Net radiation declined from mid- to late summer at all locations, with the TRI location experiencing the smallest decline, possibly caused by the lower emitted terrestrial fluxes in late summer compared to mid-summer due to a larger cold-pool effect. The smaller decline in net radiation can explain the smaller decline in turbulent fluxes from mid- to late summer at the TRI location. However, wind flows and TKE were recognized to also have an impact on the fluxes in the valley, and can contribute to enhancement or loss of fluxes at this location.

On a fully sunny day on 19 August, the simulated diurnal heat fluxes were mainly overestimated when compared to EC tower observations, with the most significant deviation in simulated sensible heat flux at FOR location. Differences between model predictions of latent and sensible fluxes and the observations affirmed the crucial role of soil moisture, along with net radiation, as impacted by elevation and vegetation, in controlling the heat and evaporative fluxes.

The correlations observed between latent heat and TKE at TRI may suggest non-local influences on moisture and evaporative flux within the valley. This indicates that processes occurring beyond the immediate vicinity of TRI, potentially at FRG or other locations, could impact moisture transport and evaporative flux within the valley.

4.6 Conclusions

In complex terrains, where variations in altitude, latitude, topography and atmospheric and surface parameters are significant, surface energy fluxes exhibit substantial variability from valley areas to ridgetops. While irradiance plays a crucial role, the influence of topography

on the atmospheric and surface hydrometeorological variables such as turbulent flux, wind speed, and soil moisture should also be considered. However, the limited availability of EC towers and meteorological stations in mountainous regions makes it challenging to quantify these variations in atmospheric and surface parameters with high spatial accuracy from observations alone.

The indifference in correlation coefficients between the wet and dry days for the fluxes at a specific location may indicate factors other than soil moisture, such as vegetation, to play a more significant role in appropriating fluxes in complex terrain. However, the indifference of fluxes to soil moisture content at a specific location may be partially related to the limited ranges in soil moisture in the selected samples of wet and dry days. To further investigate this hypothesis, it would be beneficial to gather longer-term data with a wider range of soil moisture levels at each study site, which should be considered for future studies.

Controls on the turbulent fluxes can be quite complex in high mountain areas, as the radiative, and horizontal and vertical boundary layer exchange processes such as turbulence, local and non-local wind and their interactions, as well as soil moisture content and vegetation can all have significant impact on the evaporative fluxes and moisture transport within complex terrain. The persistent higher wind speeds on ridgetops makes wind speed variations less important in generating fluxes, while slope and valley flows can enhance turbulent fluxes in the valley areas.

The results highlight the interplay between latent and sensible fluxes with net radiation, soil moisture content, and horizontal and vertical exchange processes within the boundary layer such as turbulence and local and non-local flows in mountainous terrain. The results have implications for further research aimed at exploring the impact of topography on land-atmosphere interactions in mountainous regions. Since data in high mountain areas are limited, high resolution models can help resolve near-surface processes and their hydrological consequences for future water resources. Additionally, a better understanding of how complex topography affects the partitioning of radiation and turbulent fluxes can enhance the climate modeling of complex terrains and support model validation.

Chapter 5

Conclusions

The purpose of this thesis was to provide improved predictions for the boundary layer processes in complex terrain that impact the near-surface turbulent characteristics, and turbulent fluxes. Due to limited observations in high elevation mountains, numerical weather prediction models have proven to be essential for resolving and understanding of such processes. However, numerical models still face many challenges including representing complex topographic features (e.g. slopes and valleys) and that impedes providing reliable predictions for thermally driven flows and surface heat and evaporative fluxes. Additionally, the simplified assumptions of the model's 1D turbulence parametrization do not apply to complex terrain, misrepresenting thermal and turbulent exchange processes.

LES modeling provides a pathway for taking the 3D effects in a complex terrain into account by resolving larger scale eddies, and modeling smaller scale eddies containing smaller fractions of energy using turbulent closer schemes. Even if using LES improves predictions, there still remains dealing with terrain-following coordinates in numerical models resulting in numerical errors and instabilities when simulating flow over a complex terrain. Therefore, terrain smoothing was considered to overcome these issues, and the model was evaluated using both global and local filtering. Excessive terrain smoothing may result in removing too many valley features and unrealistic flows. Unlike global smoothing, local filtering only smoothes the steeper slopes ($>$ 45 degree), for a more realistic representation of orography. Simulations were performed over the complex terrains of the Fortress

Mountain and Marmot Creek research basins, Kananaskis Valley, Canadian Rockies, Alberta on 18 July, 2016. The model results were verified using SODAR and meteorological stations located on a variety of locations at different elevations, as discussed in chapter 2. Due to limited availability of SODAR, the chosen day for simulations was not a perfect sunny day, and there were partially cloudy skies throughout the day affecting the model validations. LESLF_shade_cloud with the cumulus parametrization activated only for the parent domain provided better predictions for surface wind direction, improved predictions for net radiation, and better RMSE for humidity, and was chosen as a preferable model to study the boundary layer processes in this dissertation. The results highlighted that correct topographic representation, and radiation in very complex terrain has a crucial role in model predictions.

Using the chosen model configuration, simulations implicated influences from the afternoon mesoscale wind or non-local flows interacting with topography on thermally driven valley flows, often disrupting the weak up-valley flow by changing the wind direction, as confirmed by the observations. The results have implications on complex flow interactions between local and non-local flows in the valley locations during daytime in summer, when thermally driven flows prevail. The comparisons between the two different valley volumes in FMRB anf MCRB have implications with regard to cold-air pools and the strength of up-valley wind. The formation and transition of down-valley to up-valley occurred earlier in MCRB valley than in FMRB valley, and the up-valley flows were stronger in the wide but deeper Kananaskis Valley in MCRB, as compared to the narrower and shallower valley in FMRB. The removal of a cold-air pool due to temperature rise happened earlier in the valley in FMRB than in the valley of MCRB due to an elevated inversion layer of the deeper valley. In this study, the larger valley volume had an impact on up-valley wind strength. The results imply complex processes in a complex terrain, and could be related to a combination of various factors such as the thermodynamics related to valley geometry and orientation, contribution from upslope flows, and the rate at which cold air drains down the valley, which helps with the formation of up-valley flows. Based on these results, additional questions arose. For example, what are the implications from the complex flow interactions on exchange processes, i.e. turbulence and sensible and latent heat fluxes in a mountainous terrain? Although these questions have been addressed by other mountain

studies, the diversity in mountain topographies and its effect on the exchange processes remains an open question. This question was the motivation for the second manuscript in chapter 3, which focused on turbulence in the Fortress Mountain area, with a shallow valley, and equipped with eddy covariance systems located in the valley and two ridge tops, required for model validation.

In Chapter 3, a clear-sky summer day (19 August, 2016) in presence of weak synoptic winds was considered for the study. Simulations revealed that an up-valley flow is evident in simulated cross-sections, inclined towards the northern slope of Fortress Mountain, possibly due to the curvature in the eastsouth end of the valley. The presence of an up-valley flow was supported by observations over summer months at the BNS valley station, which is located at the west end of the valley. Both model and observations indicated the presence of cross-ridge flows throughout the day, and the TKE at the TRI valley station was correlated strongly with the wind speed at FRG northern ridge top station. TKE budget analysis using simulations showed that the vertical TKE budget alone may not account for the increase in TKE at the northwest-facing slope, and the horizontal shear production could be an important source for the TKE in the valley. TKE at the northwest-facing slope ceased later in the afternoon when the stable boundary layer set in, alongside a considerable reduction in horizontal shear production. This suggests contribution from the cross-ridge flow to the TKE in the valley, and highlights the importance of the interactions between the up-valley flow and the cross-ridge flows to the TKE production in the valley. The results in this chapter indicate the importance of both vertical and horizontal exchange processes to the turbulence in the valley, and have implications about the impact of these processes on sensible heat and evaporative fluxes in complex terrain.

Further, the impact of complex topography on sensible heat and evaporative fluxes are explored in chapter 4. For this study, longer term observations were desired for a better evaluation of turbulent fluxes, providing data for two summer months. The analysis using three eddy covariance towers in the Fortress Mountain helped to identify different controlling agents with various significance on the turbulent fluxes depending on the location in complex topography. The latent and sensible heat fluxes at all locations, except the wet days at TRI, displayed a strong correlation with the net radiation for both wet and dry summer days. The weaker correlation between net radiation and turbulent fluxes for the

wet days at TRI may suggest influences from sparse vegetation along with wetter soils, causing a faster and more significant response to the changes in near-surface air temperature, and more deviations in sensible heat fluxes. The latent heat at the TRI valley location displayed a moderately strong correlation with the slope flows, but the correlation was weak or insignificant at the ridge tops. When comparing the study sites, which differed in elevation and topography, and considering the changes in radiation from mid- to late summer, the effect of soil moisture content on latent heat fluxes became more pronounced. From low to high elevation sites, with the decrease in soil moisture, the latent heat decreased while the sensible heat increased mostly with elevation. The smaller decline in net radiation from mid- to late summer at the TRI location is caused by the lower emitted terrestrial fluxes in late summer compared to mid-summer due to a larger cold-pool effect. The smaller decline in net radiation can explain the smaller decline in turbulent fluxes from mid- to late summer at the TRI location. However, wind flows and TKE were recognized to also have an impact on the fluxes in the valley, and can contribute to enhancement or loss of fluxes at this location. Finally, it is argued that contributions from the horizontal and vertical exchange, as discussed in chapter 3, can influence the turbulent fluxes in the valley.

The study in this dissertation was unique as it was performed in a shallow valley, but despite the depth of the valley thermally driven flows prevail. The results had implications on up-valley curvature effects, complex flow interactions, and high turbulence in the valley, confirming previous studies performed in deeper valleys. The results overall highlight the complex interplay between the surface sensible heat and evaporative fluxes with variations in net radiation, soil moisture content, turbulence, local and non-local flows in mountainous terrain. With limitations in observations in high mountain areas, high resolution models can help resolve near-surface processes, and be used as an input to hydrological models for future projection predictions of water resources. Future research should incorporate models to study the exchange processes for multiple days and over a wider range of mountain basins with different volumes and topographies to evaluate the impact of spatial and temporal variations in boundary layer processes on horizontal and vertical exchange processes. This can be achieved in future by development of more cost efficient and faster computational resources, and improved numerical methods such as when dealing with vertical coordinates,

representing topography, vegetation, soil moisture, and model resolution. At the moment, LES are computationally costly. However, if a proper 3D parametrization for boundary layer mixing over a complex terrain is realized and incorporated into the models, less cost effective simulations using those parametrizations with lower resolutions than a 100 m can provide a pathway for understanding of exchange processes. Simulations are also still limited to golden days with weak synoptic forcing. The improved understanding of the effect of complex interactions of the local and non-local flows in complex topography helps with improved calculations and evaluations of exchange processes in mountainous terrains.

Based on this work, model predictions using LES was found to result in improved predictions of wind flows and boundary layer processes, and was used to study the impact of such processes on local flows, turbulence, and fluxes in complex terrain. Correct topographic representation, and radiation in very complex terrain were identified to have a crucial role in model predictions. Flow reversals, topographic and mesoscale winds can all have important influences on thermally-driven wind flows in complex terrain. Cloud shading and wind gusts seem to contribute to short-lived flow reversals at the valley locations. The larger valley volume can enhance up-valley wind strength, but removal of cold-air pool due to temperature rise occurs earlier in the deeper valley with an elevated inversion layer. Cross-ridge and up-valley flow, contributed to the TKE budget, and generating turbulence in the valley. This study shows that the vertical TKE budget alone may not account for all the increase in TKE at the northwest-facing slope, and both vertical and horizontal shear and advection could enhance turbulence in a mountain valley. This suggests that the TKE was generated elsewhere and transported to the valley through horizontal and vertical exchange processes. Similarly, local and non-local exchange processes and wind flows were suggested to impact turbulent fluxes in the mountain valley, but radiation, soil moisture and vegetation were found to all have important impacts on the evaporative fluxes and moisture transport within complex terrain. While slope flows can enhance turbulent fluxes in the valley, high wind speeds on ridgetops makes wind speed variations less important in generating evaporative fluxes.

This work can be built upon in future by better modeling approaches, and longer term simulations and observational data, and ultimately a more comprehensive and in depth understanding of boundary layer processes in mountainous terrains. A 3D profiling

of the valley atmosphere through sounding or LIDAR observations can help verify the model results regarding diurnal valley winds speed and direction, temperature, humidity structure, and TKE. Eddy-covariance systems located on the slopes, and in the valley with multiple measurement levels can provide vertical estimates of TKE, TKE production terms, and fluxes for a more comprehensive study of the exchange processes. The results in this study have important implications for horizontal shear production mechanism, and the major role cross-ridge or cross-valley flows play in TKE production in mountainous terrains.

References

[1] D. Arnold, D. Morton, I. Schicker, P. Seibert, M. Rotach, et al. *High resolution modelling in complex terrain: report on the HiRCoT 2012 Workshop, Vienna, 21-23 February 2012*. Institut für Meteorologie, Department Wasser-Atmosphäre-Umwelt, Univ. f . . . , 2012.

[2] R. S. Arthur, K. A. Lundquist, J. D. Mirocha, and F. K. Chow. Topographic effects on radiation in the wrf model with the immersed boundary method: implementation, validation, and application to complex terrain. *Mon. Wea. Rev.*, 146:3277–3292, 2018.

[3] M. Aubinet, T. Vesala, and D. Papale. *Eddy Covariance: A Practical Guide to Measurement and Data Analysis*. Springer and Business Media: Dordrechet, The Netherlands, 2012.

[4] K. Babi´c and M.W. Rotach. Turbulence kinetic energy budget in the stable boundary layer over a heterogeneous surface. *Quart. J. Roy. Meteor. Soc.*, 144:1045–1062, 2018.

[5] W.G. Baily and othres. Atmosphere and surface control on evapotranspiration of alpine tundra in the canadian cordillera. *Hydrology of mountainous regions*, 193:45–52, 1990.

[6] N. Barman, A. Borgohain, S. S. Kundu, R. Roy, B. Saha, R. Solanki, N. V. P. Kiran Kumar, and P. L. N. Raju. Daytime temporal variation of surface-layer parameters and turbulence kinetic energy budget in topographically complex terrain around umiam, india. *Quart. J. Roy. Meteor. Soc.*, 172:149–166, 2019.

[7] W. Brutsaert. *Evaporation into the Atmosphere: Theory, History and Application.* D. Reidel Holland, 1982.

[8] F. K. Chow, C. Schär, N. Ban, K. A. Lundquist, L. Schlemmer, and X. Shi. Crossing multiple gray zones in the transition from mesoscale to microscale simulation over complex terrain. *Atmosphere*, 10(5):274, 2019.

[9] F. K. Chow, A. P. Weigel, R. L. Street, M. W. Rotach, and M. xue. High-resolution large-eddy simulations of flow in a steep alpine valley. part i: Methodology, verification, and sensitivity experiments. *J. Climate Appl. Meteor.*, 45:63–86, 2006.

[10] F. K. Chow, S. FJ. De Wekker, and B. J. Snyder. *Mountain weather research and forecasting: recent progress and current challenges.* Springer, 2013.

[11] A. Colette, F. K. Chow, and R. L. Street. A numerical study of inversion-layer breakup and the effects of topographic shading in idealized valleys. *J. Appl. Meteor.*, 42:1255–1272, 2003.

[12] B. Colman, K. Cook, and B. J. Snyder. Numerical weather prediction and weather forecasting in complex terrain. mountain weather research and forecasting. *F. K. Chow, S. F. J. De Wekker, and B. J. Snyder, Eds., Springer Netherlands, Springer Atmospheric Sciences*, pages 655–692, 2013.

[13] J. P. Conway, J. W. Pomeroy, W. D. Helgason, and N. J. Kinar. Challenges in modeling turbulent heat fluxes to snowpacks in forest clearings. volume 19, pages 1599–1616, 2018.

[14] F. Couvreux et al. Boundary-layer turbulent processes and mesoscale variability represented by numerical weather prediction models during the bllast campaign. *Atmos. Chem. Phys.*, 16(14):8983–9002, 2016.

[15] J. Cuxart. When can a high-resolution simulation over complex terrain be called les? *Frontiers in Earth Science*, 3:87, 2015.

[16] M. H. Daniels, K. A. Lundquist, J. D. Mirocha, D. J. Wiersema, and F. K. Chow. A new vertical grid nesting capability in the weather research and forecasting (wrf) model. *Mon. Wea. Rev.*, 144:3725–3747, 2016.

[17] M. De Franceschi, D. Zardi, M. Tagliazucca, and F. Tampieri. Analysis of second-order moments in surface layer turbulence in an alpine valley. *Quart. J. Roy. Meteor. Soc.*, 135:1750–1765, 2009.

[18] S. F. J. De Wekker and M. Kossmann. Convective boundary layer heights over mountainous terrain—a review of concepts. *Frontiers in Earth Science*, 3:22, 2015.

[19] S. F. J. De Wekker, D. G. Steyn, and S. Nyeki. A comparison of aerosol-layer and convective boundary-layer structure over a mountain range during staaarté 97. *Boundary-Layer Meteorol*, 113:249–271, 2004.

[20] D. Dee et al. The era-interim reanalysis: Configuration and performance of the data assimilation system. *Quart. J. Roy. Meteor. Soc.*, 137(656):553–597, 2011.

[21] H. Diémoz et al. Transport of po valley aerosol pollution to the northwestern alps. part 1: phenomenology. atmospheric chemistry and physics discussions. *phenomenology. Atmospheric Chemistry and Physics Discussions*, pages 1–45, 2018.

[22] P. F. Dornes, J. W. Pomeroy, A. Pietroniro, S. K. Carey, and W. L. Quinton. Influence of landscape aggregation in modelling snow-cover ablation and snowmelt runoff in a sub-arctic mountainous environment. *Hydrological Sciences Journal*, 4:725–740, 2008.

[23] D. J. Downing et al. *Natural regions and subregions of Alberta*. Natural regions committee, ISBN: 0-7785-4573-3, 2006.

[24] J. D. Doyle, C. C. Epifanio, A. Persson, P. A. Reinecke, and G. Zängl. Mesoscale modeling over complex terrain: numerical and predictability perspectives. In *Mountain Weather Research and Forecasting*, pages 531–589. 2013.

[25] J. Dudhia. Numerical study of convection observed during the winter monsoon experiment using a mesoscale two-dimensional model. *J. Atmos. Sci.*, 46(20):3077–3107, 1989.

[26] E. A. B. Eltahir. soil moisture-rainfall feedback mechanism: 1. theory and observations. *Water Resources Research*, 34:765–776, 1998.

[27] X. Fang and J. W. Pomeroy. Simulation of the impact of future changes in climate on the hydrology of bow river headwater basins in the canadian rockies. *Journal of Hydrology*, 620:129566, 2023.

[28] X. Fang, J. W. Pomeroy, C. R. Ellis, M. K. MacDonald, C. M. DeBeer, and T. Brown. Multi-variable evaluation of hydrological model predictions for a headwater basin in the canadian rocky mountains. *Hydrol. Earth Syst. Sci.*, 17:1635–1659, 2013.

[29] L. Fillion et al. The canadian regional data assimilation and forecasting system. *Wea. Forecasting*, 25:1645–1669, 2010.

[30] T. Foken and B. Wichura. Tools for quality assessment of surface-based flux measurements. *Agric For Meteorol*, 78(1-2):83–105, 1996.

[31] F. Gerber, N. Besic, V.Sharma, R.Mott, M.Daniels, M.Gabella, A.Berne, U.Germann, and M.Lehning. Spatial variability in snow precipitation and accumulation in cosmo–wrf simulations and radar estimations over complex terrain. *The Cryosphere*, 12:3137–3160, 2018.

[32] L. Giovannini, L. Laiti, S. Serafin, and D. Zardi. The thermally driven diurnal wind system of the adige valley in the italian alps. *Quart. J. Roy. Meteor. Soc.*, 143(707):2389–2402, 2017.

[33] B. Goger, M. W. Rotach, A. Gohm, O. Fuhner, I. Stiperski, and A. A. M. Holstag. The impact of three-dimensional effects on the simulation of turbulence kinetic energy in a major alpine valley. *Boundary-Layer Meteorol*, 168:1–27, 2018.

[34] B. Goger, M. W. Rotach, A. Gohm, I. Stiperski, and O. Fuhner. Current challenges for numerical weather prediction in complex terrain: Topography representation and parameterizations. pages 890–894, 2016.

[35] B. Goger, I. Stiperski, L.Nicholson, and T.Sauter. Large-eddy simulations of the atmospheric boundary layer over an alpine glacier: Impact of synoptic flow direction and governing processes. *Quart. J. Roy. Meteor. Soc.*, 148:1319–1343, 2022.

[36] A. Gohm et al. Air pollution transport in an alpine valley: Results from airborne and ground-based observations. *Boundary-Layer Meteorol*, 131:441–463, 2009.

[37] A.C. Golzio, S. Ferrarese, C.Cassardo, G.A.Diolaiuti, and M.Pelfini. Land-use improvements in the weather research and forecasting model over complex mountainous terrain andcomparison of different grid sizes. *Boundary-Layer Meteorol*, 180:319–351, 2021.

[38] M. L. Goulden and othres. Evapotranspiration along an elevation gradient in california's sierra nevada. *Journal of Geophysical Research*, 117, G03028, 2012.

[39] V. Grubisić et al. The terrain-induced rotor experiment: A field campaign overview including observational highlights. *Bull. Amer. Meteor. Soc.*, 89:1513–1533, 2008.

[40] P. Harder, M. Schirmer, J. Pomeroy, and W. Helgason. Accuracy of snow depth estimation in mountain and prairie environments by an unmanned aerial vehicle. *Cryosphere*, 10(6):2559–2571, 2016.

[41] W. Helgason and J. W. Pomeroy. Characteristics of the near-surface boundary layer within a mountain valley during winter. *J. Climate Appl. Meteor.*, 51:583–597, 2012.

[42] W. D. Helgason. *Energy fluxes at the air-snow interface*. Ph.D. dissertation, University of Saskatchewan, 171 pp, 2009.

[43] S. Henne, M. Furger, and A. H. Pévpôt. Climatology of mountain venting–induced elevated moisture layers in the lee of the alps. *J. Appl. Meteor.*, 44:620–633, 2005.

[44] S. Henne and othres. Quantification of topographic venting of boundary layer air to the free troposphere. *Chem. Phys.*, 4:497–509, 2004.

[45] U. Hogstrom. Analysis of turbulence structure in the surface layer with a modified similarity formulation for near neutral conditions. *J. Atmos. Sci.*, 47(16):1949–1971, 1990.

[46] S-Y Hong, Y. Noh, and J. Dudhia. A new vertical diffusion package with an explicit treatment of entrainment processes. *Mon. Wea. Rev.*, 134(9):2318–2341, 2006.

[47] P.L. Jackson, G. Mayr, and S. Vosper. Dynamically-driven winds. mountain weather research and forecasting. *Eds., Springer Netherlands, Springer Atmospheric Sciences*, pages 121–218, 2013.

[48] Z. I. Janjić. The step-mountain eta coordinate model: Further developments of the convection, viscous sublayer, and turbulence closure schemes. *Mon. Wea. Rev.*, 122(5):927–945, 1994.

[49] J. Jeworrek, G. West, and R. Stull. Evaluation of cumulus and microphysics parametrizations in wrf across the convective gray zone. *Weather and forecasting*, 34:1097–1115, 2019.

[50] Q. Jiang and J. D. Doyle. Diurnal variation of downslope winds in owens valley during the sierra rotor experiment. *Mon. Wea. Rev.*, 136(10):3760–3780, 2008.

[51] P. A. Jiménez and J. Dudhia. Improving the representation of resolved and unresolved topographic effects on surface wind in the wrf model. *J. Appl. Meteor. Climatol.*, 51(2):300–316, 2012.

[52] P. A. Jiménez, J. Dudhia, J. F. González-Rouco, J. P. Montávez J. Navarro, and E. García-Bustamante. A revised scheme for the wrf surface layer formulation. *Mon. Wea. Rev.*, 140(3):898–918, 2012.

[53] B. Jimenez-Esteve, M. Udina, M. R. Soler, N. Pepin, and J. R. Miro. Land use and topography influence in a complex terrain area: A high resolution mesoscale

modelling study over the eastern pyrenees using the wrf model. *Atmos. Res.*, 202:49–62, 2018.

[54] H. K. Kafle and Y. Yamaguchi. Effects of topography on the spatial distribution of evapotranspiration over a complex terrain using two-source energy balance model with aster data. *Hydrological Processes*, 23:2295–2306, 2009.

[55] J. C. Kaimal and J. J. Finnigan. *Atmospheric boundary layer flows: their structure and measurement*. Oxford Univ. Press, New York, 1994.

[56] J. C. Kaimal and J. J. Finnigan. *Atmospheric boundary layer flows: their structure and measurement*. Oxford Univ. Press, New York, 1994.

[57] J. S. Kain. The kain-fritsch convective parametrization:an update. *J. Appl. Meteor.*, 43(1):170–181, 2004.

[58] P.C. Kalverla, G.-J.Duine, G.-J.Steeneveld, and T.Hedde. Evaluation of the weather research and forecasting model in the durance valley complex terrain during the kascade field campaign. *J. Appl. Meteor. Climatol.*, 55:861–882, 2016.

[59] C. Kiemle et al. Latent heat flux measurements over complex terrain by airborne water vapour and wind lidars. *Quart. J. Roy. Meteor. Soc.*, 137:190–203, 2011.

[60] G. Kirkil, J. Mirocha, E. BouZeid, F. K. Chow, and B. Kosovic. Implementation and evaluation of dynamic subfilter scale stress models for large-eddy simulation using wrf. *Mon. Wea. Rev.*, 140:266–284, 2012.

[61] D. J. Kirshbaum, B. Adler, N. Kalthoff, C. Barthlott, and S. Serafin. Moist orographic convection: Physical mechanisms and links to surface-exchange processes. *Atmosphere*, 9:80, 2018.

[62] J. B. Klemp, W. C. Skamarock, and J. Dudhia. Conservative split-explicit time integration methods for the compressible nonhydrostatic equations. *Mon. Wea. Rev.*, 135(8):2897–2913, 2007.

[63] J. C. Knievel, G. H. Bryan, and J. P. Hacker. Explicit numerical diffusion in the wrf model. *Mon. Wea. Rev.*, 135(11):3808–3824, 2007.

[64] B. Kosović. Wps-geo-localfilter.v1.0. *GitHub*, 2020.

[65] M.N. Lang, A. Gohm, and J.S Wagner. The impact of embedded valleys on day time pollution transport over a mountain range. *Atmos.Chem.Phys.*, 15:14315–14356, 2015.

[66] X. Lee, W. Massman, and B. Law. *Handbook of Micrometeorology: A Guide for Surface Flux Measurement and Analysis*. Kluwer Academic, 250 pp, 2004.

[67] M. Lehner and M. Rotach. Current challenges in understanding and predicting transport and exchange in the atmosphere over mountainous terrain. *J. Atmos.*, 9:276, 2018.

[68] P. Li et al. Observed heterogeneity in the local atmosphere and land–air heat exchange across complex terrain in the tibetan mountains. *Arctic, Antarctic, and Alpine Reserach*, 50:1:e1542209, 2018.

[69] K. Lilly. On the application of the eddy viscosity concept in the inertial sub-range of turbulence. *NCAR Manuscr*, 123:19, 1966.

[70] K. Lilly. The representation of small-scale turbulence in numerical simulation experiments. *IBM Scientific Computing Symposium on Environmental Sciences*, pages 195–210, 1967.

[71] Y. Liu, Y.Liu, D.Muñoz-Esparza, F. Hu, C.Yan, and S.Miao. Simulation of flow fields in complex terrain with wrf-les: Sensitivity assessment of different pbl treatments. *J. Appl. Meteor. Climatol.*, 59:1481–1501, 2020.

[72] L. Mahrt and D. Vickers. Extremely weak mixing in stable conditions. *Boundary-Layer Meteorol*, 119:19–39, 2006.

[73] V. Mahrt. Variation of surface air temperature in complex terrain. *J. Appl. Meteor. Climatol.*, 45:1481–1493, 2006.

[74] D. Martınez, J. Cuxart, and J. Cunillera. Conditioned climatology for stably stratified nights in the lleida area. *Journal of Weather & Climate of the Western Mediterranean*, 5:13–24, 2008.

[75] R. M. Maxwell, F. K. Chow, and S. J. Kollet. The groundwater–land-surface–atmosphere connection: Soil moisture effects on the atmospheric boundary layer in fully-coupled simulations. *Advances in Water Resources*, 30:2447–2466, 2007.

[76] F. Mesinger et al. North american regional reanalysis. *Bull. AM. Meteorol. Soc.*, 87(3):343, 2006.

[77] J. Mirocha, B. Kosović, and G. Kirkil. Resolved turbulence characteristics in large-eddy simulations nested within mesoscale simulations using the weather research and forecasting model. *Mon. Wea. Rev.*, 142(2):806–831, 2014.

[78] E. J. Mlawer, S. J. Taubman, P. D. Brown, M. J. Iacono, and S. A. Clough. Radiative transfer for inhomogeneous atmospheres: Rrtm, a validated correlated-k model for the longwave. *J. Geophys. Res.: Atmospheres*, 102(D14):16663–16682, 1997.

[79] C. H. Moeng, J. Dudhia, J. Klemp, and P. Sullivan. Examining two-way grid nesting for large eddy simulation of the pbl using the wrf model. *Mon. Wea. Rev.*, 135:2295–2311, 2007.

[80] A. S. Monin and A. M. Obukhov. Basic turbulent mixing laws in the atmospheric surface layer. *Trudy Geofiz. Inst. Akad. Nauk SSSR*, 24:163–187, 1954.

[81] D. Muñoz-Esparza, B. Kosović, J. Van Beeck, and J. Mirocha. A stochastic perturbation method to generate inflow turbulence in large-eddy simulation models: Application to neutrally stratified atmospheric boundary layers. *Physics of Fluids*, 27(3), 2015.

[82] D. Muñoz-Esparza, B. Kosović, J. Mirocha, and J. van Beeck. Bridging the transition from mesoscale to microscale turbulence in numerical weather prediction models. *Boundary-layer meteorology*, 153(3):409–440, 2014.

[83] D. Muñoz-Esparza, J. K. Lundquist, J. A. Sauer, B. Kosović, and R. R. Linn. Coupled mesoscale-les modeling of a diurnal cycle during the cwex-13 field campaign: From weather to boundary-layer eddies. *Journal of Advances in Modeling Earth Systems*, 9(3):1572–1594, 2017.

[84] D. Muñoz-Esparza, J. A. Sauer, R. R. Lin, and B. Kosović. Limitations of one-dimensional mesoscale pbl parameterizations in reproducing mountain-wave flows. *J. Atmos. Sci.*, 73(7):2603–2614, 2016.

[85] M. Nakanishi and H. Niino. An improved mellor–yamada level-3 model: Its numerical stability and application to a regional prediction of advection fog. *Boundary-Layer Meteorology*, 119(2):397–407, 2006.

[86] G-Y. Niu, Z-L. Yang, K. E. Mitchell, F. Chen, M. B. Ek, M. Barlage, Kumar, et al. The community noah land surface model with multiparameterization options (noah-mp): 1. model description and evaluation with local-scale measurements. *J. Geophys. Res.: Atmospheres*, 116(D12), 2011.

[87] G. A. Olyphant and S. A. Isard. Some characteristics of turbulent transfer over alpine surfaces during the snowmelt-growing season: Niwot ridge, front range, colorado, u.s. a. *Arctic and Alpine Research*, 19:261–269, 1987.

[88] S. Oncley, C. Friehe, J. LaRue, J. Businger, E. Itsweire, and S. Chang. Surface-layer fluxes, profiles, and turbulent measurements over uniform terrain under near-neutral conditions. *J. Atmos. Sci.*, 53:1029–1044, 1996.

[89] M. Pagès, N. Pepin, and J. R. Miró. Measurement and modelling of temperature cold pools in the c erdanya valley (pyrenees), spain. *Meteor. Appl.*, 24(2):290–302, 2017.

[90] H.A. Panofsky. *Atmospheric Turbulence: Models and Methods for Engineering Applications*. Wiley: Hoboken, NJ, USA, 1984.

[91] Y. Ping, Z. Qiang, W. Runyuan, L. Yaohui, and W. Sheng. Turbulence intensity and turbulent kinetic energy parameters over a heterogeneous terrain of loess plateau. *Advances in Atmospheric Sciences*, 32:1291–1302, 2015.

[92] M. Piper and J. K. Lundquist. Surface layer turbulence measurements during a frontal passage. *J. Atmos. Sci.*, 61:1768–1780, 2004.

[93] J.W. Pomeroy et al. Variation in surface energetics during snowmelt in a subarctic mountain catchment. *J. Hydrometeor.*, 4, 2003.

[94] R. K. Rai, L. K. Berg, B. Kosović, J. D. Mirocha, M. S. Pekour, and W. J. Shaw. Comparison of measured and numerically simulated turbulence statistics in a convective boundary layer over complex terrain. *Boundary-layer meteorology*, 163(1):69–89, 2017.

[95] G. Rampanelli and D. Zardi. A method to determine the capping inversion of the convective boundary layer. *J. Appl. Meteor.*, 43:925–933, 2004.

[96] M. L. Reba, T. E. Link, D. Marks, and J. W. Pomeroy. An assessment of corrections for eddy covariance measured turbulent fluxes over snow in mountain environments. *Water Resources Research*, 45:W00D38, 2009.

[97] J. F. Rihani, F. K. Chow, and R. M. Maxwell. Isolating effects of terrain and soil moisture heterogeneity on the atmospheric boundary layer: Idealized simulations to diagnose land-atmosphere feedbacks. *Journal of Advances in Modeling Earth Systems*, 7:915–937, 2015.

[98] M. Rohanizadegan, R. M. Petrone, J. W. Pomeroy, B. Kosovic, D. Muñoz-Esparza, and W. D. Helgason. High-resolution large-eddy simulations of flow in the complex terrain of the canadian rockies. *Earth and Space Science*, 10, 2023.

[99] M. W. Rotach et al. Boundary layer characteristics and turbulent exchange mechanisms in highly complex terrain. *Acta Geophysicae*, 56:194–219, 2008.

[100] M. W. Rotach et al. Investigating exchange processes over complex topography: the innsbruck box (i-box). *Bull Am Meteorol*, 98:787–805, 2017.

[101] M. W. Rotach, A. Gohm, M. N. Lang, D. Leukauf, I. Stiperski, and J. S. Wagner. On the vertical exchange of heat, mass, and momentum over complex, mountainous terrain. *Frontiers in Earth Science*, 3:76, 2015.

[102] M.W. Rotach and D. Zardi. On the boundary-layer structure over highly complex terrain: key findings from map. *Quart. J. Roy. Meteor. Soc.*, 133:937–948, 2007.

[103] M.W. Rotach and D. Zardi. On the boundary-layer structure over highly complex terrain: key findings from map. *Quart. J. Roy. Meteor. Soc.*, 133:937–948, 2007.

[104] I. R. Saunders and W. G. Bailey. Radiation and energy budgets of alpine tundra environments of north america. *progress in physical geography*, 18(4):517–538, 1994.

[105] J. Schmidli. Daytime heat transfer processes over mountainous terrain. *J. Atmos. Sci.*, 70:4041–4066, 2013.

[106] J. Schmidli, S. Boing, and O. Fuhner. Accuracy of simulated diurnal valleywinds in the swiss alps: Influence of grid resolution, topography filtering, and land surface datasets. *Atmosphere*, 9(5):196, 2018.

[107] J. Schmidli et al. Intercomparison of mesoscale model simulations of the daytime valley wind system. *Mon. Wea. Rev.*, 139:1389–1409, 2010.

[108] J. Schmidli and R. Rotunno. Mechanisms of along-valley winds and heat exchange over mountainous terrain,. *J. Atmos. Sci.*, 67:3033–3047, 2010.

[109] S. Serafin et al. Exchange processes in the atmospheric boundary layer over mountainous terrain. *Atmosphere*, 9(102), 2018.

[110] S. Serafin and D. Zardi. Daytime heat transfer processes related to slope flows and turbulent convection in an idealized mountain valley. *J. Atmos. Sci.*, 67:3739–3756, 2010.

[111] E. Sertel, A. Robock, and C. Ormeci. Impacts of land cover data quality on regional climate simulations. *Int. J. Climatol.*, 30:1942–1953, 2010.

[112] P. Sheridan and S. Vosper. High-resolution simulations of lee waves and downslope winds over the sierra nevada during t-rex iop 6. *J. Appl. Meteor. Climatol.*, 51:1333–1352, 2012.

[113] N Singh, R. Solanki, N. Ojha, R.H.H. Janssen, A. Pozzer, and S.K. Dhaka. Boundary layer evolution over the central himalayas from radio wind profiler and model simulations. *Atmos Chem Phys*, 16:10559–10572, 2016.

[114] W. C. Skamarock et al. A description of the advanced research wrf version 3. *NCAR technical note*, 2008.

[115] J. Smagorinsky. General circulation experiments with the primitive equations: I. the basic experiment. *Mon. Wea. Rev.*, 91(3):99–164, 1963.

[116] E. E. Small and A. K. Shirley. Tight coupling between soil moisture and the surface radiation budget in semiarid environments: Implications for land-atmosphere interactions. *Water Resources Research*, 39:1278, 2003.

[117] R. Solanki, N. Singh, N.V.P. Kiran Kumar, K. Rajeev, R. Imasu, and S. K. Dhaka. Impact of mountainous topography on surface-layer parameters during weak mean-flow conditions. *Boundary-Layer Meteorol*, 172:133–148, 2019.

[118] I. Stiperski and M.W. Rotach. On the measurement of turbulence over complex mountainous terrain. *Bound. Layer Meteorol.*, 159:97–121, 2016.

[119] L. Strauss, S. Serafin, and V. Grubisić. Atmospheric rotors and severe turbulence in a long deep valley. *J. Atmos. Sci.*, 73:1481–1506, 2016.

[120] W. L. Strong. *Ecoregions and ecodistricts of Alberta. Vol 1.*, volume 244, 77pp. Alberta Forestry Lands and Wildlife, Land Information Services Division, Resource Information Branch, Edmonton, Alta., 1992.

[121] R.B. Stull. *An introduction to boundary layer meteorology.* Kluwer Academic Publishers, Dordrecht, 1988.

[122] S. Sukoriansky, B. Galperin, and V. Perov. Application of a new spectral theory of stably stratified turbulence to the atmospheric boundary layer over sea ice. *Boundary-Layer Meteorology*, 117(2):231–257, 2005.

[123] C. Talbot, E. Bou-Zeid, and J. Smith. Nested mesoscale large-eddy simulations with wrf: Performance in real test cases. *J. Hydrometeor.*, 13:1421–1441, 2012.

[124] M. Udina, M. R. Soler, and O. Sol. A modeling study of a trapped lee-wave event over the pyrénées. *Mon. Wea. Rev.*, 145:75–96, 2017.

[125] L. Umek, A.Gohm, M.Haid, H.C.Ward, and M.W.Rotach. Large eddy simulation of foehn-cold pool interactions in the inn valley during piano iop2. *Quart. J. Roy. Meteor. Soc.*, 147:944–982, 2021.

[126] L. Umek, A.Gohm, M.Haid, H.C.Ward, and M.W.Rotach. Influence of grid resolution of large-eddy simulations on foehn-cold pool interaction. *Quart. J. Roy. Meteor. Soc.*, 148:1840–1863, 2022.

[127] Z. Vecenaj, S.F.J. De Wekker, and V. Grubisić. Near-surface characteristics of the turbulence structure during a mountain-wave event. *J. Appl. Meteor. Climatol.*, 50:1088–1106, 2011.

[128] D. Vickers and L. Mahrt. Quality control and flux sampling problems for tower and aircraft data. *J. Atmos. Oceanic Technol.*, 14:512–526, 1997.

[129] V. Vionnet, S. Belair, C. Girard, and A. Plante. Wintertime subkilometer numerical forecasts of near-surface variables in the canadian rocky mountains. *Mon. Wea. Rev.*, 143:666–686, 2015.

[130] S.B. Vosper et al. Cold-pool formation in a narrow valley. *Quart. J. Roy. Meteor. Soc.*, 140:699–714, 2014.

[131] J. S. Wagner, A. Gohm, and M. W. Rotach. The impact of horizontal model grid resolution on the boundary layer structure over an idealized valley. *Mon. Wea. Rev.*, 142(9):3446–3465, 2014.

[132] J. S. Wagner, A. Gohm, and M. W. Rotach. The impact of valley geometry on daytime thermally driven flows and vertical transport processes. *Quart. J. Roy. Meteor. Soc.*, 141(690):1780–1794, 2015.

[133] E. K. Webb, G. I. Pearman, and R. Leuning. Correction of flux measurements for density effects due to heat and water vapour transfer. *Quart. J. Roy. Meteor. Soc.*, 106(447):85–100, 1980.

[134] A. P. Weigel, F. K. Chow, and M. W. Rotach. On the nature of turbulent kinetic energy in a steep and narrow alpine valley. *Boundary-Layer Meteorol*, 123:177–199, 2007a.

[135] A. P. Weigel, F. K. Chow, and M. W. Rotach. On the nature of turbulent kinetic energy in a steep and narrow alpine valley. *Boundary-Layer Meteorol*, 123:177–199, 2007a.

[136] A. P. Weigel, F. K. Chow, and M. W. Rotach. The effect of mountainous topography on moisture exchange between the surface and the free atmosphere. *Boundary-Layer Meteorol*, 125:227–244, 2007b.

[137] A. P. Weigel et al. High-resolution large-eddy simulations of flow in a steep alpine valley. part ii: Flow structure and heat budgets. *J. Appl. Meteor. Climatol.*, 45(1):87–107, 2006.

[138] A.P. Weigel and M.W. Rotach. Flow structure and turbulence characteristics of the daytime atmosphere in a steep and narrow alpine valley. *Quart. J. Roy. Meteor. Soc.*, 130:2605–2627, 2004.

[139] C. D. Whiteman. *Mountain meteorology. Fundamentals and applications.* Oxford University Press, 2000.

[140] D. J. Wiersema, K. A. Lundquist, and F. K. Chow. Mesoscale to microscale simulations over complex terrain with the immersed boundary method in the weather research and forecasting model. *Mon. Wea. Rev.*, 148:577–595, 2020.

[141] J.M. Wilczak, S.P. Oncley, and S. A. Stage. Sonic anemometer tilt correction algorithms. *Boundary-Layer Meteorol*, 99:127–150, 2001.

[142] I. N. Williams and M. S. Torn. Vegetation controls on surface heat flux partitioning, and land-atmosphere coupling. *Geophys. Res. Lett.*, 42:9416–9424, 2015.

[143] M.G. Willoughby et al. *Range plant community types and carrying capacity for the subalpine and alpine subregions*. 3rd approximation, Sustainable Resource Development, Public Land and Forest Division, Edmonton, Alta, T/072, 2006.

[144] J. C. Wyngaard. On the surface-layer turbulence. In *workshop on micrometeorology*, pages 101–149. Amer. Meteorol. Soc., 1973.

[145] J. C. Wyngaard. Toward numerical modeling in the "terra incognita". *J. Atmos. Sci.*, 61(14):1816–1826, 2004.

[146] G. Zängl. An improved method for computing horizontal diffusion in a sigma-coordinate model and its application to simulations over mountainous topography. *Mon. Wea. Rev.*, 130(5):1423–1432, 2002.

[147] G. Zängl. A reexamination of the valley wind system in the alpine inn valley with numerical simulations. *Meteorol. Atmos. Phys.*, 87(4):241–256, 2004.

[148] G. Zängl. The impact of weak synoptic forcing on the valley-wind circulation in the alpine inn valley. *Meteorol. Atmos. Phys.*, 105(1-2):37–53, 2009.

[149] D. Zardi and C. D. Whiteman. Diurnal mountain wind systems. In *Mountain weather research and forecasting*, pages 35–119. Springer, 2013.

[150] H. Zhang, Z. Pu, and X. Zhang. Examination of errors in near-surface temperature and wind from wrf numerical simulations in regions of complex terrain. *Wea. Forecasting*, 28(3):893–914, 2013.

[151] W. Zhao and L. Ainong. A review on land surface processes modelling over complex terrain. *Advances in Meteorology*, 607181, 2015.

[152] X. Zhao and Y. Liu. Relative contribution of the topographic influence on the triangle approach for evapotranspiration estimation over mountainous areas. *Advances in Meteorology*, Hindawi publishing corporation,ID 584040, 2014.

[153] B. Zhou and F. K. Chow. Nested large-eddy simulations of the intermittently turbulent stable atmospheric boundary layer over real terrain. *J. Atmos. Sci.*, 71(3):1021–1039, 2014.